BOSTON UNIVERSITY

GRADUATE SCHOOL OF ARTS AND SCIENCES

Dissertation

FABRICATION AND CHARACTERIZATION OF GALLIUM NITRIDE-BASED LASERS WITH CLEAVED AND CRYSTALLOGRAPHICALLY ETCHED FACETS

by

DEAN A. STOCKER

B. S., Case Western Reserve University, 1991

Submitted in partial fulfillment of the
requirements for the degree of
Doctor of Philosophy
1999

© Copyright by
DEAN A. STOCKER
1999

Approved by

First Reader
____
E. Fred Schubert, Ph.D.
Professor of Electrical and Computer Engineering

Second Reader
____
William J. Skocpol, Ph.D.
Professor of Physics

ACKNOWLEDGEMENTS

I would like to first thank my wife Penny for her constant prayers, love, and encouragement through my years of study.

I would also like to give special thanks my advisor Professor E. Fred Schubert, without whom none of this work would have been possible. He has been a constant source of technical expertise, support and encouragement in this work. The freedom that he has given me to explore new ideas has created a wonderful environment in which to work and in which we have learned much together. He has helped me greatly in all aspects of this work, particularly through discussions and in writing papers together.

I also extend gratitude to Professor William Skocpol for helping me to transition from coursework to labwork at BU. He encouraged and supported me through the comprehensive exams and then introduced me to Prof. Schubert, and I have gone to him for professional advice ever since. Thanks are also due to the other members of my thesis committee, Professors Claudio Rebbi, Sidney Redner, and Jan Smits.

To my colleagues in the lab Wolfgang Grieshaber, John Graff, Ian Goepfert, Li Wei Tu, and Xiaoyun “Jane” Guo, and also to Anlee Krupp, Paul Mak, and Helmut Lingertat, I owe thanks for their assistance, advice, and friendship.

I owe the ability to do this work to those who provided the raw materials, particularly to Dr. Karim Boutros and Dr. Joan Redwing at ATMI, Dr. R. F. Karlicek at Emcore, and Dr. Peter Norris and Dr. Paul Maruska at NZ Applied Technologies.

This work was supported by ONR, the Boston University Photonics Center, the Boston University ECE Department, and especially by NSF.

FABRICATION AND CHARACTERIZATION OF GALLIUM NITRIDE-BASED LASERS WITH CLEAVED AND CRYSTALLOGRAPHICALLY ETCHED FACETS

(Order No.)

DEAN A. STOCKER

Boston University Graduate School of Arts and Sciences, 1999

Major Professor: E. Fred Schubert, Professor of Electrical and Computer Engineering

ABSTRACT

Gallium nitride and its aluminum- and indium-containing alloys are the materials of choice for producing laser diodes that operate at wavelengths throughout the visible and ultraviolet parts of the electromagnetic spectrum. These materials are extremely stable, which allows them to be used in high temperature environments, but makes them difficult to etch. This thesis centers around analyzing the requirements for GaN-based lasers, developing techniques for fabricating them, and characterizing laser cavities which have been fabricated. It includes the first InGaN/GaN double heterostructure lasers, the first demonstration of crystallographic etching of GaN, and the first GaN-based lasers with wet-etched facets.

A theory for calculating specular reflectivity as a function of facet roughness was developed. When applied to InGaN/GaN laser structures, this theory requires a root-mean-square surface roughness (Δd) $\leq$ 4 nm for desired reflectivities of at least 90% of the ideal value.

Cleaved-facet InGaN/GaN laser cavities on sapphire substrates with a facet roughness Δd = 16 nm were fabricated. Laser action occurs above a threshold optical pumping power of

1.3 MW/cm^2, as shown by an increase in the differential quantum efficiency by a factor of 34, significant linewidth narrowing, and strongly polarized output.

Crystallographic wet chemical etching techniques for GaN are presented, displaying etch rates comparable to those of the fastest dry processes. The anisotropic nature of the etching is governed by the energy required to remove gallium atoms from the surface. In addition to overcut and undercut sidewalls, the smoothest etched vertical (*i.e.* parallel to the crystal growth direction) sidewalls ever reported for GaN ($\Delta d < 5$ nm) were demonstrated using these techniques.

Crystallographic etching was used to fabricate the first wet-etched GaN-based laser cavities. The threshold pumping power densities for these laser cavities range from 2.4 MW/cm^2 for 500 μm cavities to 23 MW/cm^2 for 50 μm cavities, indicating an absorption coefficient of 15 cm^{-1} for the laser structure. Comparison of the threshold pumping power densities of the laser cavities before and after crystallographic etching indicate that etching increases the reflectivity by a factor of two or more.

TABLE OF CONTENTS

1. Introduction ____ 1

1.1. The development of light-emitting devices__________________________ 1

1.2. The GaN materials system____________________________________ 4

1.3. Current state-of-the-art of GaN-based lasers_________________________ 7

1.4. Remaining barriers of GaN-based lasers __________________________ 11

2. Laser theory ____ 15

2.1. Luminescence____ 15

2.2. Stimulated emission ____ 20

2.3. Optical feedback____ 27

3. Dry Etching____ 36

3.1. Reactive Ion Etching (RIE) _____________________________________ 36

3.2. Discussion of other dry etching techniques_________________________ 41

3.3. Discussion of advantages and disadvantages of dry etching ___________ 42

4. Cleaving ____ 43

4.1. Physical properties of GaN _____________________________________ 43

4.2. Cleavage of GaN grown on *c*-plane sapphire substrates ______________ 45

4.3. Cleavage of GaN grown on other substrates________________________ 51

4.4. Discussion of advantages and disadvantages of cleaving ______________ 53

5. Photoenhanced Electro-Chemical (PEC) Etching__________________________ 55

5.1. Experimental procedure and etching mechanism _____________________ 55

5.2. Experimental results ____ 57

5.3. Origins and control of the roughness of PEC-etched surfaces ___________ 60

5.4. Discussion of advantages and disadvantages of PEC etching ___________ 67

6. Anisotropic Wet Chemical Etching______________________________________ 68

6.1. Etching mechanisms and theoretical models_________________________ 68

6.2. Experimental results ____ 73

6.3. Discussion of advantages and disadvantages of wet etching ____________ 89

7. Lasers ____ 91

7.1. Heterostructure design____ 91

7.2. Cleaved-facet lasers ____ 97

7.3. Wet-etched-facet lasers____ 105

8. Conclusions____ 114

8.1. Techniques for facet fabrication___________________________________ 114

8.2. Demonstrations of cleaved and wet-etched lasers____________________ 116

8.3. Proposed directions for future research ____________________________ 117

9. Appendix A: Miller indices in a hexagonal lattice ________________________ 119

LIST OF TABLES

Table 6.1: Wet chemical etch rates and observed etching planes for various chemicals. 88

Table 9.1: Conventions for planes and directions using Miller indices in a hexagonal coordinate system ______________________________________ 123

Table 9.2: Labels and Miller indices for common planes in a hexagonal coordinate system. ____ 123

LIST OF FIGURES

Figure 1.2.1: Bandgap energies for several families of III-V semiconductors at a temperature of 300 K.___ 4

Figure 1.2.2: Chromaticity diagram from the Commission Internationale de l'Éclairage. The black triangle outlines the area that can be produced by a standard television, and the white triangle outlines the area that can be produced by a display made with red AlGaAs LED's and blue and green InGaN LED's.___ 6

Figure 1.3.1: Structure of an InGaN/GaN multiple quantum well (MQW) LD (Reprinted with permission from Ref. 36).___ 8

Figure 1.3.2: Typical L-I and V-I characteristics of InGaN MQW LD's measured under CW operation at room temperature (Reprinted with permission from Ref. 36). 9

Figure 1.3.3: Laser emission spectra measured under room temperature CW operation with current densities of (a) $J = 1.0J_{th}$ (b) $J = 1.2J_{th}$ (Reprinted with permission from Ref. 36). ___ 10

Figure 2.1.1: Basic transitions in a semiconductor. E_C, E_V, E_A, E_D, E_t, and E_g are the energies of the conduction band, the valence band, an acceptor, a donor, a trap, and the bandgap, respectively. ___ 17

Figure 2.1.2: Typical photoluminescence spectrum of n-type GaN showing near-bandgap18

Figure 2.1.3: Typical photoluminescence spectrum of Mg-doped p-type GaN showing near-bandgap and donor-acceptor pair luminescence. ____________________ 19

Figure 2.2.1: Radiative transitions: (a) spontaneous emission, (b), absorption and (c) stimulated emission. ____ 21

Figure 2.2.2: Schematic of the "variable stripe length method" for determining the net optical gain of a semiconductor.____ 24

Figure 2.2.3: Schematic for the derivation of the output intensity as a function of stripe length for the variable stripe length method. _____________________________ 24

Figure 2.2.4: Room temperature net optical gain measurements using the variable stripe26

Figure 2.3.1: Schematic of the active region of a laser, demonstrating optical feedback. 28

Figure 2.3.2: Sample surface for mathematical model of reflectivity as a function of roughness. The arcs represent the wavefronts of Huygen's elementary waves generated by the reflection of plane waves from the surfaces. _________ 30

Figure 2.3.3: Power reflectivity of glass as a function of surface roughness for λ_0 = 633 nm. R_0 is the experimental reflectivity for an unroughened surface. ________ 33

Figure 2.3.4: Power reflectivity of InGaN/GaN laser facets as a function of surface___ 35

Figure 3.1.1: Schematic of a reactive ion etching system__________________________ 37

Figure 3.1.2: GaN reactive ion etching depth as a function of etching time in a 200W plasma with a flow rate of 10 sccm Cl_2 at 8mTorr 38

Figure 3.1.3: Reactive-ion-etched facets, with a 70° sidewall angle and a 200 nm sidewall roughness 39

Figure 3.1.4: Scanning electron microscope (SEM) image of a dry etched facet in a GaInAlN device. (Reprinted with permission from Ref.) 40

Figure 4.1.1: Crystal structure of Wurtzite GaN. The top two atomic layers are shown as they would appear when looking down along the growth axis. The plane of the paper is the (0001) *c*-plane. The $\{11\bar{2}0\}$ *a*- and $\{10\bar{1}0\}$ *m*-planes are perpendicular to the *c*-plane, cutting across it in the directions shown. 44

Figure 4.2.1: Method for cleaving GaN epilayers on a sapphire substrate. 45

Figure 4.2.2: Projection of bulk *c*-plane sapphire and GaN cation positions for the observed epitaxial growth orientation. The dots mark aluminum atom positions and the dashed lines show the sapphire *c*-plane unit cells. The open squares mark gallium atom positions and the solid lines show the GaN *c*-plane unit cells. (Reprinted with permission from Ref. 39) 47

Figure 4.2.3: Images of cleaved GaN on *c*-plane sapphire. (a) Atomic force microscope image of cleaved *a*-plane GaN, showing striations with an RMS roughness of

16 nm. All units are in µm. (b) SEM micrograph of cleaved *m*-plane GaN, showing 90 nm steps occurring at ~2.2 µm intervals.________________ 48

Figure 4.2.4: SEM images of cleaved sapphire. (a) Edge cleaved along the *a*-plane. (b) Edge broken 2° off of the *a*-plane ________________________________ 50

Figure 4.4.1: Comparison of cleaved-facet and etched-facet lasers for far-field and integrated optoelectronic device applications. ______________________________ 53

Figure 5.1.1: Schematic of PEC etching apparatus ______________________________ 56

Figure 5.2.1: SEM images of PEC-etched GaN. (a) Side view of an etched sidewall. The 60-nm-thick titanium mask is visible on the top. The sidewall itself appears rough, and the bottom etched surface is extremely rough, covered with "stalagmites" of GaN. (b) Top view of the same sidewall. The roughness of the titanium mask is easily visible at this higher magnification. ________ 58

Figure 5.2.2: Surface energy band diagram for n- and p-type GaN ________________ 59

Figure 5.3.1: SEM images of various types of surface features which develop in GaN during PEC etching: (a) columns, (b) cones, and (c) whiskers. The bars in the lower right corners are 1µm long.____________________________________ 61

Figure 5.3.2: The relative roughness, *i.e.*, the ratio of the average peak height to the maximum etch depth, of the PEC-etched GaN surface as a function of bias voltage and KOH concentration at room temperature. _______________ 63

Figure 5.3.3: Matlab™ simulation of the electric field in a weak ionic solution between a smooth cathode, representing the gold wire, on the right and a rough anode, representing the GaN surface, on the left. The field is strongest at the peaks on the GaN anode, increasing the etch rate at the peaks and smoothing the surface. ____ 65

Figure 5.3.4: The minimum PEC etch rate, *i.e.* the etch rate of the GaN peaks, as a function of voltage for various KOH concentrations at room temperature. ____ 66

Figure 5.3.5: Schematic showing a step edge and the corresponding dangling bonds on a silicon (100) surface. The dashed lines represent bonds; the darker colored atoms are recessed into the page by ¼ of a lattice vector compared to the lighter colored atoms. ____ 69

Figure 5.3.6: (a,b) Predicted cross-sectional profiles for opposing sides of a mesa etched in a {511} oriented GaAs slice using 1 H_2SO_4 : 8 H_2O_2 : 40 H_2O etchant. The diagrams upon which they are based are below each profile. (c) Micrograph of an actual cross section after etching. (D. W. Shaw, 1979) ____ 72

Figure 5.3.7: Top view of hexagonal etch pits formed in the *c*-plane of GaN by etching in molten KOH. ____ 75

Figure 5.3.8: High-resolution field-effect SEM image of dislocation etch pits in the *c*-plane of GaN, produced by etching in 10% KOH by weight dissolved in ethylene glycol at 165°C. ____ 75

Figure 5.3.9: SEM images of crystallographic surfaces of GaN made by wet etching. (a) Overcut $\{10\bar{1}3\}$ plane etched by H_3PO_4. (b) Undercut $\{10\bar{1}\bar{2}\}$ plane etched by H_3PO_4. (c) Vertical $\{10\bar{1}0\}$ plane etched by KOH in ethylene glycol. (d) Undercut $\{10\bar{1}\bar{1}\}$ plane etched by molten KOH. 77

Figure 5.3.10: Arrhenius plot of etch rates for GaN in H_3PO_4. 79

Figure 5.3.11: Arrhenius plot of GaN etch rates in KOH and 30% KOH dissolved in ethylene glycol. Solid and hollow symbols represent etch rates measured along cleaved edges parallel to the $\{11\bar{2}0\}$ *a*-plane and the $\{10\bar{1}0\}$ *m*-plane, respectively. 80

Figure 5.3.12: GaN etch rate as a function of KOH concentration in ethylene glycol at 170 °C. Solid and hollow symbols represent etch rates measured along cleaved edges parallel to the sapphire $\{10\bar{1}0\}$ *m*-plane and $\{11\bar{2}0\}$ *a*-plane, respectively. 81

Figure 5.3.13: SEM image of a $\{10\bar{1}\bar{2}\}$ crystallographic p-type GaN surface made by wet etching in molten KOH at 243°C. The black bar in the lower right corner is 1 μm long. 82

Figure 5.3.14: SEM image of a $\{10\bar{1}0\}$ crystallographic p-type GaN surface made by wet etching in molten KOH at 197°C. The white bar on the lower right side is 1 μm long. 83

Figure 5.3.15: Arrhenius plots of n- and p-type GaN etch rates in molten KOH. 85

Figure 5.3.16: Arrhenius plot of p-type GaN etch rates in H_3PO_4 and in 30% KOH by weight dissolved in ethylene glycol.____ 86

Figure 5.3.17: Modified Wulff diagrams of etch rates normal to the GaN $[11\bar{2}0]$ direction for etching in (a) molten KOH or KOH dissolved in ethylene glycol, (b) H_3PO_4, and (c) TEAH or TMAH.____ 87

Figure 6.1.1: Schematic of the InGaN/GaN double heterostructure laser structure. The active region consists of Si-doped $In_{0.09}Ga_{0.91}N$, which has a refractive index $\bar{n}$ = 2.57. The cladding layer is undoped GaN, $\bar{n}$ = 2.54. This structure is grown on *c*-plane sapphire, $\bar{n}$ = 1.8.____ 92

Figure 6.1.2: Trajectory of a light ray guided in a laser cavity with a dielectric slab waveguide. ____ 93

Figure 6.1.3: Power reflectivity *R* for TE and TM modes in a laser with a slab waveguide, as a function of incident angle.____ 95

Figure 6.2.1: Schematic of optical pumping and collection optics for a laser cavity in edge-emitting configuration.____ 98

Figure 6.2.2: Pumping and collection optics for stimulated emission measurements.____ 99

Figure 6.2.3: Peak and integrated emission intensities as a function of incident excitation power density. The inset shows an expanded view of the low-power regime.

Above threshold, the slope increases by a factor of 34 and 210 for the integrated and peak intensities, respectively.____________________ 100

Figure 6.2.4: Emission spectra for different excitation levels. At sub-threshold excitation intensities, a broad band centered at 3.18 eV (390 nm) is visible. Above threshold, a narrow peak emerges, centered at 3.15 eV (394 nm). ____ 102

Figure 6.2.5: Polarized emission spectra taken at $2.4 \times P_{\text{threshold}}$. The TM mode shows the103

Figure 6.3.1: Schematic showing the positioning of the silicon wafer and sample during PEC etching. ____ 106

Figure 6.3.2: Smoothing of a surface produced by photo-enhanced electrochemical (PEC) etching of an InGaN/GaN double heterostructure. The 10 μm bar underneath the figure is valid for all of the SEM images. (a) PEC-etched surface before smoothing by crystallographic etching in molten KOH at 175°C. (b) PEC-etched surface after smoothing for 1 min. (c) After smoothing for 3 min. (d) After smoothing for 9 min.__________________________________ 107

Figure 6.3.3: Emission spectra of a 500 μm wet-etched laser cavity for several different pumping power levels. At sub-threshold excitation powers, two broad bands are visible, one at 3.18 eV (390 nm) and another at 3.32 eV (373 nm). Above threshold, a narrow peak emerges at 3.13 eV (396 nm) and moves to slightly lower energy as pumping power is increased. ___________________ 109

Figure 6.3.4: Peak emission intensity, FWHM, and TE/TM ratio for a 500 μm wet-etched laser cavity over a wide range of pumping power densities. The laser threshold is at 2.7 MW/cm^2. ____ 111

Figure 6.3.5: Measured threshold current density as a function of inverse cavity length. 113

Figure 7.3.1: Base vectors for Miller indices in a hexagonal lattice.______________ 120

Figure 7.3.2: A plane intersecting the first three directional vectors in a hexagonal lattice at points B, C, and D. The fourth direction is out of the page. Point A is at the origin. ____ 121

Figure 7.3.3: Geometric constructions for determining the relationship between the first three Miller indices in a hexagonal coordinate system.__________________ 122

LIST OF ABBREVIATIONS

CAIBE	Chemically-assisted ion beam etching
CW	Continuous wave
DH	Double heterostructure
DVD	Digital video disk (also called a “digital versatile disk”)
ECR	Electron-cyclotron resonance
ELOG	Epitaxial lateral overgrowth
FWHM	Full width at half maximum
HVPE	Hydride vapor phase epitaxy
LD	Laser diode
LED	Light-emitting diode
MOCVD	Metal-organic chemical vapor deposition
MQW	Multiple quantum well
PEC	Photo-electro-chemical
QW	Quantum well
RIE	Reactive ion etching
RF	Radio frequency
RMS	Root-mean-square
SEM	Scanning electron microscope
TE	Transverse electric
TM	Transverse Magnetic
UV	Ultraviolet

1. Introduction

1.1. The development of light-emitting devices

> In the beginning God created the heavens and the earth. Now the earth was formless and empty, darkness was over the surface of the deep, and the Spirit of God was hovering over the waters. And God said, "Let there be light," and there was light. God saw that the light was good.[1]

In the story of creation, light is the first step in bringing order to a formless universe. From time immemorial, the sun's light has ordered our days, as its light aids us in our daily activities. Over the centuries, man has learned to harness this power of light. From the time we began to learn to control fire, we have been continually searching for brighter and more efficient manmade sources of light. Thomas Edison made a remarkable breakthrough in 1879 when he demonstrated that under the proper conditions a horse-hair filament can convert electrical energy into light. This was the first incandescent light bulb, versions of which are still widely used today for many applications, first became commercially available at the beginning of this century. Over the next 50 years, brighter and more efficient neon, fluorescent, and sodium discharge lamps have replaced incandescent bulbs for many purposes.[2]

In 1962 high-efficiency[a] electroluminescence from semiconductors was demonstrated, opening the era of light-emitting-diode (LED) technology.[3] Until recently, LED technology has been almost exclusively limited to the Ga(Al,In)As and Ga(Al,In)P materials systems, which emit light in the infrared to yellowish-green portion of the electromagnetic spectrum. This emission range is determined by the *bandgap*, i.e. the difference in energy between the top of the valence band and the bottom of the conduction band, of the semiconductors. LED's are now used commonly in commercial products, including display panels. Almost every electronic device has a small red LED indicator light on it somewhere, and red LED's are increasingly being used in traffic lights and for brake lights in cars.

---

[a] "High-efficiency" in this case is on the order of 1%; light emitting diodes today have efficiencies on the order of a few percent.

Another major leap in light production came with the advent of lasers. Laser light is unique, in that it is preferentially emitted along one direction through a process called "stimulated emission." The word "laser" is actually an acronym for "Light Amplification by Stimulated Emission of Radiation." Albert Einstein introduced the concept of stimulated emission in 1917,[4] and the first experimental evidence was found in 1928.[5] The first report of stimulated emission from a semiconductor was in 1962.[6] Semiconductor laser diodes (LD's) are in general much more efficient than gas lasers. Power conversion efficiencies of ~50% are not unusual for diode lasers, while the efficiencies of gas lasers are typically ~1%.[7] As with LED's, LD's have been almost exclusively limited to the Ga(Al,In)As and Ga(Al,In)P materials systems, so again the emission wavelengths fall in the infrared to yellow range. These LD's have a broad range of commercial applications, including fiber-optic communications, laser printing, and optical data storage.

It would be beneficial to have LD's which emit in the green to UV range, to complement the LD's which are currently available. Introduction of short-wavelength LD's in the green-to-UV portion of the spectrum will open up the possibility of full-color laser projection displays and undersea optical communication. These shorter wavelengths will also allow an increase in the optical storage densities of digital video disks (DVD's) by as much as a factor of 4, because the storage density is inversely proportional to the square of the wavelength. Similarly, improvements in the resolution of laser printers and color copiers are possible with the introduction of short-wavelength LD's.

Three different materials systems are now in the developmental stages for making short-wavelength LD's: organic materials,[8,9] II-VI semiconductors such as ZnSe,[10,11] and III-V Nitrides.[12,13] Organic materials are the newest entry into the laser diode arena, with stimulated emission first reported in 1996, and although they are not as well developed as the II-VI semiconductors and the III-V Nitrides, when the technology is more mature it may offer an alternative with mechanical flexibility and very low price.[14] The stability of the organic materials, however, is still uncertain. II-VI materials can potentially be used to develop green and blue light emitters, but they have very short lifetimes, probably due to stacking faults and rapid oxidation.[15,16] A low formation energy allows native defects to form spontaneously in the II-VI's, so high defect densities are apparently a fundamental property of these materials.[17] III-V Nitrides (GaN and its aluminum- and indium-containing alloys) are currently leading the pack in short-wavelength LED and LD development; this dissertation focuses upon the III-V Nitrides.

1.2. The GaN materials system

Crystalline GaN films were first grown by a process called Hydride Vapor Phase Epitaxy (HVPE) in 1969.[18] The bandgap of GaN and several other III-V semiconductors which are commonly used as light-emitters are shown in Figure 1.2.1. For this figure, the bandgap energies for the Nitrides are taken from S. Strite and H. Morkoç,[19] and those of the Arsenides and Phosphides are taken from R. A. Smith.[20] The bandgap of GaN is 3.39 eV, which falls within the ultraviolet (UV) portion of the spectrum.[18] As this figure shows, Nitride-based light emitting devices fill in the shorter wavelengths (i.e. higher energies) of the spectrum that can not be reached by the other III-V semiconductor materials.

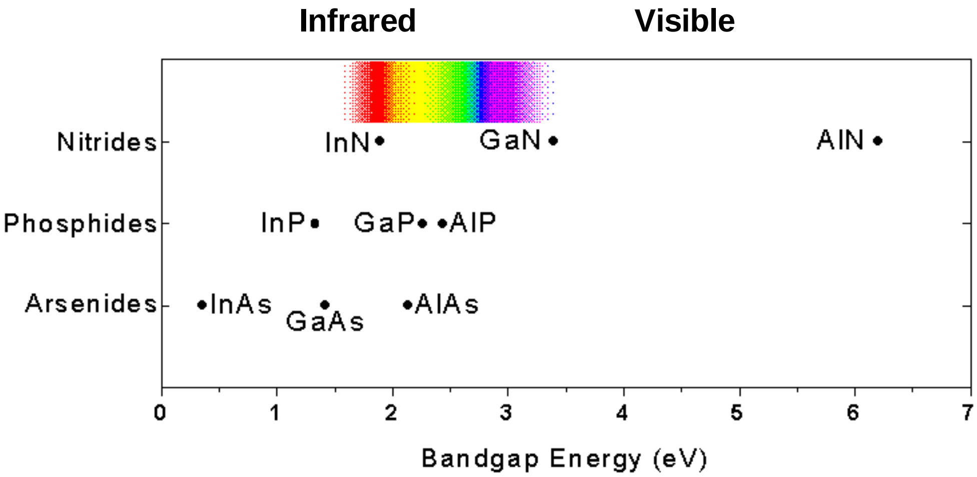

Figure 1.2.1: Bandgap energies for several families of III-V semiconductors at a temperature of 300 K.

The various binary compound semiconductors shown in Figure 1.2.1 can be combined to form semiconductors with a wide range of bandgap energies. It is possible, for example, to grow $In_xGa_{1-x}N$, where x can be varied from 0 – 1. The bandgap is dependent upon x, and can fall anywhere between the bandgaps of InN and GaN, thus filling in the spectrum between red and near UV. There is much research in progress concerning phase separation of InGaN alloys,[21–23] which will not be dealt with in detail in this dissertation. In-rich precipitates form in $In_xGa_{1-x}N$ for $x > 0.2$, which suggests that not all possible values of x between 0 and 1 yield stable crystals. It is possible to grow thin InGaN layers with $x > 0.2$ without phase separation, but to date phase separation has been consistently observed in thicker layers.[22] Blue and green InGaN LED's are now commercially available from several different manufacturers, including Nichia Chemical Corp., CREE Research Corp., and Hewlett-Packard Corp.

With the introduction of GaN-based LED's, several important areas of application have already been opened up. One application is an LED display with all three primary colors of light. Because InGaN LED's fill in the remaining visible portions of the spectrum, they can be used in conjunction with existing AlGaAs devices to make full-color displays that can produce more vivid colors than a conventional television. The chromaticity diagram in Figure 1.2.2 shows all possible combinations of light detectable by the human eye. The black triangle outlines the region that can be produced by a standard television, and the white triangle outlines the region that can be produced by a display made with commercially available LED's. Filling out the visible spectrum also opens up the possibility of producing LED traffic lights, which would have higher efficiencies and longer lifetimes than the incandescent bulbs currently in use. Red LED's are already replacing the red lenses and incandescent bulbs used for red lights on traffic signals, and we may soon see LED's replacing the yellow and green lights. While III-V Nitride LED's have already been commercialized, there is still considerable work to be done before commercialization of III-V Nitride laser diodes.

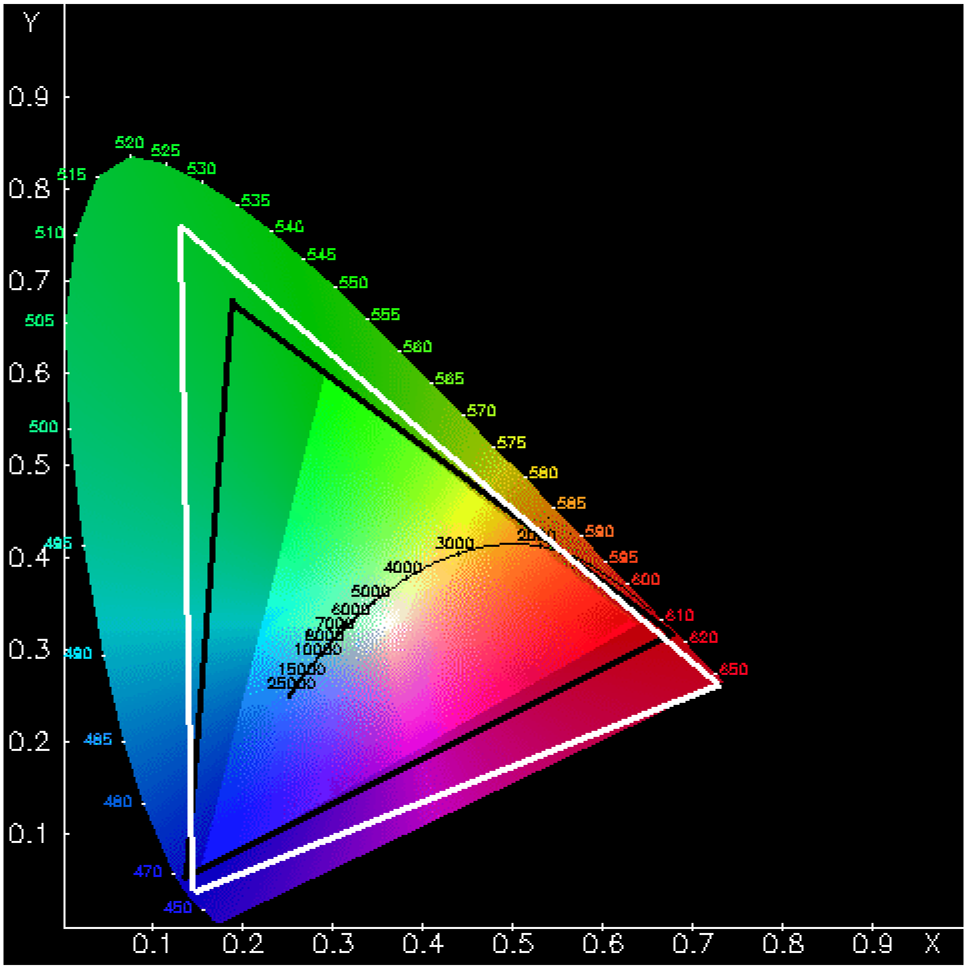

Figure 1.2.2: Chromaticity diagram from the Commission Internationale de l'Éclairage. The black triangle outlines the area that can be produced by a standard television, and the white triangle outlines the area that can be produced by a display made with red AlGaAs LED's and blue and green InGaN LED's.

1.3. Current state-of-the-art of GaN-based lasers

Although optically pumped stimulated emission was observed in GaN at low temperatures as early as 1971,[24] the crystal quality was not good enough for significant stimulated emission to occur at room temperature until 1990.[25] The improvement in the optical properties of the crystals between 1971 and 1990 was due primarily to improved growth techniques for GaN, such as metal-organic chemical vapor deposition (MOCVD),[26] and the introduction of an intermediate "buffer" layer between the substrate and the epitaxial GaN.[27,28]

Due to difficulties in overcoming unintentional n-type background doping levels and activating p-type acceptors,[29,30] demonstration of an electrically pumped GaN-based laser diode (LD) took five more years. Shuji Nakamura *et al.* of Nichia Corporation in Japan reported the first GaN-based LD in January of 1996.[31] Nakamura's first LD's were operated under pulsed-current conditions, but he achieved room temperature continuous wave (CW) operation by the end of 1996.[32] While other groups have reported pulsed operation of GaN-based LD's,[33,34,35] no others have yet reported a CW laser diode with a lifetime longer than 1 minute.

To give a sense of the current state-of-the-art for GaN-based lasers, some results for Nakamura's GaN-based laser diodes, as reported in the *MRS Internet Journal of Nitride Semiconductor Research* in March of 1997 will be presented.[36] Since this publication was released, some improvements have been made, so that the lifetime of an LD operating at 2 mW output power has an expected lifetime of 10,000 hours, and the maximum output power achieved from a single GaN-based LD is 140 mW.[37]

The basic structure that Nakamura *et al.* used is shown in Figure 1.3.1. The active region is an $In_{0.02}Ga_{0.98}N/In_{0.15}Ga_{0.85}N$ multiple quantum well (MQW), bounded by GaN guiding layers and Al$_{0.08}$Ga$_{0.92}$N cladding layers. The operating voltage and output power as a function of current for a typical LD are shown in Figure 1.3.2. The threshold current is approximately 82 mA, and the operating voltage is greater than 5 V. Ideally, the operating voltage should be close to 3.4 V, which is the bandgap energy of GaN divided by the elementary charge of an electron.

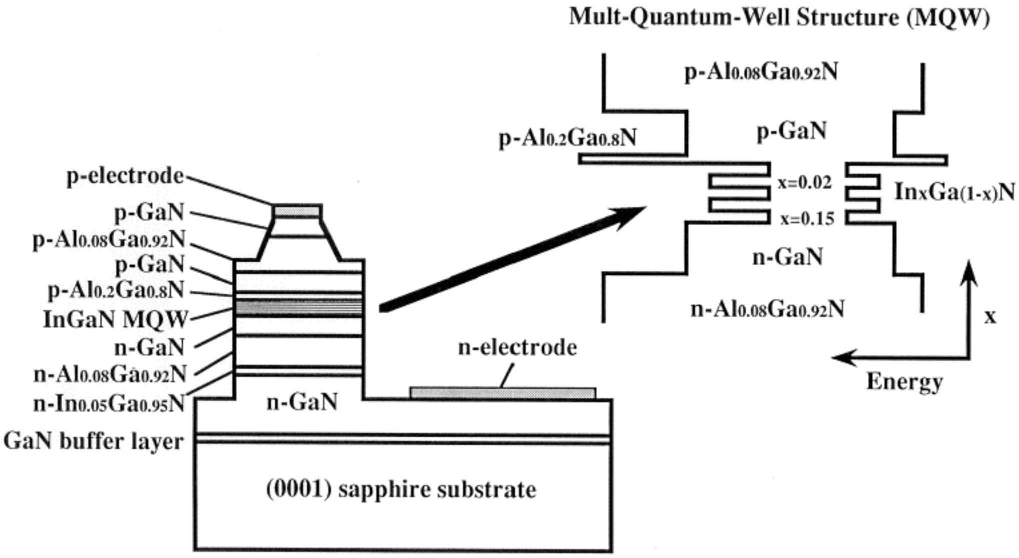
Mult-Quantum-Well Structure (MQW)
p-Al$_{0.08}$Ga$_{0.92}$N
p-Al$_{0.2}$Ga$_{0.8}$N
p-GaN
x=0.02
x=0.15
In$_x$Ga$_{(1-x)}$N
n-GaN
n-Al$_{0.08}$Ga$_{0.92}$N
x
Energy
p-electrode
p-GaN
p-Al$_{0.08}$Ga$_{0.92}$N
p-GaN
p-Al$_{0.2}$Ga$_{0.8}$N
InGaN MQW
n-GaN
n-Al$_{0.08}$Ga$_{0.92}$N
n-In$_{0.05}$Ga$_{0.95}$N
GaN buffer layer
n-GaN
n-electrode
(0001) sapphire substrate

Figure 1.3.1: Structure of an InGaN/GaN multiple quantum well (MQW) LD (Reprinted with permission from Ref. 36).

The upper and lower spectra in Figure 1.3.3 are for current densities (J) equal to and greater than the laser threshold, respectively. The arbitrary units used for the y axis are different for the upper and lower spectra. In the upper spectrum, optical modes are clearly visible, with a spacing of approximately 0.04 nm. These well-known modes are due to the effects of the optical mode density of a Fabry-Perot optical resonator on the strongly non-linear stimulated emission dynamics. In the lower spectrum, the mode with the highest optical net gain has become dominant, with the two modes closest to it also visible.

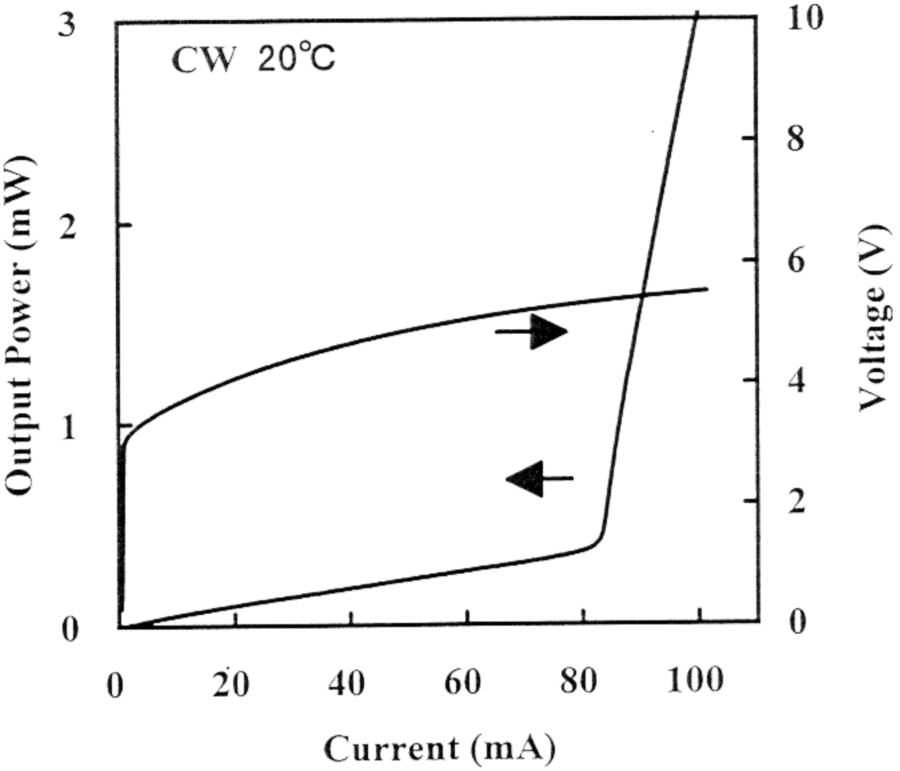

Figure 1.3.2: Typical L-I and V-I characteristics of InGaN MQW LD's measured under CW operation at room temperature (Reprinted with permission from Ref. 36).

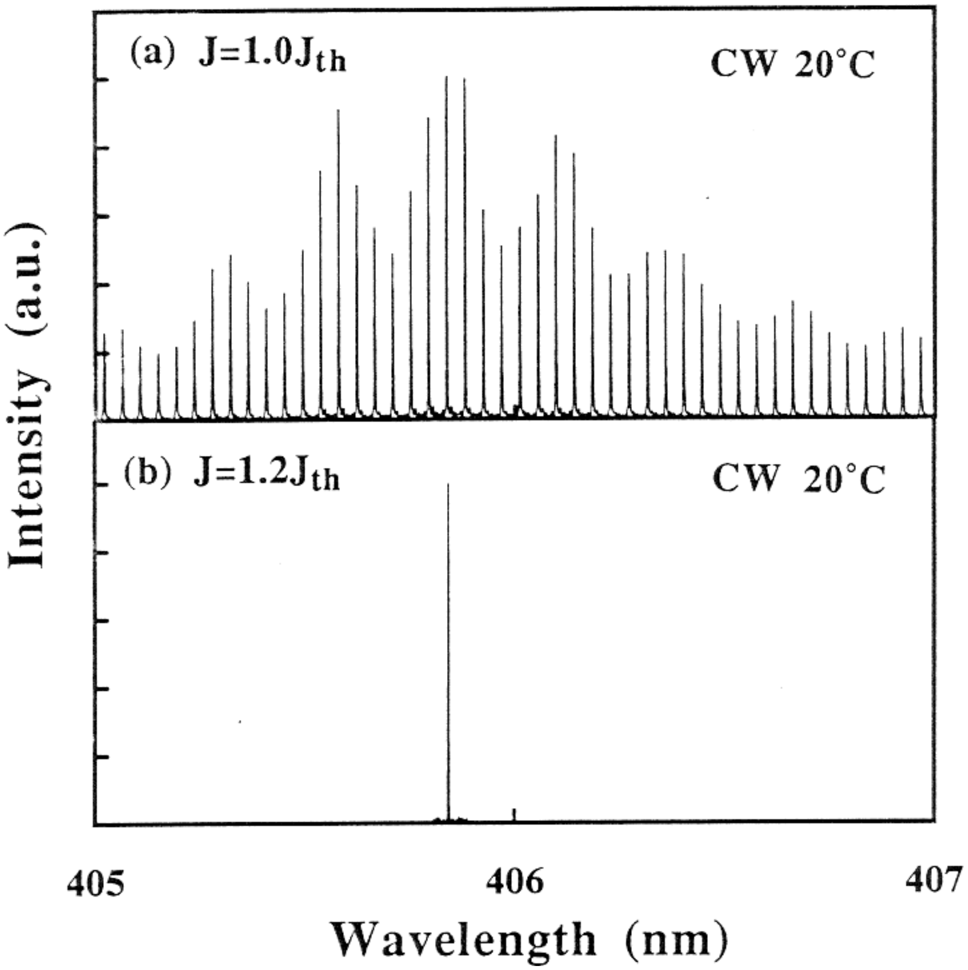

Figure 1.3.3: Laser emission spectra measured under room temperature CW operation with current densities of (a) $J = 1.0J_{th}$ (b) $J = 1.2J_{th}$ (Reprinted with permission from Ref. 36).

1.4. Remaining barriers of GaN-based lasers

Despite the recent successes in fabrication of pulsed and CW III-Nitride LD's by groups in the United States and Japan, there are still some major barriers that need to be overcome before commercialization. The three areas most in need of research are growth of low-defect material, lowering device resistance and improving mirror quality.

Most of the crystal defects in GaN are screw and threading dislocations that start at the interface between the substrate and epilayers and continue vertically through the epilayers. Poor lattice matching between substrate and epilayers, 3.5% when a SiC substrate is used[38] and ~15% when a sapphire substrate is used,[39] is responsible for the high defect density at the interface. GaN films grown on sapphire, the most commonly used substrate, have threading dislocation densities on the order of 10^7 to 10^{11} cm^{-2}.[40,41] In silicon and GaAs, such high dislocation densities are enough to render the material useless for device applications, but GaN LED's with relatively high efficiencies have been made despite the high defect densities.[42]

There are at least two possible explanations of how it is possible to make LED's with material that has so many crystal defects. The first explanation is that many of the defects are electrically neutral,[43,44] and the geometry of the electrically active defects is such that they do not scatter electrons that are travelling vertically through the material,[38] as they are in a typical LED structure. The second explanation has to do with the small diffusion length of GaN. If the defect density of GaN is 10^8 cm^{-2}, the average distance between defects is approximately 10^{-4} cm, or 1 μm. The diffusion length L_D is given by the diffusion coefficient D of the material and the lifetime τ of the carriers as follows:

$$L_{\mathrm{D}} = \sqrt{D\tau}\,. \qquad \textbf{Equation 1.4.1}$$

The diffusion coefficient can be calculated using the Einstein relation

$$D = \frac{\mu kT}{e}\,. \qquad \textbf{Equation 1.4.2}$$

The highest mobilities reported for GaN are 1000 cm^2/Vs for electrons and 30 cm^2/Vs for holes,[45] and the lifetime of the carriers at room temperature is on the order of 0.1 to 1 ns.[46–48] This range of values gives a diffusion length of 0.1 μm to 1 μm. Since the diffusion length is less than the average distance between defects, many electron-hole pairs combine radiatively before reaching a defect where non-radiative recombination could occur. Either or both of these effects could be a factor in understanding why GaN-based LED’s have been demonstrated with highly defective crystals. Although luminescence is observed in highly defective crystals, the most efficient light emitting regions of the crystal are those with the lowest defect densities. In order to decrease the defect density, different substrates or new methods of growth need to be explored.

The ideal substrate for epitaxial GaN would be bulk GaN, but to date the largest bulk GaN crystals are only ~100 μm thick, with lateral dimensions on the order of 3 – 5 mm.[49] In comparison, the typical diameter of sapphire and SiC substrates is 2" (50 mm). Very thick HVPE layers 10 – 300 μm thick have been grown for use as pseudo-bulk substrates. These thick HVPE layers have high defect densities near their interface with the sapphire substrates on which they are grown, but many of these defects annihilate each other as the growth continues, so that the upper portion on which the epitaxial layers are grown have defect densities of 10^6 cm^{-2} or less.[50]

Another method for growth of material with immeasurably low defect densities is currently receiving much attention.[51] This method is called “epitaxial lateral overgrowth,” or ELOG. ELOG involves first growing a thin layer of GaN, then patterning an SiO_2 or Si_3N_4 mask on top of it. When returned to the growth chamber, nucleation of GaN occurs on the GaN between the masked surfaces, and not on the mask itself. The GaN grows upward and also under some conditions can be made to grow outward across the mask (overgrowth). The defect density of the overgrown GaN is significantly lower than that of the GaN in the region of the mask windows, except where the growth fronts meet. The optical quality of films produced using the ELOG method is much better than that produced by traditional epitaxial methods, due not only to a reduction in defect density but also to strain relaxation.[52] By a combination of ELOG and HVPE methods, it appears that the barriers to the development of GaN-based lasers caused by high defect densities may soon be overcome.

The second major hurdle is decreasing the resistance of GaN-based laser diodes. The minimum voltage required to operate an LED or LD is the potential required to raise an electron from the valence band to the conduction band, which is approximately 3.4 V for GaN.[19] The lowest actual operating voltage for GaN-based lasers is currently around 5.5 V, as can be seen in Figure 1.3.2. The two main contributors to the high operating voltage are a large potential drop associated with poor ohmic contacts to p-type GaN[53] and high resistivities of p-type GaN and the AlGaN cladding layers.[54]

One method that has been presented for improving the electrical properties of p-type GaN is the incorporation of superlattice doping.[55] Compositional modulation of a uniformly doped AlGaN/GaN superlattice can enhance the acceptor activation by more than one order of magnitude. Further work focusing on increasing the conductivity of AlGaN and p-type GaN and decreasing the resistance of ohmic contacts to p-type GaN will help to decrease the operating voltages. In addition, the MQW structures that are currently used introduce potential barriers that carriers must cross before recombination.[56] The use of single quantum well and double heterostructure designs for LD's could therefore reduce the operating voltages significantly. [57]

The third major hurdle to commercialization of III-V Nitride LD's is developing methods for fabricating smoother laser facets. Lasers require reflective mirrors, or facets, that provide feedback. The performance of the laser, measured in terms of power and sharpness of far field pattern, depends strongly on how well the light is reflected from the facets. In Section 2.3 it will be shown that the reflectivity of a laser facet decreases exponentially with the square of its root-mean-square (RMS) roughness.[58] Typical roughnesses for GaN-based lasers are 16 nm for cleaved facets on sapphire substrates[57] and 5 – 50 nm for dry-etched facets.[35,59,60] In order to achieve reflectivities greater than 90% of the theoretical maximum, facets with a roughness of less than 4 nm are required.[58] It is overcoming this third hurdle that this work has focussed upon, and that will be discussed at length in this dissertation.

2. Laser theory

2.1. Luminescence

Semiconductor lasers consist of an optical gain medium in a resonant cavity. While most materials absorb light, an optical gain medium can be *pumped* optically or electrically into a nonequilibrium state in which it amplifies light. The resonant cavity provides feedback for the amplified light, allowing a laser oscillation to develop. In this chapter I will discuss the luminescence properties of semiconductors in general and GaN in particular, the origins of stimulated emission, and the design of optical resonators.

Luminescence occurs in direct-gap[b] semiconductors when electrons drop from one energy level to a lower one, analogous to an electron dropping from one orbital to another in a single atom. If energy greater than the semiconductor bandgap is transferred to an electron at the top of the valence band, an electron-hole pair can be generated, *i.e.*, the electron can be raised from the valence band into the conduction band. The electron and hole can then recombine, releasing energy in the form of luminescence. There are four basic types of luminescence from semiconductors, distinguished by the source of input energy: (1) photoluminescence with excitation by optical radiation, (2) cathodoluminescence by an electron beam, (3) radioluminescence by other fast particles or high-energy radiation, and (4) electroluminescence by electrical current.[61] Lasers are usually operated by optical or electrical excitation; this work focuses on optical excitation.

---

[b] A *direct-gap* semiconductor is one for which an electron at the valence band maximum has the same momentum as an electron at the conduction band minimum.

The basic types of transitions for a semiconductor are shown in Figure 2.1.1. The transitions in the figure are labeled as follows: (a) band-to-band, or near-bandgap transitions, (b) conduction band to acceptor, (c) donor to acceptor, (d) donor to valence band, and (e) deep levels. Any or all of these transitions can produce luminescence in GaN.

Near-bandgap luminescence often involves *excitons*. An exciton is an electron and a hole which are orbiting one another in a Hydrogen-like fashion. The energy of an electron in such a configuration is equal to the conduction band energy minus a small *binding energy*, where the binding energy is the energy required to spatially separate the electron-hole pair. Some excitons are localized on or near a single atom in the semiconductor; these are called Frenkel excitons, and their energies are closely related to the atomic transitions of the single atom.[62]

Weakly bound excitons are not associated with a single atom in the crystal. The energy of these electrons can be calculated using a modified Rydberg equation:

$$E_n = E_{\mathbf{g}} - \frac{\mu e^4}{2\hbar^2 \varepsilon^2 n^2}. \qquad \textbf{Equation 2.1.1}$$

Here n is the principle quantum number, μ is the reduced mass of the electron-hole pair, e is the elementary charge, and ε is the dielectric constant of the material. The binding energy is the second term on the right-hand side of the equation. For GaN, $\varepsilon \approx 9$,[19] $m_e^* = 0.2\ m_0$,[19] and $m_h^* = 0.26\ m_0$.[63] This gives a binding energy of 19 meV for the ground state of the exciton.

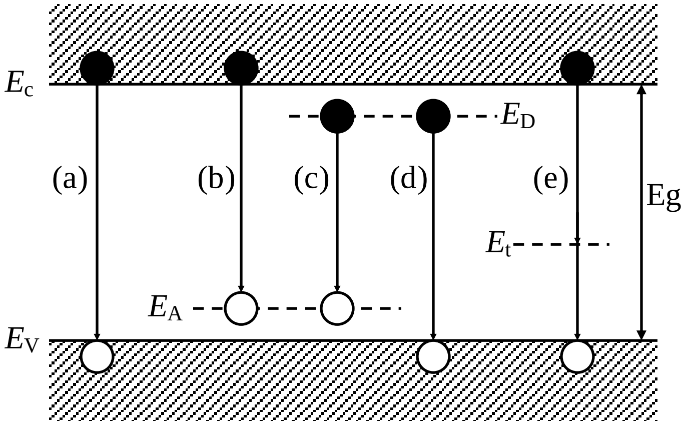

Figure 2.1.1: Basic transitions in a semiconductor. E_C, E_V, E_A, E_D, E_t, and E_g are the energies of the conduction band, the valence band, an acceptor, a donor, a trap, and the bandgap, respectively.

Typical Si-doped n-type GaN and Mg-doped p-type GaN photoluminescence spectra obtained while using a HeCd laser (λ = 325 nm) excitation source are shown in Figure 2.1.1 and Figure 2.1.3, respectively. Both spectra show near-bandgap luminescence, which has been interpreted as either a donor-to-valence-band transition[64] or an excitonic transition.[65,66] The Si-doped n-type GaN shows a broad "yellow" luminescence which is caused by deep levels,[67,68] possibly associated with defects in the crystal structure at grain boundaries[69] or with gallium vacancies.[70,71] The intensity of the yellow luminescence has also been studied as a function of the n-type doping concentration, revealing that it is caused by a compensating center.[72] Wright and Grossner[73] have recently predicted that threading dislocations, which are found predominantly at grain boundaries, are stabilized by the formation of gallium vacancies under some growth conditions. This could unify the two current lines of thought concerning the origin of the yellow luminescence, in that the luminescence may come from gallium vacancies at grain boundaries.

The photoluminescence from a Mg-doped p-type GaN in Figure 2.1.3 shows no yellow luminescence, but a peak at 3.05 eV associated with donor-acceptor pairs. Other Mg-doped p-type samples have had donor-acceptor pair peaks in the energy range between 2.95 eV and 3.1 eV, which is consistent with the values observed by other groups.[74-77]

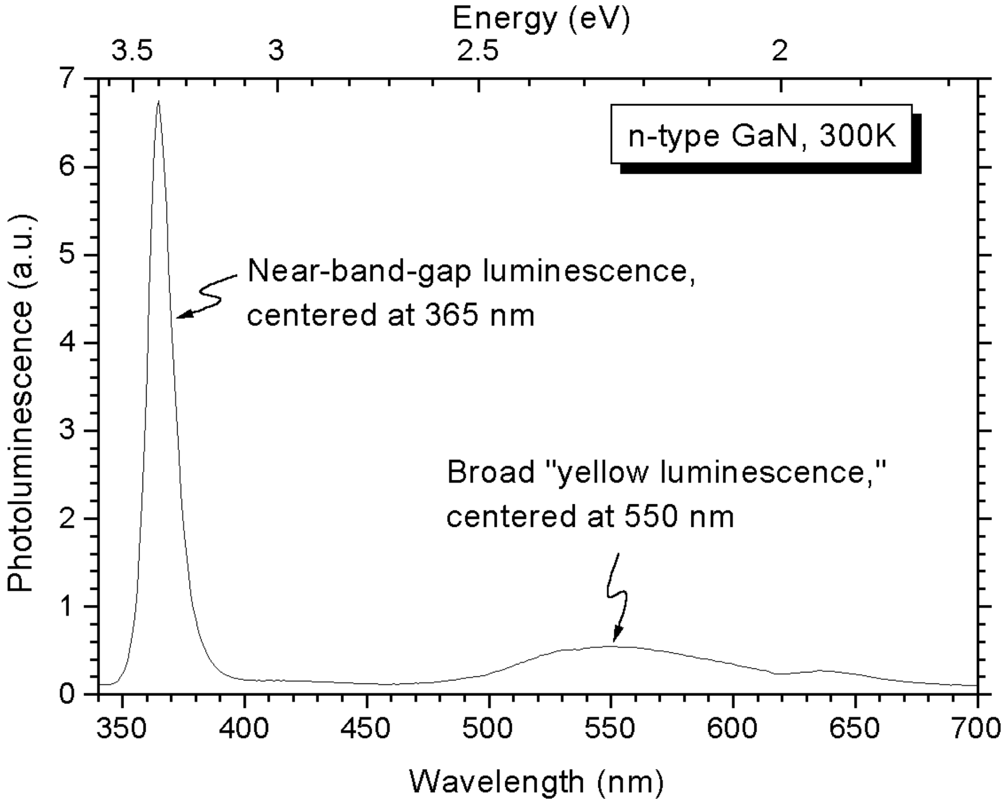

Figure 2.1.2: Typical photoluminescence spectrum of n-type GaN showing near-bandgap and "yellow" luminescence.

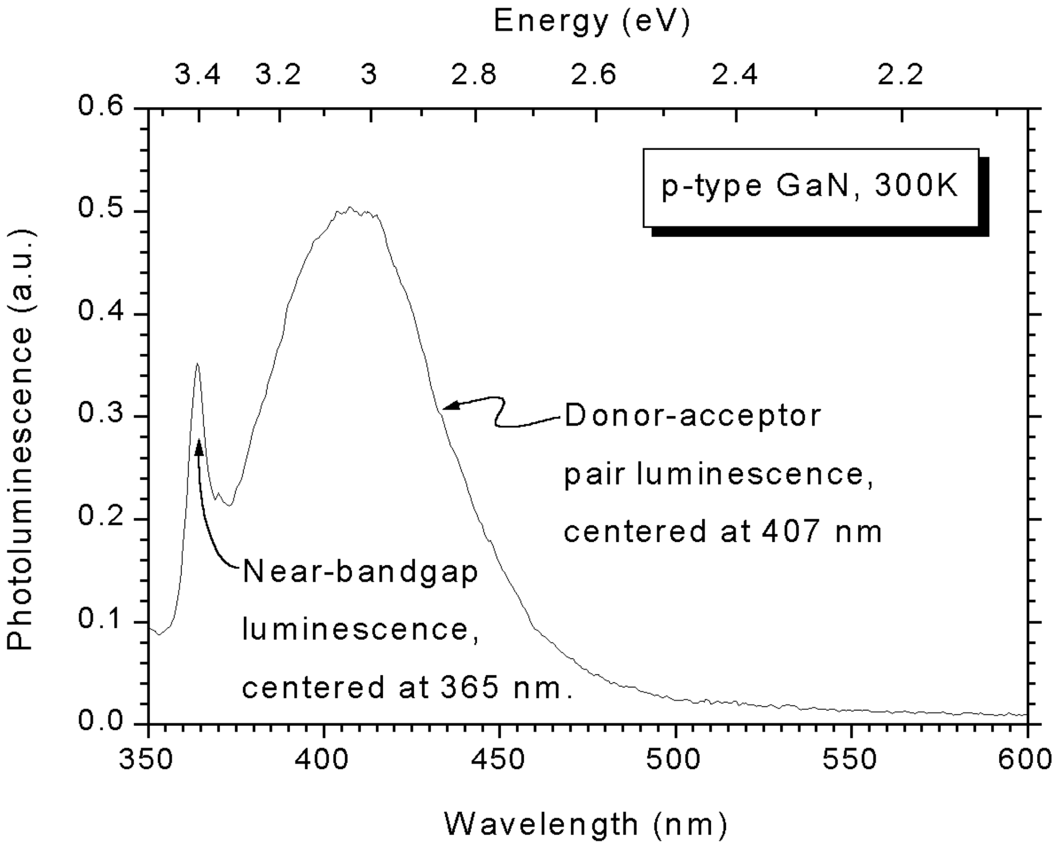

Figure 2.1.3: Typical photoluminescence spectrum of Mg-doped p-type GaN showing near-bandgap and donor-acceptor pair luminescence.

2.2. Stimulated emission

All of the transitions referred to in Section 2.1 were considered from the standpoint of spontaneous emission, that is, an electron and a hole combining and releasing energy in the absence of an external stimulus, as illustrated in Figure 2.2.1(a). In fact, there are two other types of transitions that should be considered along with spontaneous emission: absorption and stimulated emission. The concept of absorption is a familiar one: light passes through a material, and the material absorbs some of the light, so that the intensity of the light coming out of the material is less than the intensity of the light that went in. The primary mechanism for absorption is illustrated in Figure 2.2.1(b). An incoming photon with an energy larger than the bandgap energy $E_g = E_C - E_V$ gives its energy to an electron, raising it from the valence band to the conduction band. The third important type of transition, stimulated emission, is illustrated in Figure 2.2.1(c). This occurs when a photon with an energy approximately equal to E_g interacts with an electron in the conduction band, stimulating the electron to drop into a hole in the valence band. This process releases a second photon with the same phase and frequency as the first photon.

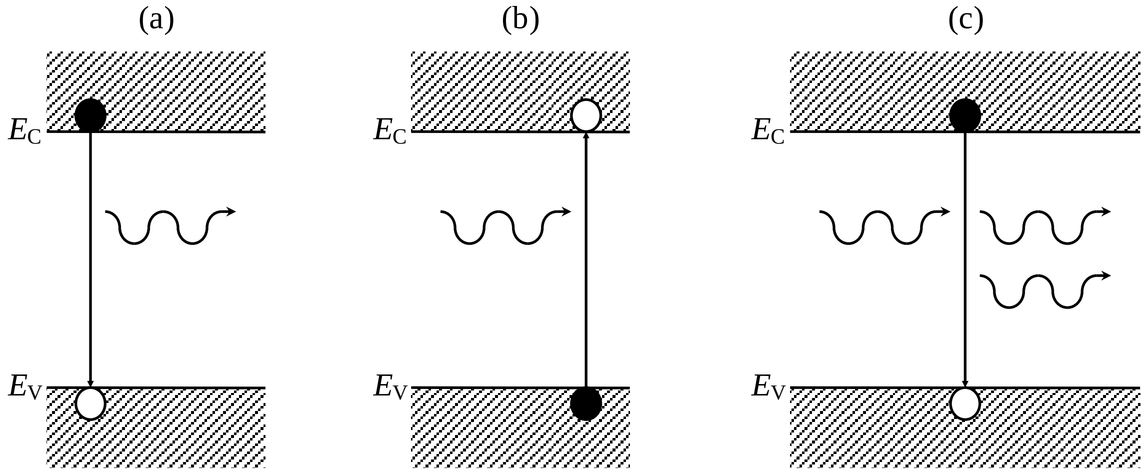

Figure 2.2.1: Radiative transitions: (a) spontaneous emission, (b), absorption and (c) stimulated emission.

Stimulated emission was first postulated by Einstein, who considered the rates of electron transitions in single atoms. He defined A and B coefficients which refer to the spontaneous and stimulated processes, respectively. For a system in equilibrium, the sum of the transition rates between state "1" and higher energy state "2" is equal to zero:

$$\frac{\mathbf{d}N_1}{\mathbf{d}t} = -\frac{\mathbf{d}N_2}{\mathbf{d}t} = A_{21}N_2 + B_{21}W(\nu)N_2 - B_{12}W(\nu)N_1 \qquad \textbf{Equation 2.2.1}$$

The coefficients A, B_{21}, and B_{12} are associated with spontaneous emission, stimulated emission, and absorption, respectively, and so they are weighted with the radiation spectral density $W(\nu)$. The subscripts on B_{12} and B_{21} are intended to prevent confusion when doing calculations, to make it easier to differentiate between absorption and stimulated emission; in fact, their values are equal for any given system. When dealing with semiconductors, there are not only two states as there are in single atoms. Instead, a continuum of states must be taken into consideration. Generally, the emission of semiconductors is referred to not in terms of A and B coefficients, but in terms of spontaneous emission, absorption, and optical gain. For a detailed discussion of Einstein's A & B coefficients and how to relate them to the optical parameters commonly used with semiconductors, see Appendix 6 of L. A. Coldren and S. W. Corzine's *Diode Lasers and Photonic Integrated Circuits*, John Wiley & Sons, Inc., New York (1995).

In order for stimulated emission to outweigh absorption in a material, the second term on the right-hand side of Equation 2.2.1 must be larger than the third term on the right-hand side. Because $B_{12} = B_{21}$, this means that the number of electrons in the higher energy state must be greater than the number in the lower energy state. According to Boltzmann statistics, this can not happen under equilibrium conditions. For this reason, an external pumping source is needed to cause population inversion, wherein the number of electrons in the excited state is greater than the number of electrons in the lower, ground state. In a laser, the region where population inversion occurs is called the active region. This region contains a material that has been excited either electrically or optically into a nonequilibrium state where the amplification of light exceeds the absorption.

The intensity of the light in an absorbing medium decreases exponentially in space:

$$I(x) = I_0 \mathrm{e}^{-\alpha x}, \qquad \textbf{Equation 2.2.2}$$

where $I(x)$ is the intensity of the light, x is the position in space, with the light traveling in the $+x$ direction, I_0 is the initial intensity at $x = 0$, and α is the absorption coefficient. Gain acts as a negative absorption in the material, so that the intensity of the light increases exponentially as it passes through the medium:

$$I(x) = I_0 \mathrm{e}^{gx}, \qquad \textbf{Equation 2.2.3}$$

where g is the optical gain of the material. Any real material with optical gain also has absorption. The net result when both gain and absorption are taken into effect is

$$I(x) = \left(I_0 e^{gx}\right) e^{-\alpha x} = I_0 e^{(g-\alpha)x} \equiv I_0 e^{g_{\text{net}} x}, \qquad \textbf{Equation 2.2.4}$$

where the net optical gain g_{net} is defined as $(g-\alpha)$.

Shaklee *et al.*[78] developed a method for determining the optical net gain (the net gain during optical pumping) by a "variable stripe length method," which is illustrated in Figure 2.2.2. The magnitude of the edge emission is monitored while the illuminated stripe length is varied systematically. The output intensity I, in arbitrary units, as a function of stripe length l can be derived using Figure 2.2.3. The increase in intensity $\mathrm{d}I(x)$ is given by

$$\mathrm{d}I(x) = (g-\alpha) I(x)\mathrm{d}x + C\mathrm{d}x, \qquad \textbf{Equation 2.2.5}$$

where C is a constant representing the spontaneous recombination. Integration by parts then gives

$$\int_0^l \frac{\mathbf{d}I(x)}{I(x)g_{\mathbf{net}} + C} = \int_0^l \mathbf{d}x. \qquad \textbf{Equation 2.2.6}$$

Evaluation of this integral yields

$$\frac{\ln\left|I(l)g_{\text{net}} + C\right|}{g_{\text{net}}} - \frac{\ln\left|I(0)g_{\text{net}} + C\right|}{g_{\text{net}}} = l. \qquad \textbf{Equation 2.2.7}$$

The intensity at $x = 0$ is zero, because no light is traveling in the $+x$ direction at this point. Setting I(0) = 0 and rearranging this equation yields the following expression for light emitted when using the variable stripe length method:

$$I(l) = \frac{C}{g_{\mathbf{net}}}\left(\mathbf{e}^{g_{\mathbf{net}} l} - 1\right). \qquad \textbf{Equation 2.2.8}$$

By plotting the intensity as a function of stripe length, it is possible to determine the net optical gain of the material.

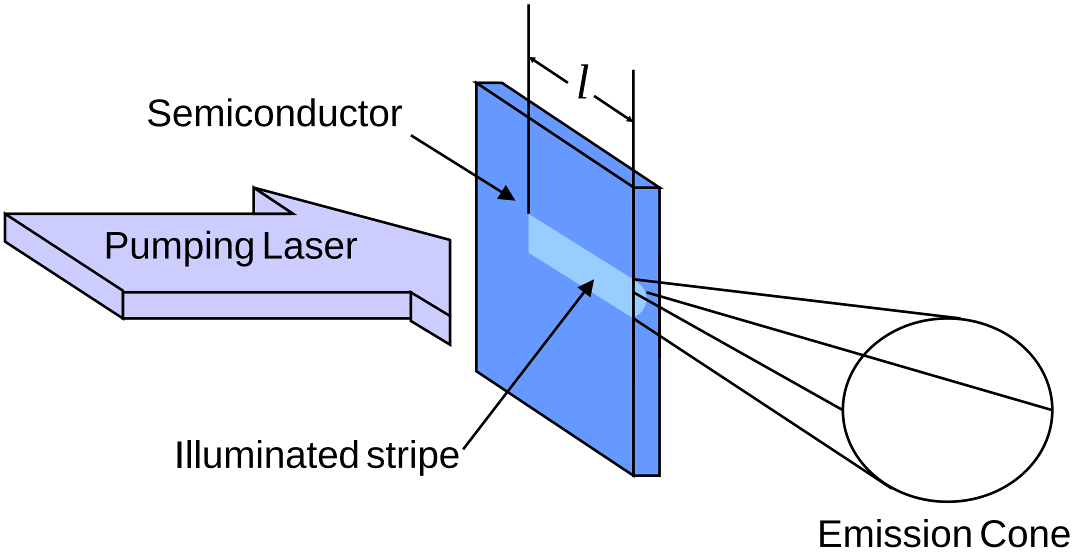

Figure 2.2.2: Schematic of the "variable stripe length method" for determining the net optical gain of a semiconductor.

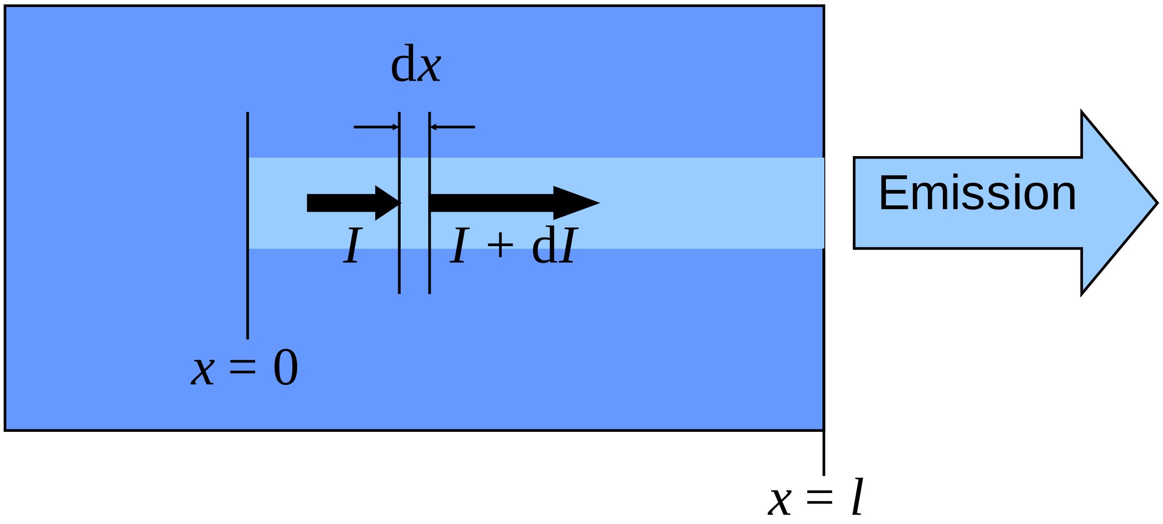

Figure 2.2.3: Schematic for the derivation of the output intensity as a function of stripe length for the variable stripe length method.

The net optical gain of InGaN/GaN double heterostructures has been determined by using this method with a N_2 laser (λ = 337.1 nm) excitation source. The details of this structure and its growth will be described in Section 7.1. The pumping power density was measured by using a high-speed detector. The most uniform area of the laser was focused on a slit 1mm wide by 200 μm long defined by razor blades. The detector was used to measure the energy of a single pulse from the N_2 laser after it has passed through the slits. This value was divided by the length of the pulse as given by the laser specifications, 800 ps to give a pumping power, and then divided by the area of the slit to give a pumping power density. The slit was imaged on the sample at a magnification factor of 1, so that the size of the illuminated bar on the sample was the same as the size of the slit. The data for the experiment, shown in Figure 2.2.4, gives a net optical gain of 97 cm^{-1} at an incident pumping power density of 9.8 MW/cm^2. Note that the exponential behavior of the data extends over nearly five orders of magnitude. This value is in good agreement with typical values of 80 – 210 cm^{-1} reported in the literature for the net optical gain of (In,Al)GaN structures.[79-82]

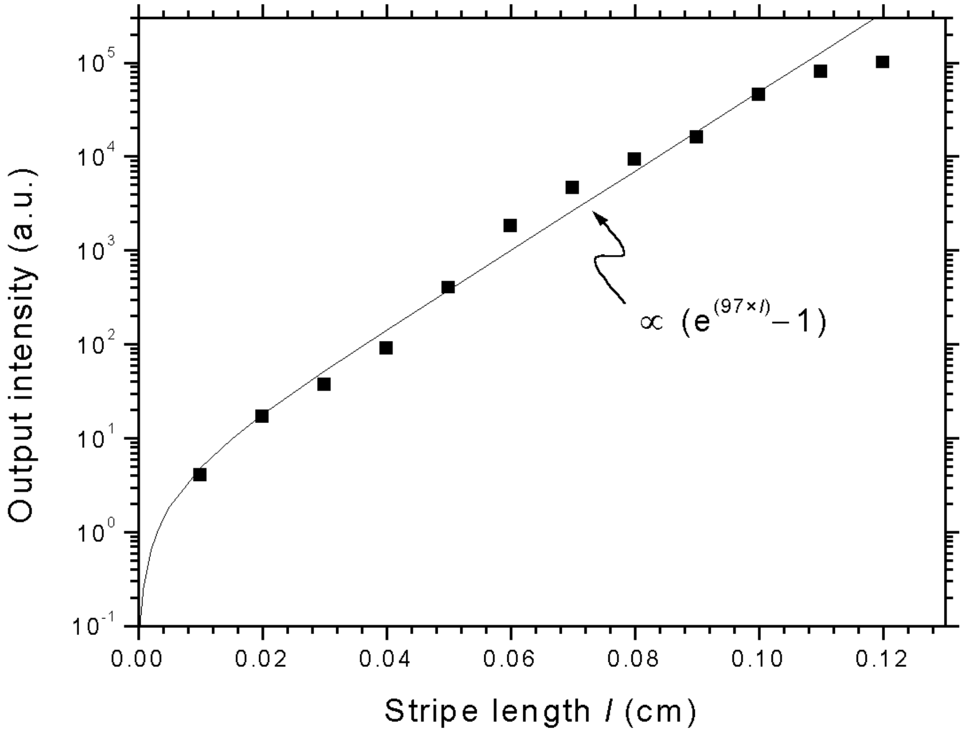

Figure 2.2.4: Room temperature net optical gain measurements using the variable stripe length method on an InGaN/GaN double heterostructure at an incident pumping power density of 9.8 MW/cm^2.

2.3. Optical feedback

As was mentioned in Section 2.1, a laser cavity requires not only net optical gain but also an optical resonator. An optical resonator is usually made by placing the optical gain region between two mirrors, or *facets*. The facets reflect the light back and forth through the active region, creating standing waves in the cavity. The output of the laser exits through one or both of the partially reflecting facets. In order for laser action to occur, there must be *round trip net gain* in the cavity. This means that the gain must outweigh not only the absorption but also all other losses. Consider a light wave with an intensity I_1 travelling to the right (+x direction) from the left mirror at the point labeled "1" in Figure 2.3.1. According to Equation 2.2.4, when it reaches point "2," the intensity will have increased to $I_1 \times e^{(g-\alpha)L}$, where L is the length of the active region. Upon reaching the first facet, some of the light is transmitted, some is reflected, and some is scattered. The intensity reaching point "3" is the intensity at point "2" multiplied by the power reflectivity R of the mirror. For simplicity, we will consider a symmetrical laser cavity, where the facets are identical. In this case, the net gain from one round trip through the cavity (1 → 2 → 3 → 4 → 1) would be

$$e^{(g-\alpha)L} \times R \times e^{(g-\alpha)L} \times R = R^2 e^{2(g-\alpha)L}. \qquad \textbf{Equation 2.3.1}$$

At threshold, for the round trip net gain is unity. To reach threshold, the reflectivity of the facets must be

$$R = e^{-(g-\alpha)L}. \qquad \textbf{Equation 2.3.2}$$

This relationship shows that for a given facet reflectivity and net optical gain there is a minimum cavity length for laser action to occur. In the case of the InGaN/GaN heterostructures used for fabricating laser cavities, the net optical gain at an incident pumping power of 9.8 MW/cm^2 is 97 cm^{-1}. For uncoated facets, the reflectivity at normal incidence can be derived from Fresnel's equations. At normal incidence, this gives

$$R = r^2 = \left(\frac{\bar{n}_1 - \bar{n}_2}{\bar{n}_1 + \bar{n}_2}\right)^2, \qquad \textbf{Equation 2.3.3}$$

where r is the electric field amplitude reflectivity and $\bar{n}_1$ and $\bar{n}_2$ are the refractive indices of the semiconductor and air, respectively. The GaN refractive index is 2.54 at 395 nm, the emission wavelength of our laser structures.[83] This gives a power reflectivity $R = 0.18$ for uncoated facets. Thus, using Equation 2.3.2, the minimum cavity length for laser action to occur in this structure with an optical pumping power of 9.8 MW/cm^2 is approximately 175 μm.

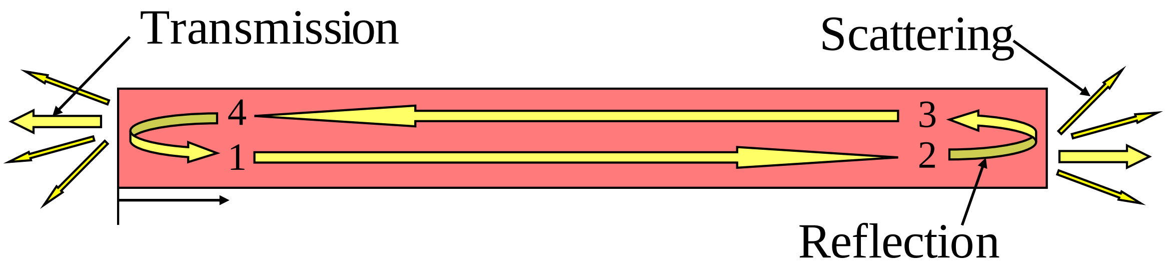

Figure 2.3.1: Schematic of the active region of a laser, demonstrating optical feedback.

Equation 2.3.2 can also be used as a guide for determining optimal laser cavity lengths. Pumping power threshold decreases monotonically as the cavity length is increased. Beyond a certain point, however, increasing the cavity length has a negligible effect on the threshold. This can be seen by rearranging Equation 2.3.2 to solve for the gain at threshold :

$$g = \alpha - \frac{\ln(R)}{L}. \qquad \textbf{Equation 2.3.4}$$

Noting that R is always less than 1, the second "mirror loss" term is always positive, so the gain at threshold decreases as the cavity length increases. According to the "linear gain model," the optical gain is proportional to the pumping power. Therefore, the pumping power threshold decreases as the cavity length increases. This effect becomes small, however, when the absorption term becomes large compared to the mirror loss term. An optimal cavity length would therefore be such that these two terms are approximately equal. If the facets are coated with high-reflectivity coatings, the optimal cavity length decreases. On the other hand, if the mirrors are not smooth scattering can become a significant problem, decreasing the reflectivity of the facets and increasing the optimal cavity length.

A facet roughness analysis for semiconductor lasers with step-like surfaces is described in Ref. 84. This model shows that the reflectivity decreases significantly even for surfaces that are commonly considered "optically flat" with a roughness of $\lambda/10$. For a step size as small as $\lambda/10$, the reflectivity is only 90% of the value for a perfectly smooth reflector. For a GaN-based laser with $\lambda \approx 400$ nm, the wavelength inside the laser cavity is only 157 nm, so $\lambda/10$ is 15.7 nm. Except for some cleaved facets, which will be described in detail in Section 4.2, the roughness of GaN-based laser facets is not step-like, so this model can not be used to determine the effect of the roughness on reflectivity.

For this reason, a mathematical model is developed here which gives the reflectivity of facets with Gaussian roughness distributions, when the scale of the roughness is shorter than the wavelength. An example of a surface morphology with which this model can be used is shown in Figure 2.3.2. In the upper part of the figure is a perfectly smooth surface. The dotted semicircles above this surface represent Huygen's elementary waves which have been reflected from an incident plane wave. With a smooth surface, these waves add to make a smooth specularly reflected wavefront. In the lower part of the figure is a rough surface, where the length scale of the roughness is shorter than the wavelength of the light. In this case there is no clear specular wavefront in the Huygen's waves after reflection.

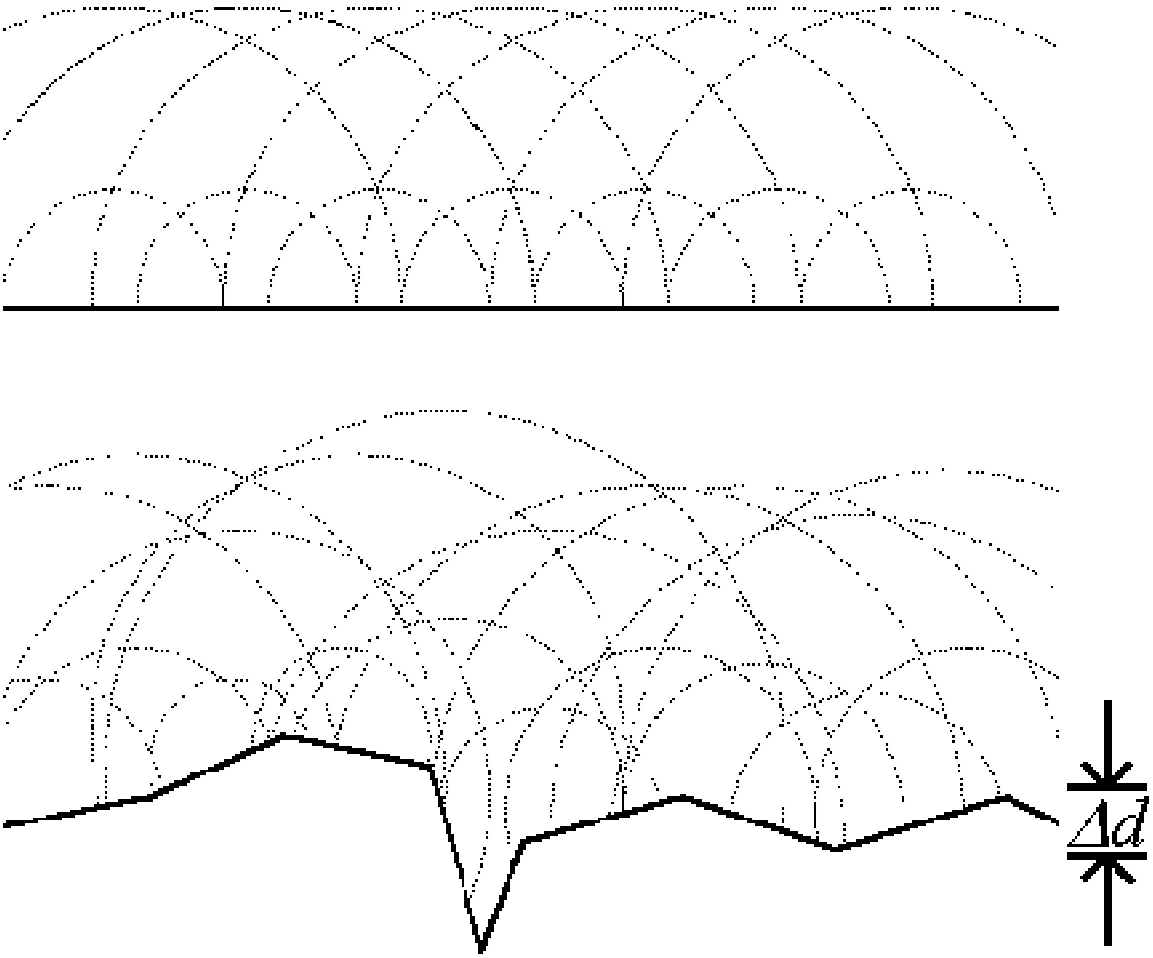

Figure 2.3.2: Sample surface for mathematical model of reflectivity as a function of roughness. The arcs represent the wavefronts of Huygen's elementary waves generated by the reflection of plane waves from the surfaces.

The reflected wave is taken to be a superposition of Huygens elementary waves generated at the surface of the laser facet. Because the model is being applied to a laser cavity, only the specular, normal-incidence reflection is considered. A facet with an RMS roughness Δd that follows a gaussian distribution is assumed. If the surface has a step-like structure, such an assumption would not be valid, but for the surface morphologies normally observed with GaN-based laser facets (images of these surfaces will be presented in Chapters 2 – 5), such an assumption is acceptable. The roughness of the facet causes phase differences in the elementary waves generated at the surface, broadening the phase of the reflected wave by

$$\Delta\phi \quad = \quad \frac{4\pi\,\bar{n}\,\Delta d}{\lambda_0}, \qquad \textbf{Equation 2.3.5}$$

where $\bar{n}$ is the refractive index of the semiconductor and λ_0 is the emission wavelength in vacuum. For an incident wave with an electric field magnitude U_0, the reflected wave is a superposition of all of the reflected elementary waves, which have a gaussian phase shift distribution. The distribution of phases can be thought of as being centered about the normal phase shift for a wave reflecting from a perfectly smooth surface. The magnitude U of the reflected wave as a function of phase shift ϕ has a standard deviation ($\Delta\phi$) and is dependent upon the incident magnitude U_0, the amplitude reflection coefficient r, and the phase broadening $\Delta\phi$:

$$U(\phi) \quad = \quad \frac{U_0\, r}{\sqrt{2\pi}\,(\Delta\phi)}\,\mathrm{e}^{-\phi^2/2(\Delta\phi)^2}\,. \qquad \textbf{Equation 2.3.6}$$

Because the wave is monochromatic, the superposition of all of the elementary waves in this distribution of phase shifts results in a wave with a magnitude U_f. U_f is obtained by integrating over $U(\phi)$ multiplied by the phase factor $\mathrm{e}^{\mathrm{i}\phi}$:

$$U_f \quad = \quad \int_{-\infty}^{\infty} U(\phi)\,\mathrm{e}^{\mathrm{i}\phi}\,\mathrm{d}\phi \quad = \quad U_0\, r\,\mathrm{e}^{-(\Delta\phi)^2/2}\,. \qquad \textbf{Equation 2.3.7}$$

The reflected amplitude for a perfectly smooth facet is simply $U_{(\Delta\phi\,=\,0)} = U_0 r$. The exponential factor in Equation 2.3.4 is interpreted as a decrease in the amplitude reflectivity r. Substituting Equation 2.3.4 into Equation 2.3.6, we find that the ratio of the power reflectivity of a rough facet to the power reflectivity of a perfectly smooth facet is given by

$$\frac{R(\Delta d)}{R_0} = \mathrm{e}^{-16\pi^2 (n\Delta d/\lambda_0)^2}\,, \qquad \textbf{Equation 2.3.8}$$

where R_0 is defined as the reflectivity of a perfectly smooth facet as given by Equation 2.3.3.

The model was verified by examining the intensity of a HeNe laser ($\lambda_0 = 633$ nm) reflected off of a roughened glass slide. One side of the glass slide was roughened using a polishing wheel with 3 μm grit paper. One end of the slide was pressed into the polishing wheel while the other was allowed to rise off of the paper. In this way, the roughness was graded from one end of the slide to the other. A profilometer was used to measure the roughness at various points along the length of the glass slide.

A HeNe beam was reflected from the roughened surface at near-normal incidence and the intensity of the reflection was measured using a silicon detector. The width of the collection cone of the detector when viewed from the glass slide was approximately 0.02°. The reflections off of the front and back surfaces of the glass slide are taken into consideration. The detector was positioned in the brightest spot of the reflection for each measurement so that the front and back reflections could be taken to add constructively. The results of this experiment are shown in Figure 2.3.3, along with the theoretical curve. The values in this figure are normalized so that $R/R_0 = 1.0$ corresponds to the maximum signal observed for an unroughened surface.

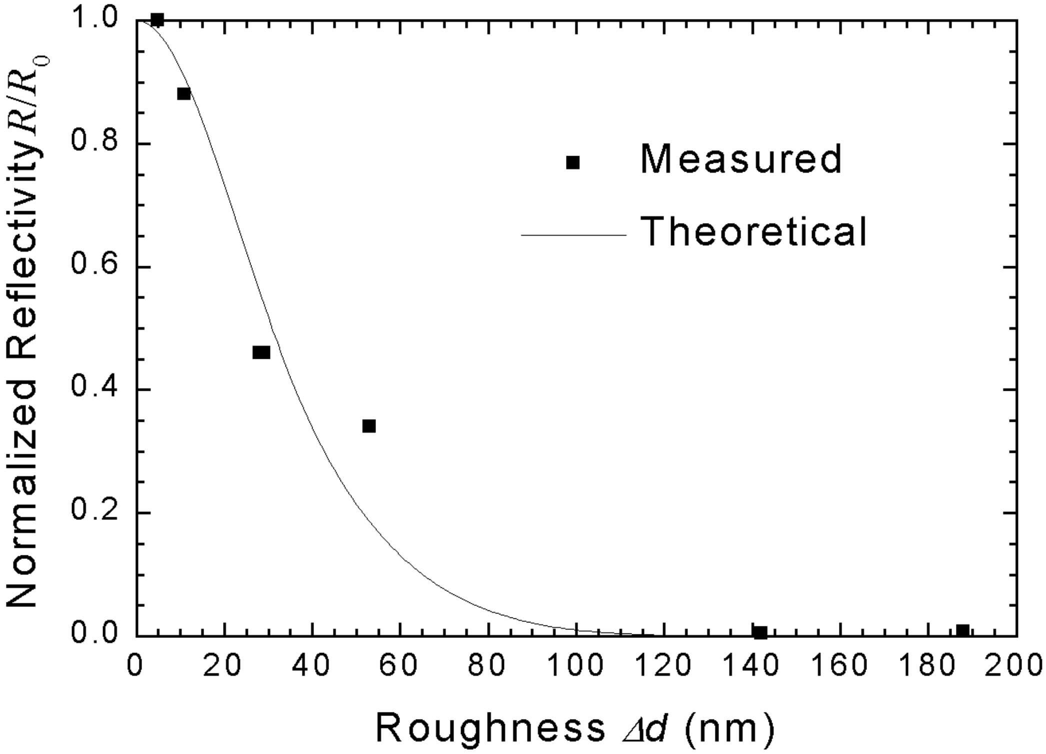

Figure 2.3.3: Power reflectivity of glass as a function of surface roughness for $\lambda_0 = 633$ nm. R_0 is the experimental reflectivity for an unroughened surface.

The theoretical model is next applied to the InGaN/GaN laser structure with an emission wavelength of 395 nm. The normalized reflectivity of a GaN surface as a function of surface roughness is shown in Figure 2.3.4, along with published roughness measurements on GaN-based laser structures. In order to achieve reflectivities of greater than 90%, facets with an RMS roughness of less than 4 nm are required.

This mathematical model was calculated only for specular reflections; scattered light was taken to be lost. In a laser cavity, however, waveguiding occurs, which allows some scattered light to remain within the active region. For an extremely rough surface, the reflected light can be taken to be scattered uniformly throughout a solid angle of 2π. In the laser structures used here, the angle of propagation of the guided mode is 9°, so any light scattered within an 18° acceptance angle in the vertical direction remains within the cavity. In the horizontal direction, the acceptance angle depends upon the dimensions of the cavity; for a typical 500 μm length and a 200 μm width, this acceptance angle is 22°. Thus, the minimum reflectivity for an extremely rough surface would be approximately 0.02. So, while the curve in Figure 2.3.4 drops to near zero as the roughness increases, there is actually minimum value on the order of 0.02 for very large roughnesses. In the next chapters the methods used for fabricating GaN-based lasers and the quality of the facets achieved by each method will be discussed.

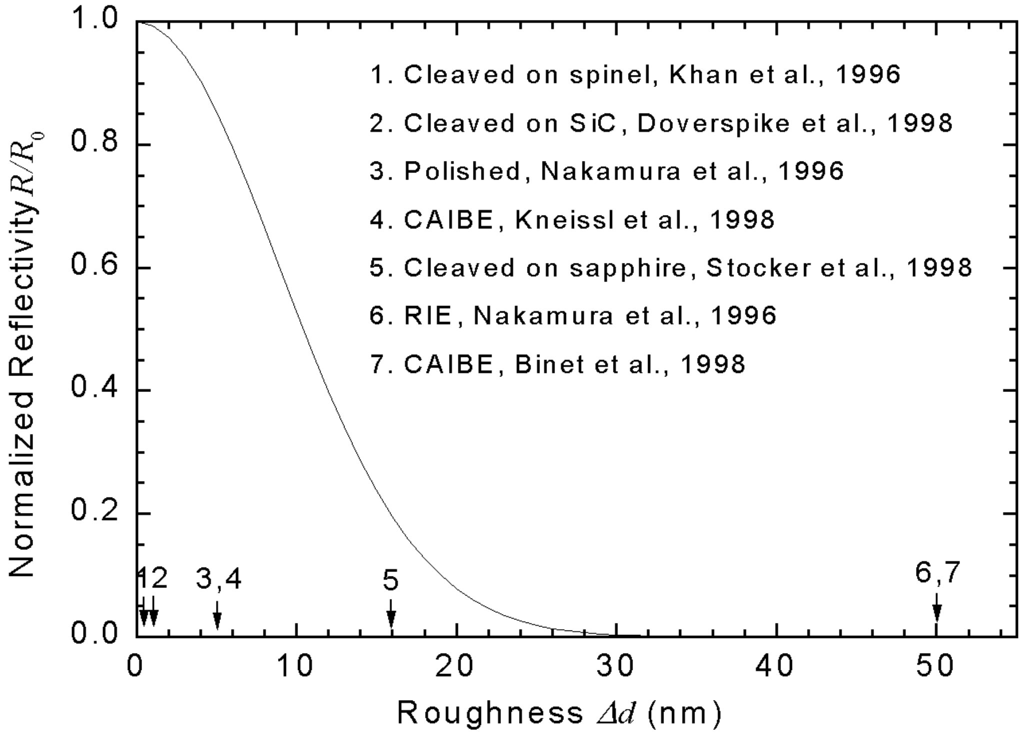

Figure 2.3.4: Power reflectivity of InGaN/GaN laser facets as a function of surface roughness for λ_0 = 395 nm. R_0 = 0.19 is the reflectivity of a perfectly smooth facet as given by the Fresnel equations.

3. Dry Etching

3.1. Reactive Ion Etching (RIE)

The simplest dry etching technique, one that is widely used in silicon and gallium arsenide technology, is reactive ion etching (RIE). A simple schematic of a reactive ion etching system is shown in Figure 3.1.1. The sample is placed in a vacuum chamber on an electrode that can be driven by a radio frequency (RF) source. A reactive gas is then fed into the chamber, and the RF field strips the outer electrons from the gas molecules, forming a plasma. In addition to the rapidly oscillating RF field, a bias voltage also develops between the upper and lower electrodes, due to the accumulation of negative charge on the lower electrode. While both electrons and positive ions can be driven to the electrodes by the RF field, the electrons have a larger amplitude of motion due to their smaller mass. As a result, negative charge is imparted to both electrodes. The upper electrode is grounded, so the negative charge drains off of it as quickly as it arrives. The lower electrode, however, has a blocking capacitor which prevents charge from leaking to ground. The resulting bias voltage drives the positively charged ions down onto the surface of the sample. Highly anisotropic etching can result from the combination of physical and chemical etching processes at the sample surface.

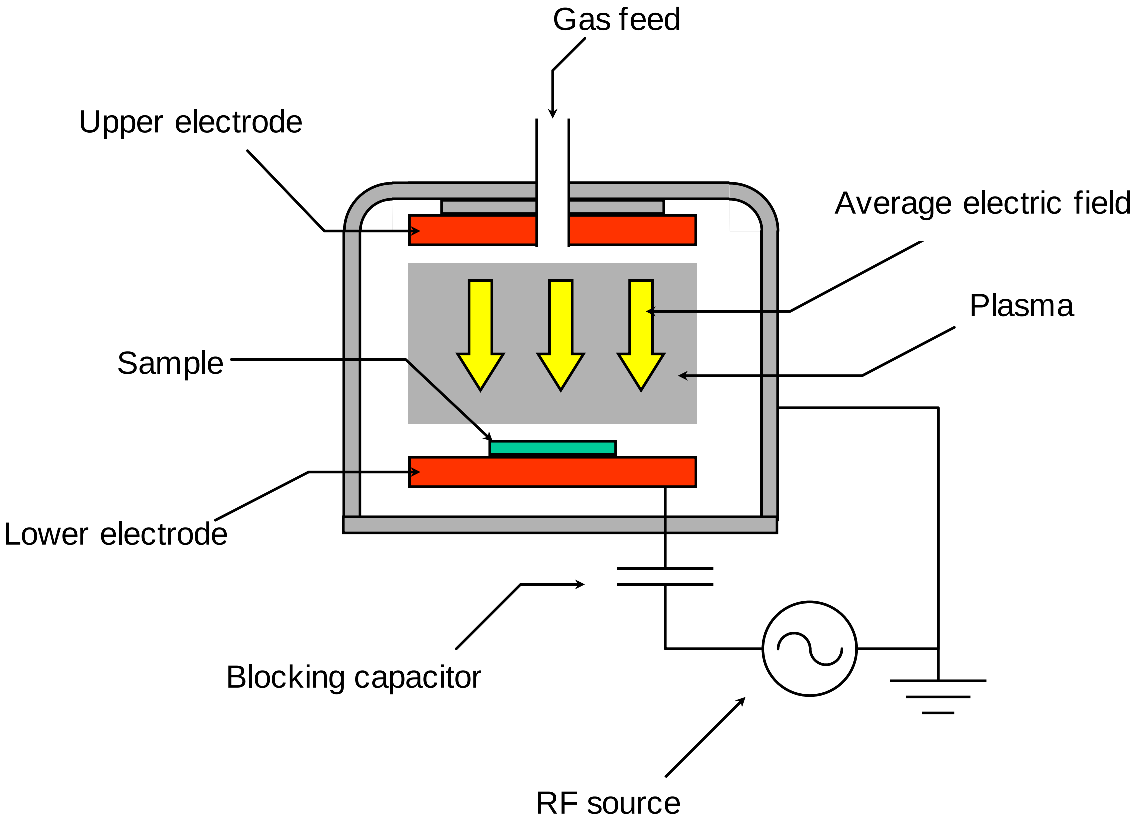

Figure 3.1.1: Schematic of a reactive ion etching system

For reactive ion etching of GaN, the most effective plasmas are chlorine-, bromine-, or fluorine-based. The nitrogen is removed as NCl, while the gallium is removed as $GaCl_3$, $GaBr_3$, or GaF_3.[85] Due to the chemical and physical stability of GaN, high-RF-power etches are required, on the order of 200 – 500 W. RIE etch rates as high as 50 – 60 nm/min have been achieved, with sidewall angles of 60 – 78°.[86-89] In all cases, the rms sidewall roughness is on the order of 100 nm.

In this study, the best RIE results (*i.e.* the highest etch rates and most vertical walls) were achieved using an SiO_2 etch mask in a 200 W Cl_2 plasma at a flow rate of 10 sccm and a pressure of 8 mTorr. The thickness of the masks was approximately 0.3 μm, and the selectivity was such that the GaN etched roughly three times faster than the SiO_2. No etching is observed in the first twenty minutes under these conditions, and then etching begins to occur at 18 nm/min, as can be seen in Figure 3.1.2. The twenty-minute period before etching begins may be due to a heating effect, the etching process beginning only when the sample has been heated significantly by the plasma. However there is no provision to monitor the temperature of the sample during the etching process in order to verify this hypothesis.

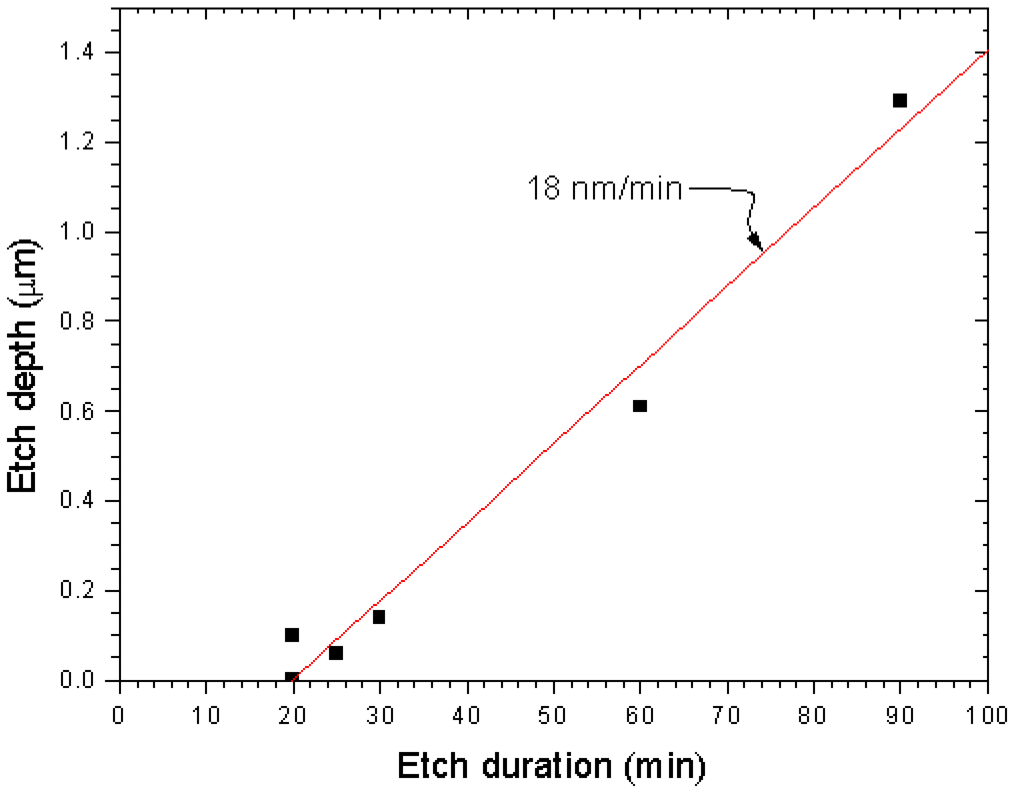

Figure 3.1.2: GaN reactive ion etching depth as a function of etching time in a 200W plasma with a flow rate of 10 sccm Cl_2 at 8mTorr

The 70° sidewall angle and 200 nm sidewall roughness observed here in reactive-ion-etched GaN can be seen in the scanning electron microscope (SEM) image in Figure 3.1.3. The 10-μm-wide GaN bars in the image are etched all of the way through to the sapphire substrate. The SiO_2 mask roughens during the etching process, and the roughness of the sidewalls is correlated with the roughness of the mask. The angled sidewalls begin to form where the GaN surface is partially shaded at the edges of the mask. The angled surface propagates because the ions striking it are reflected at a shallow angle, and the energy transfer in the reflection is insufficient to cause etching. Reactive ion etching is reportedly used by Nakamura for most of his laser facets, and the results that he reports are significantly better than what is reported here, in terms of both roughness and verticality. An SEM image of one of his etched facets is shown in Figure 3.1.4 for comparison.[90]

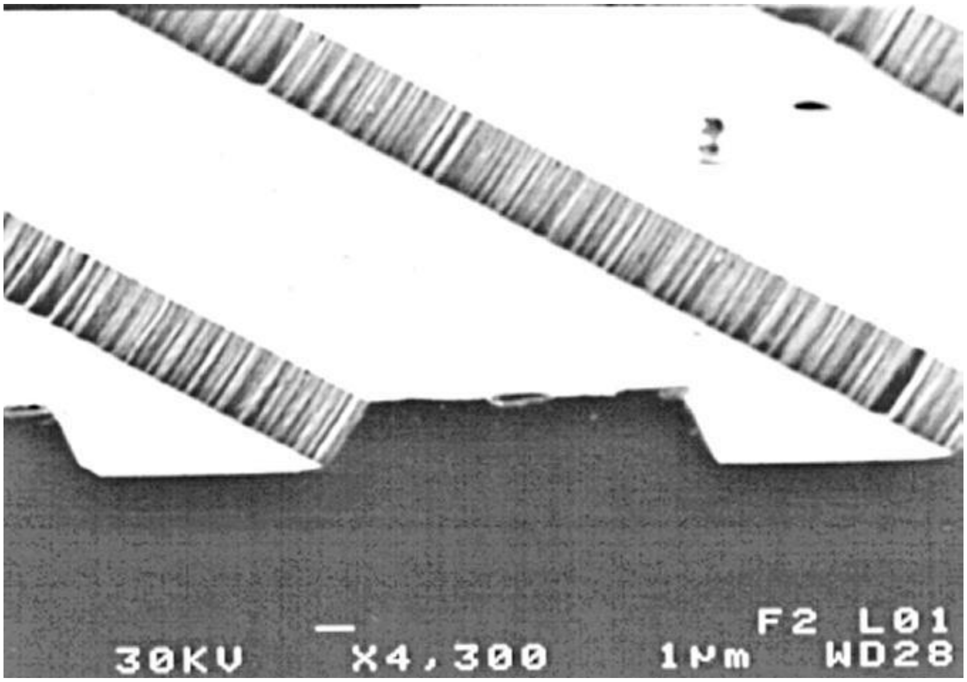

Figure 3.1.3: Reactive-ion-etched facets, with a 70° sidewall angle and a 200 nm sidewall roughness

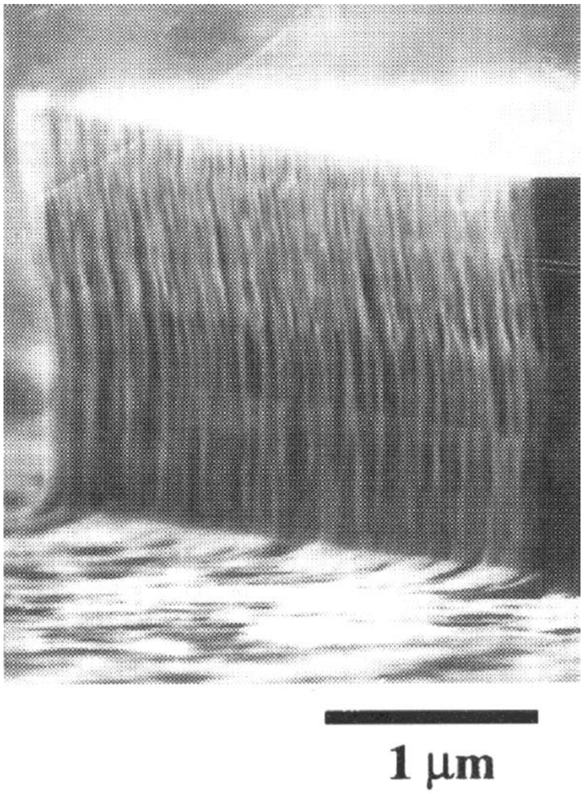

Figure 3.1.4: Scanning electron microscope (SEM) image of a dry etched facet in a GaInAlN device. (Reprinted with permission from Ref. 90)

3.2. Discussion of other dry etching techniques

In order to achieve better anisotropy (*i.e.* more vertical sidewalls) and higher etch rates in GaN, other dry etching techniques have been developed. Three of these techniques, magnetron-enhanced reactive ion etching, electron cyclotron resonance (ECR), and inductively coupled plasma, are enhanced versions of RIE, where magnetic fields are used to increase the plasma density. With magnetron-enhanced RIE, etch rates as high as 350 nm/min have been reported,[91] nearly six times the highest RIE etch rate. Inductively coupled plasma etching has proven even more effective, producing vertical sidewalls with etch rates as high as 980 nm/min in a Cl_2/Ar plasma.[92] The highest dry etch rates reported for GaN, 1300 nm/min, have been for ECR in an ICl/Ar plasma.[93] High-density plasma etching was the first etching technique to be used for producing GaN-based laser diodes, and is still the most common method.[31,94]

A fourth dry etching technique, chemically assisted ion beam etching (CAIBE), bombards the sample with an argon ion beam in the presence of a reactive gas. With chlorine gas, etch rates as high as 330 nm/min have been reported, with a sidewall angle of 94-96°.[95] Use of HCl decreases the etch rate, to a maximum of 190 nm/min, but creates vertical sidewalls.[96] Recently, CAIBE has also been used to fabricate laser structures with sidewall roughnesses of 4 – 6 nm.[35]

3.3. Discussion of advantages and disadvantages of dry etching

Dry etching is currently the method of choice for fabricating laser structures. This is due to the anisotropy and high etch rates achievable with enhanced etching systems. With a state-of-the-art ECR system, laser cavities with vertical sidewalls can be etched in approximately two minutes. Lasers fabricated with this method have been demonstrated to operate with outputs as high as 400 mW, and with threshold currents as low as 16 mA.[37]

Despite these successes, however, dry etching techniques are not the ideal method for etching of GaN. Reactive ion etching of GaN requires unusually high ion energies, which inflict surface damage and modify the surface stoichiometry.[97] High-density plasma techniques are less damaging than traditional RIE,[98] but the damage can still be significant. Defect generation by hydrogen incorporation has been observed to increase the sheet carrier concentration of GaN and decrease its effective Hall mobility in some etching chemistries.[99] This damage is reversible through subsequent annealing at 800°C, which is sufficient to remove the hydrogen from the sample and restore its electrical qualities.[99] Irreversible damage has also been reported in the upper layers of the etched GaN surface. ECR and magnetron-enhanced RIE have been shown to leave non-stoichiometric n^+-type surface layers to a depth of 10 nm,[91] which degrade the rectifying properties of subsequently deposited metal contacts.[100]

Another serious disadvantage of dry etching is the striation of the sidewalls, which can be seen in both Figure 3.1.3 and Figure 3.1.4. As was shown in Section 2.3, the reflectivity of laser facets depends strongly on roughness. Sidewall roughnesses from dry etching are typically on the order of 50 nm, but high-quality facets for GaN-based lasers will need to have a roughness of less than 4 nm, as previously shown.

4. Cleaving

4.1. Physical properties of GaN

In the GaInAsP materials system, mirror-like laser facets are formed easily by *cleaving* the epilayers and GaAs substrate along a mutual cleavage plane. Cleavage is the ability of certain crystals to break along definite crystallographic directions. The cleavage properties of a material are determined by the crystal structure and the strength of the chemical bonds. GaN can crystallize in one of two phases, the cubic zincblende structure and the hexagonal wurtzite structure. The most common phase, and the only one investigated in this dissertation, is the more stable wurtzite structure. The crystal structure and the three equivalent *a*- and *m*-planes ($\{11\bar{2}0\}$ and $\{10\bar{1}0\}$, respectively) of wurtzite GaN are shown in Figure 4.1.1.[c]

The surfaces formed by cleaving a wurtzite GaN crystal along the *a*- and *m*-planes are both nonpolar, i.e. there are equal numbers of gallium and nitrogen atoms on the surface. This allows charge neutrality to be obtained without surface reconstruction or changes in stoichiometry, and helps the crystal to cleave easily in these directions. Northrup and Neugebauer have calculated the surface energies and atomic structures of $\{10\bar{1}0\}$ and $\{11\bar{2}0\}$ surfaces within the local-density approximation.[101] This

---

[c] Four-coordinate Miller indices, *e.g.* $\{10\bar{1}0\}$, are commonly used when dealing with crystals which have hexagonal symmetry. The conventions used for 4-coordinate Miller indices are explained in Appendix A.

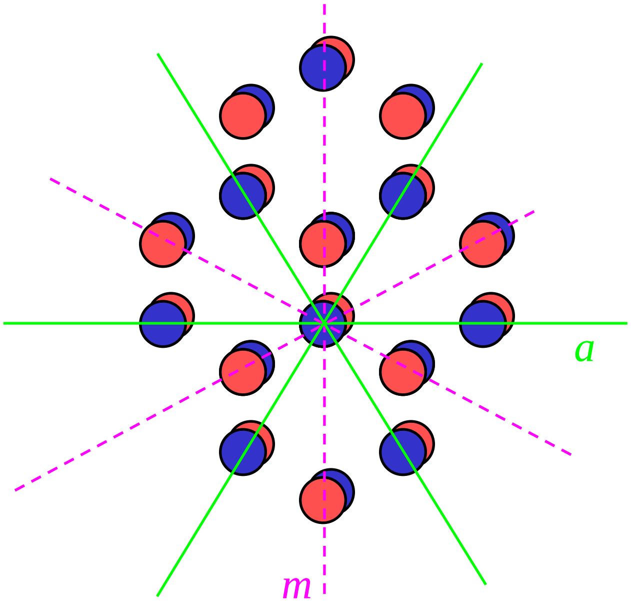

Figure 4.1.1: Crystal structure of Wurtzite GaN. The top two atomic layers are shown as they would appear when looking down along the growth axis. The plane of the paper is the (0001) *c*-plane. The $\{11\bar{2}0\}$ *a*- and $\{10\bar{1}0\}$ *m*-planes are perpendicular to the *c*-plane, cutting across it in the directions shown.

approximation shows that a small amount of reconstruction occurs for both surfaces, with Ga-N bond contraction by 4 – 6% and a ~7° buckling rehybridization in the surface layer. The surface energies of the $\{10\bar{1}0\}$ and $\{11\bar{2}0\}$ surfaces are 118 meV/Å^2 and 123meV/Å^2, respectively. This means that an energy of 118 meV/Å^2 is required to form a cleaved a-plane laser facet. For comparison, the energy per unit area required for forming cleaved laser facets in GaAs is 54 meV/Å^2.[101] Thus, GaN is more difficult to cleave than GaAs, but still cleaves readily along both the *a*- and *m*-planes, as has been observed by several groups.[57,102–105]

4.2. Cleavage of GaN grown on *c*-plane sapphire substrates

Cleaving GaN is more complicated than cleaving GaAs, because its cleavage planes do not align well with the cleavage planes of the *c*-plane sapphire substrates on which it is usually grown. The most efficient cleaving method for GaN grown on sapphire substrates involves considerable sample preparation. The substrates are prepared for cleaving by thinning to 200 μm, and then polishing and lightly scratching with a diamond scribe. After being mounted with wax to a thin piece of flexible metal, the samples are cleaved along the scribe marks by bending the metal, as shown in Figure 4.2.1. The epitaxial GaN layers are placed down against the metal sheet, so that the scribing occurs on the substrate and not on the epilayers. When this cleaving method is used on *c*-plane sapphire substrates with GaN epilayers, the resulting pieces display large areas where the sapphire and epitaxial layers have cleaved together cleanly.

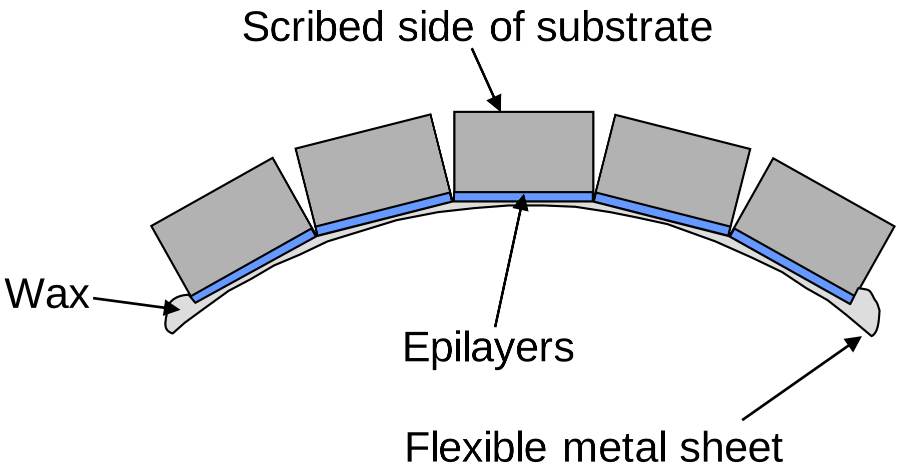

Figure 4.2.1: Method for cleaving GaN epilayers on a sapphire substrate.

When *c*-plane sapphire is used as a substrate, the crystal orientation of epitaxial GaN is rotated 30° with respect to the sapphire.[39] The reason for this is illustrated in Figure 4.2.2, which is taken from Ref. 39. The lattice mismatch between the unit cells of the *c*-plane sapphire and the *c*-plane GaN epilayers is over 30%. A hexagonal cell formed by aluminum atoms within the sapphire unit cell, however, has a mismatch with the GaN of only 15%. This cell of aluminum atoms is oriented 30° away from the sapphire unit cell, and the GaN epilayers align themselves with the aluminum atoms. Thus, the orientation of the GaN epilayers on the sapphire substrate is such that the GaN *a*-plane is parallel to the sapphire *m*-plane, and vice-versa.

Figure 4.2.3(a) is an atomic force microscope image of a cleaved GaN *a*-plane, showing striations with an RMS facet roughness of 16 nm. According to the theory developed in Section 2.3, this roughness corresponds to an 80% decrease in reflected intensity. Despite this loss of intensity, laser cavities have been reported on *c*-plane sapphire, cleaved along the GaN *a*-plane.[57] Figure 4.2.3(b) shows an SEM image of an *m*-plane GaN cleaved facet. The surface is very smooth, except for 90 nm steps that occur at intervals of approximately 2.2 μm. These steps have also been observed by other groups and have been attributed to a 2.4° rotation of the GaN *m*-plane with respect to the sapphire *a*-plane.[106] This slight misorientation with respect to the sapphire substrate has also been verified by using crystallographic etching, which will be described in Chapter 6. The 90 nm steps tilted at a 2.4° angle cause a decrease in reflectivity by more than 80%.[84] The steps on the cleaved GaN *m*-plane thus disqualify it from use in fabricating laser facets, unless the sapphire substrate could be cleaved at an angle 2.4° off of its *a*-plane.

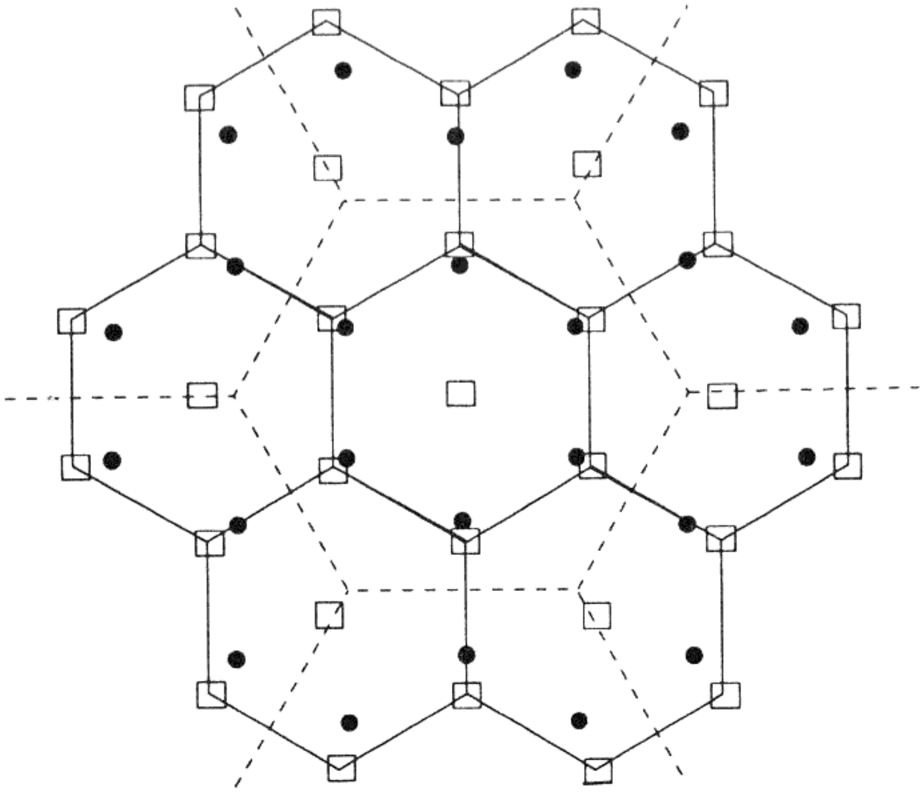

Figure 4.2.2: Projection of bulk *c*-plane sapphire and GaN cation positions for the observed epitaxial growth orientation. The dots mark aluminum atom positions and the dashed lines show the sapphire *c*-plane unit cells. The open squares mark gallium atom positions and the solid lines show the GaN *c*-plane unit cells. (Reprinted with permission from Ref. 39)

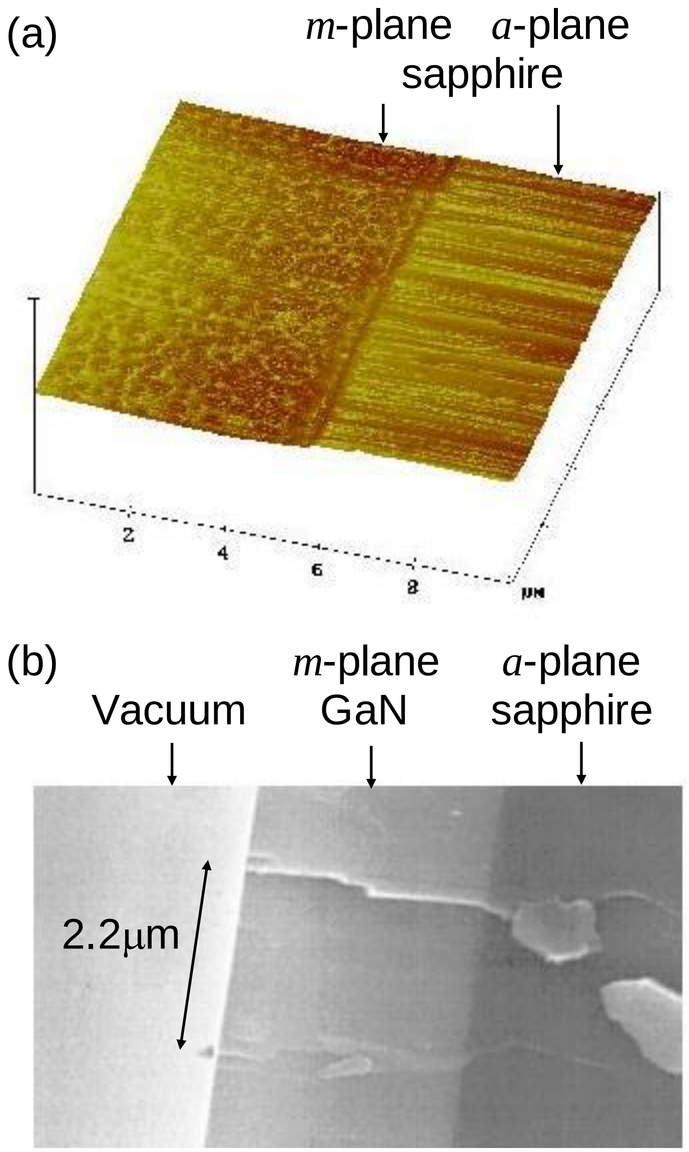

Figure 4.2.3: Images of cleaved GaN on *c*-plane sapphire. (a) Atomic force microscope image of cleaved *a*-plane GaN, showing striations with an RMS roughness of 16 nm. All units are in µm. (b) SEM micrograph of cleaved *m*-plane GaN, showing 90 nm steps occurring at ~2.2 µm intervals.

Sapphire does not cleave readily, and there has been some disagreement as to whether it cleaves at all. Some reports indicate that sapphire has no cleavage planes, but *parts* along both the (0001) and $\{11\bar{2}0\}$ planes.[107] Parting is the splitting of a crystal along a plane that does not normally cleave, and can be caused by stress, defects, or other perturbations of the crystal structure. Other reports indicate parting only along the (0001) plane when a layer of defects is present, and no cleavage in any direction.[108] After substrate thinning, Stocker *et al.* have observed cleavage along both the *a*- and the *m*-planes.[57]

Typical results of cleaving sapphire are shown in Figure 4.2.4. Figure 4.2.4(a) shows an edge cleaved exactly along the *a*-plane, while Figure 4.2.4(b) shows a jagged edge of the same piece of sapphire, this time broken 2° off of the *a*-plane. This figure shows that sapphire does, in fact, have cleavage planes. It cleaves cleanly along the *m*-plane as well as the *a*-plane, but cleaving along other crystal planes perpendicular to the *c*-plane was not successful.

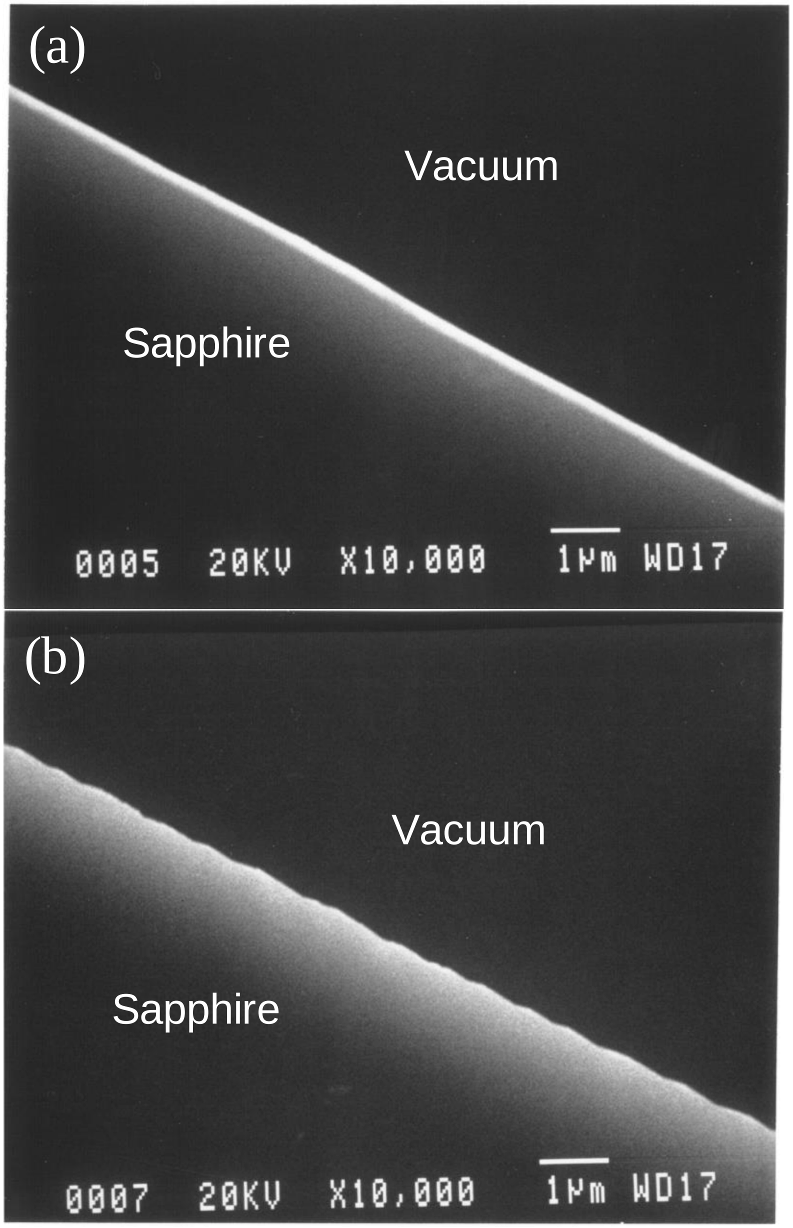

Figure 4.2.4: SEM images of cleaved sapphire. (a) Edge cleaved along the *a*-plane. (b) Edge broken 2° off of the *a*-plane

4.3. Cleavage of GaN grown on other substrates

The difficulties encountered when using *c*-plane sapphire as a substrate have provided an incentive to look to other possible substrates for GaN. These alternative substrates include *a*-plane sapphire, silicon carbide (SiC), spinel ($MgAl_2O_4$), and very thick pseudo-bulk GaN.

When GaN is grown on *a*-plane sapphire, the *m*-plane $\{10\bar{1}0\}$ of the GaN aligns with the *r*-plane $\{1\bar{1}02\}$ of the sapphire. Just as with *c*-plane sapphire, however, there is a slight misalignment of the two cleavage planes, approximately 2.4°, resulting in steps in the GaN epilayers.[105] No measurement of the RMS roughness of these surfaces have been reported in the literature. One group has reported on laser cavities formed by cleavage on *a*-plane sapphire, with results comparable to those of structures grown on *c*-plane GaN.[79,105,109]

SiC is sapphire's most serious competitor for use as a substrate for GaN. Its cleavage planes align perfectly with those of GaN epilayers, leaving facets with a roughness of only 0.7 nm.[110] This allows for easy fabrication of laser cavities.[34] In addition to its superior cleavage properties, SiC has the added advantages of relatively high thermal conductivity and electrical conductivity, if properly doped.[54] A thermally conductive substrate helps to keep down the temperature of electrically pumped laser diodes, which may improve their lifetime. Use of an electrically conductive substrate allows back-side electrical contacts, which can cut the number of processing steps considerably, lowering the cost of the final device. The only major disadvantage of SiC for use as a substrate is its relatively high cost, but if demand for SiC wafers increases, boosting the production of wafers, the cost could come down to be roughly equal to the cost of sapphire.

The third substrate that has been used to grow GaN for laser structures is spinel

($MgAl_2O_4$). Spinel apparently shares a cleavage plane with the GaN epilayers, because cleaved-facet lasers were reported with an RMS facet roughness of less than 0.3 nm.[111] Another group, however, has had difficulty in obtaining smooth mirror facets by cleaving on spinel, and has resorted to physical polishing to achieve smooth facets.[60] The physical polishing resulted in facets with a roughness of only 5 nm, but it is an extremely labor-intensive process and is not likely to result in a commercially viable product.

Nakamura *et al.* have recently reported on cleaved facet lasers grown on pseudo-bulk GaN.[112] *C*-plane sapphire is initially used as a substrate for a thin layer of MOCVD-grown GaN. An SiO_2 mask is then deposited and the substrate is returned to the MOCVD chamber for epitaxial lateral overgrowth. When the ELOG surface has coalesced over the SiO_2 mask, the sample is moved to an HVPE chamber, where ~200 μm of GaN is grown. Next, the sapphire substrate is removed by polishing. This provides a pseudo-bulk GaN film on which the laser structure is grown. While characterization of the cleaved facets for lasers made in this way has not yet been reported on directly, the far-field pattern of the lasers are much cleaner that that of the dry-etched-facet lasers that Nakamura has reported on previously. This improvement is likely due to smoother facets. The only major disadvantage to using this method for production of GaN-based lasers is the cost incurred by the multi-stage process for making the pseudo-bulk substrates.

4.4. Discussion of advantages and disadvantages of cleaving

For most laser applications, it is desirable to get a clean far-field pattern. Cleaved-facet lasers are ideal for this sort of application, because once the light leaves the cavity there are no structures to obstruct the light beam. This is because a cleaved facet is always at the very edge of the wafer. On the other hand, if the laser light is to be used in an integrated optoelectronic device, it is often useful to have the laser sitting somewhere in the middle of a wafer; this cannot be done using cleaved facets. This difference between cleaved and etched facets is illustrated in Figure 4.4.1.

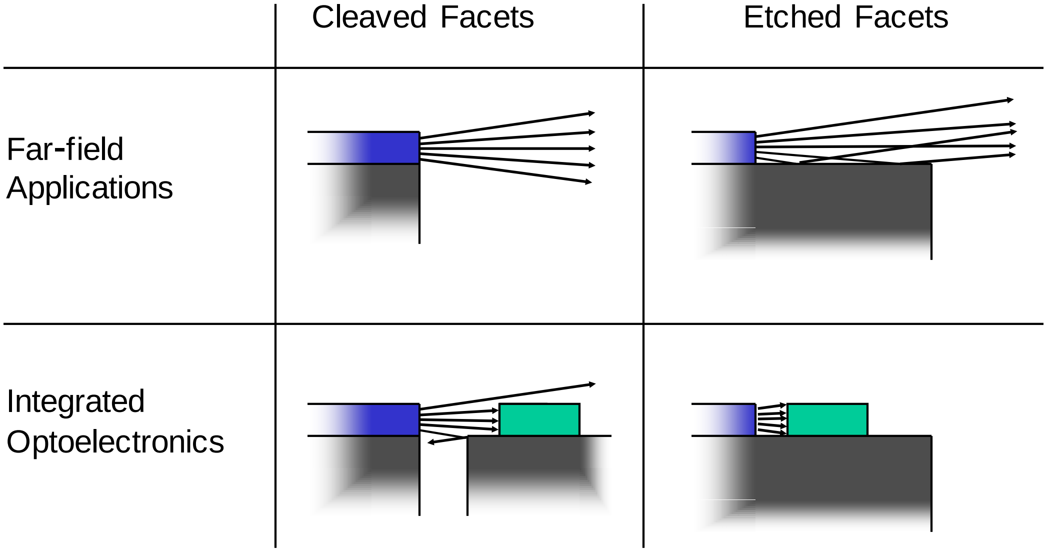

Figure 4.4.1: Comparison of cleaved-facet and etched-facet lasers for far-field and integrated optoelectronic device applications.

Cleaving can be an excellent method for producing laser cavities when a clean far-field pattern is wanted. It is very easy to produce parallel vertical walls using cleaving, because the crystal itself controls the direction of the break. This is in direct contrast to the dry etching techniques that are currently used to fabricate most laser structures, where achieving vertical sidewalls is often a difficult process. Another advantage of cleaving is that it produces relatively little surface damage. While there is some slight surface reconstruction, there is no damage induced by ion bombardment, such as a change in stoichiometry. The main barrier to using cleaving as a method for fabrication of GaN-based laser facets is lack of epilayer alignment with sapphire substrates. This difficulty is overcome by the use of SiC or pseudo-bulk GaN substrates, but the higher cost of SiC and the complexity of making pseudo-bulk GaN are currently limiting their use. Once the problem of finding an easily manufacturable, low-cost substrate whose cleavage planes are parallel with the epitaxial GaN is overcome, cleaving will probably become the method of choice for fabricating most GaN-based lasers. However, for integrated optoelectronic device applications, etched-facet lasers will likely prevail, so methods for fabricating etched facets must be explored further.

5. Photoenhanced Electro-Chemical (PEC) Etching

5.1. Experimental procedure and etching mechanism

Due to the chemical stability of GaN, wet chemical etching has not been observed at room temperature. A photoenhanced electro-chemical (PEC) etching technique, however, has shown promise for etching GaN and its alloys. A simple schematic of the PEC etching apparatus used in these studies is shown in Figure 5.1.1. The UV illumination, normally provided by a HeCd laser or a mercury lamp, generates electron-hole pairs near the surface of the GaN. Electrons are swept from the GaN to the cathode by the electrical circuit, leaving excess holes in the GaN. These holes can break bonds at the surface of the GaN, since a hole is actually just the lack of an electron in the valence band. These broken bonds allow the electrolyte to attack the GaN surface, etching it away.

Consistent with observations by Youtsey *et al.*[113] that a charge of approximately 3 e^- is required to remove one GaN entity, observations by Peng *et al.*[116] that the etched surfaces have a high oxygen content, and observations by Stocker *et al.*[114] of gas bubbles forming on the sample surface and the gold cathode during the etch process, the following reactions are likely responsible for the removal of GaN:

$$2\mathrm{GaN} + 6\mathrm{OH}^- \rightarrow \mathrm{Ga_2O}_{3(aq)} + \mathrm{N_2} + 6e^- + 3\mathrm{H_2O} \text{ (at the anode)}$$ **Equation 5.1.1**

$$6\mathrm{H}^+ + 6e^- \rightarrow 3\mathrm{H_2} \text{ (at the cathode)}$$ **Equation 5.1.2**

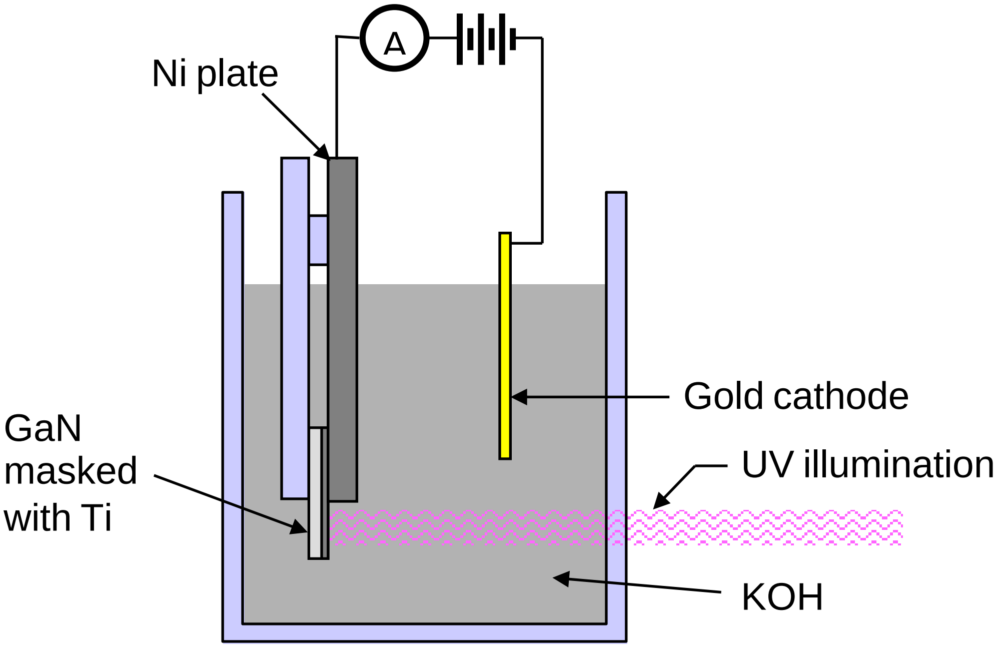

Figure 5.1.1: Schematic of PEC etching apparatus

5.2. Experimental results

GaN PEC etch rates of a few microns per minute have been achieved in KOH solutions,[115] and etching has also been observed in NaOH,[115] HCl,[115] H_3PO_4,[116] and a buffered solution of tartaric acid and ethylene glycol.[117] I have used HCl, NaOH, and KOH solutions for PEC etching of n-type GaN, with KOH producing the highest etch rates, up to approximately 2 μm/min.

60-nm-thick titanium or nickel masks are deposited by electron-beam evaporation and patterned by lift-off. If thinner masks are used, undercutting due to the transmission of light through the masks is observed. Annealing in a nitrogen ambient at 900°C for 30 seconds for titanium masks and 650°C for 2 minutes for nickel masks results in improved adhesion and better electrical contact between the GaN and the mask. A nickel bar or nickel-coated glass slide is used as an electrical contact to the masked GaN, and a gold wire is used as a cathode. Voltage and current are both monitored and a direct current power supply is used to apply a bias voltage. The UV light sources used here are a 200 W mercury lamp and a HeCd laser. All etches are done at room temperature.

Under optimized conditions, it is possible to produce near-vertical sidewalls, as shown in Figure 5.2.1, but they are very rough. The roughness of the sidewall as visible in Figure 5.2.1(a) is similar to the roughness of the titanium mask, and the top view in Figure 5.2.1(b) shows that this roughness is approximately 100 nm.

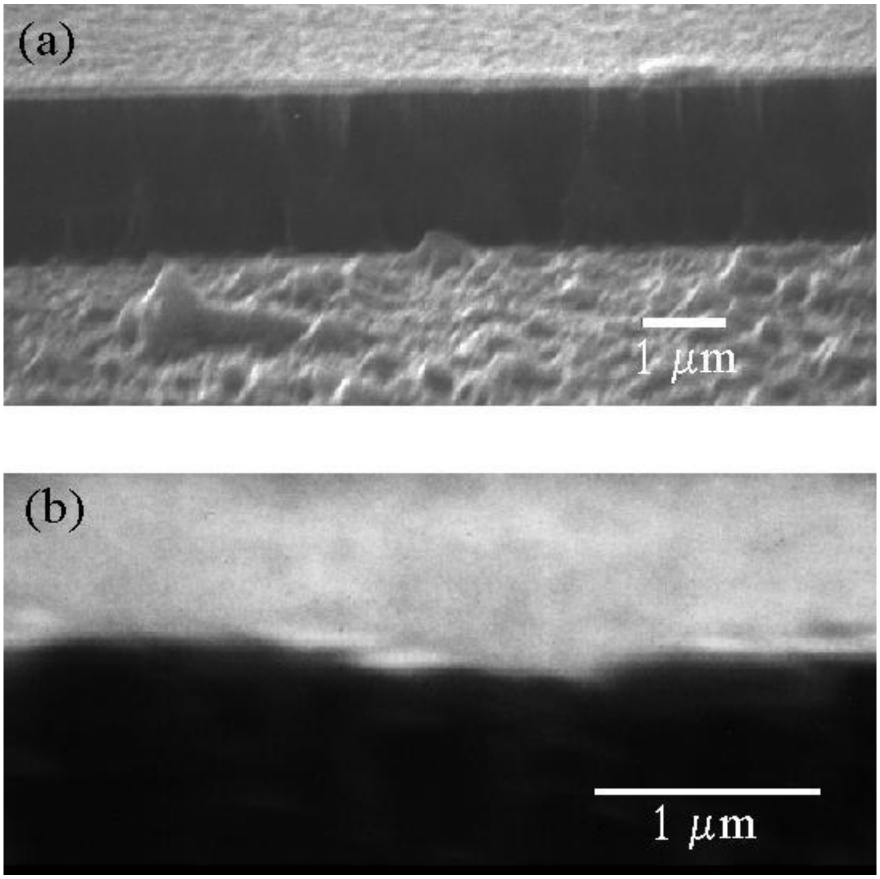

Figure 5.2.1: SEM images of PEC-etched GaN. (a) Side view of an etched sidewall. The 60-nm-thick titanium mask is visible on the top. The sidewall itself appears rough, and the bottom etched surface is extremely rough, covered with "stalagmites" of GaN. (b) Top view of the same sidewall. The roughness of the titanium mask is easily visible at this higher magnification.

For GaAs, PEC etch rates are strongly dependent upon doping, with an etching selectivity of (30:1) for n^+-type GaAs to non-intentionally doped GaAs and ≥ (15,000:1) for n^+-type GaAs to p^+-type GaAs.[118] This seems also to be true for GaN, although no selectivity measurements have yet been reported. Instead, dopant selectivity has been demonstrated by the use of a non-intentionally doped etch-stop layer under n-type GaN and also by undercutting of a buried n-type layer within a p-n GaN homostructure.[119] The reason for the influence of doping on etch rate is the surface band bending that occurs in semiconductors, and its effect on carriers. A schematic of surface band bending for GaN with the Fermi level pinned near the center of the bandgap is shown in Figure 5.2.2. The band bending results in a space charge region, where potential wells for minority carriers form at the surface. For n-type GaN, holes are trapped at the surface, where they can participate in the etching process. For p-type GaN, on the other hand, holes are swept into the bulk, and etching can not occur.

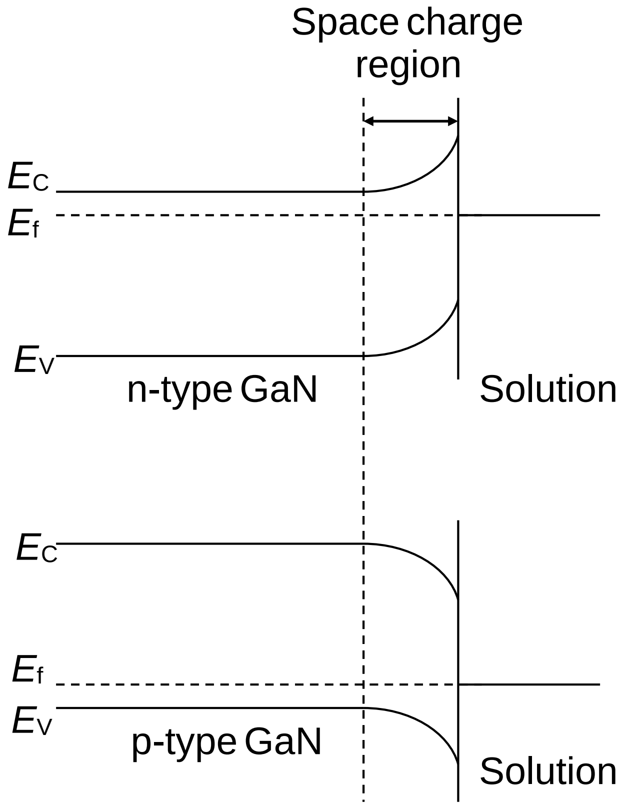

Figure 5.2.2: Surface energy band diagram for n- and p-type GaN

5.3. Origins and control of the roughness of PEC-etched surfaces

Under most circumstances, the PEC-etched GaN surface is extremely rough, as it is in Figure 5.2.1(a). In addition to surface morphologies like those in Figure 5.2.1, columns, cones, and "whiskers," have also been observed, as shown in Figure 5.3.1(a), (b), and (c), respectively. The columns are observed in HVPE-grown GaN by etching under strong HeCd laser illumination in 1.8 M KOH, and the cones are observed in MOCVD-grown GaN under the same etching conditions. The whiskers are observed in MOCVD-grown GaN when etching with illumination from a Hg lamp in 0.1 M KOH under voltage-biased conditions.

The roughness observed after PEC etching is believed to be caused by dislocations in the GaN crystal. Youtsey *et al.* have recently used transmission electron microscopy to show a correlation between whiskers like those shown in Figure 5.3.1(c) and mixed and edge threading dislocations in the unetched material.[120] The mechanism of formation of these whiskers is most likely a depletion of holes at the dislocations, possibly due to non-radiative recombination centers, dangling bonds, or impurities gettered from the bulk.[120] While the dislocations themselves can not be altered by changing the etch parameters, their effects can be minimized.

Youtsey *et al.* have demonstrated a method for producing smooth etched surfaces with an RMS roughness of approximately 1.5 nm, starting with an unetched RMS roughness of 0.3 nm.[121] Their method centers upon using KOH concentrations of 0.05 M or less. They have also observed that roughness often persists near large masked features. The maximum etch rate that they have achieved for smooth surfaces is 50 nm/min.

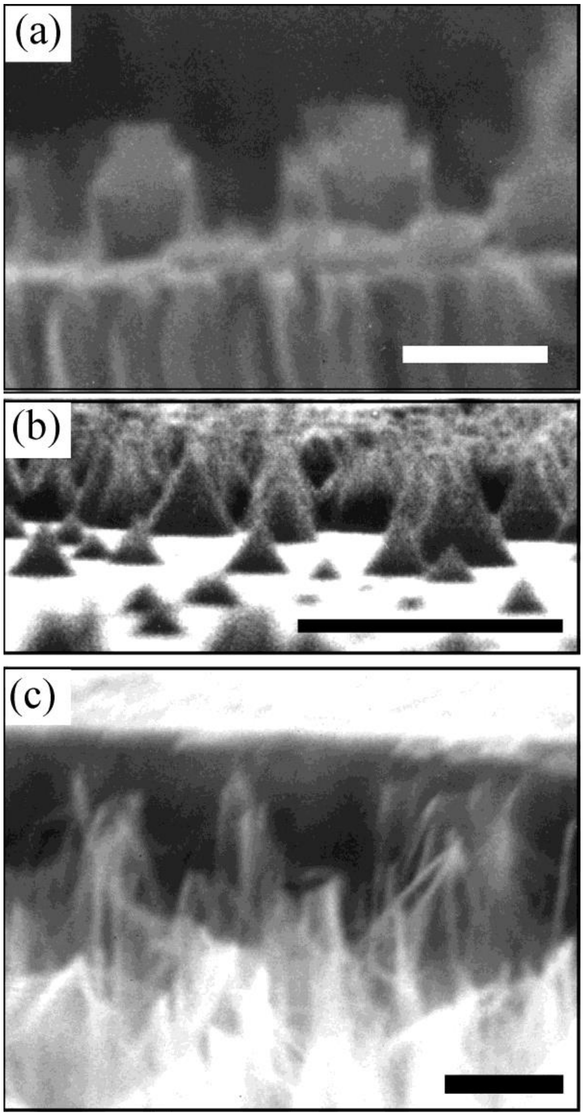

Figure 5.3.1: SEM images of various types of surface features which develop in GaN during PEC etching: (a) columns, (b) cones, and (c) whiskers. The bars in the lower right corners are 1μm long.

A new method has been developed here for producing relatively smooth PEC-etched surfaces with an RMS roughness of 20 nm while achieving an increased etch rate of 400 nm/min by introducing a bias voltage during the etching process. The initial roughness of the unetched surface is 17 nm, so almost no increase in RMS roughness is observed with this etching technique. Persistent roughness near large masked features is not observed under these conditions; the etched surface is equally smooth in all areas.

To show the effect of KOH concentration and bias voltage on etch rate and roughness, the concentration of the KOH solution used for PEC etching is varied between 0.01 M and 1.0 M, and the bias voltage is varied between 0.0 V and 2.5 V. Bias voltages higher than 2.5 V are found to strip the masks from the samples, even after annealing.

The roughness is whisker-like as in Figure 5.3.1(c) under all of these conditions. This morphology makes it difficult to measure RMS roughness using a profilometer, because the profilometer tip can easily break off the whiskers. Measurement of roughness by AFM is also inaccurate for all except the smoothest surfaces, because the thin whiskers do not generally stand straight up, and the density of whiskers is often such that the the AFM tip would never reach the lower surface. This causes the measured roughness to be considerably less than the actual roughness. SEM micrographs are used to determine the “relative roughness,” the ratio of the average peak height to the maximum etch depth as a function of KOH concentration and bias voltage. Figure 5.3.2 shows that the relative roughness decreases with decreasing KOH concentration and increasing bias voltage.

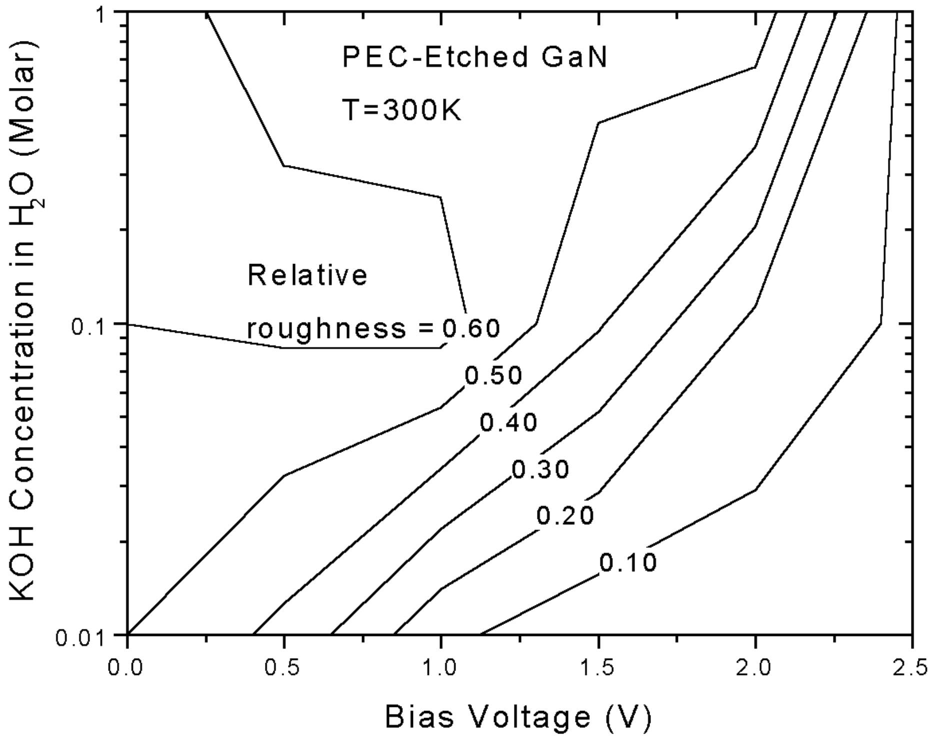

Figure 5.3.2: The relative roughness, *i.e.*, the ratio of the average peak height to the maximum etch depth, of the PEC-etched GaN surface as a function of bias voltage and KOH concentration at room temperature.

The decrease of roughness with decreasing concentration is probably due to depletion of OH^- ions in the aqueous solution. When the concentration of the KOH decreases, the concentration of OH^- ions also decreases. Thus, the ions are more likely to be depleted by reaction with the peaks of the etched surface before diffusing to the bottom. As a result, the etch rate will increase at the peaks and decrease in the valleys, smoothing out the surface.

The effect of the bias voltage on surface roughness likely stems from the electric field generated in the solution around the semiconductor. The electric field is strongest at the tops of the GaN peaks and weakest in the valleys, as illustrated qualitatively in

Figure 5.3.3. The effects of screening in the solution are not taken into consideration in this Matlab™ simulation, but the basic result of higher fields around the peaks would not change with the introduction of screening. Hydroxide ions are more strongly attracted to the peaks because of the stronger electric field, so the etch rate at the peaks increases. A similar mechanism has recently been proposed by H. P. Gillis[122] for the smoothing of rough surfaces which he has observed while using a dry etching technique for GaN called Low Energy Electron-Enhanced Etching. Gillis is currently creating a mathematical model to verify this hypothesis.[122]

The effect of bias voltage on the PEC etch rate of the GaN peaks is shown in Figure 5.3.4. The etch rate rises most significantly for a given concentration at the same time that the roughness is decreasing most strongly. For 1.0 M KOH solution, for example, the etch rate from Figure 5.3.4 and the roughness from Figure 5.3.2 stay fairly constant until the bias voltage reaches 2.5 V. The transition occurs earlier and more gradually as the KOH concentration decreases, occurring between 1.0 V and 2.5 V for 0.1 M solution and between 0.0 and 1.5 V for 0.01 M solution. This is most likely due to the OH^- ions being more easily depleted in the less concentrated solutions.

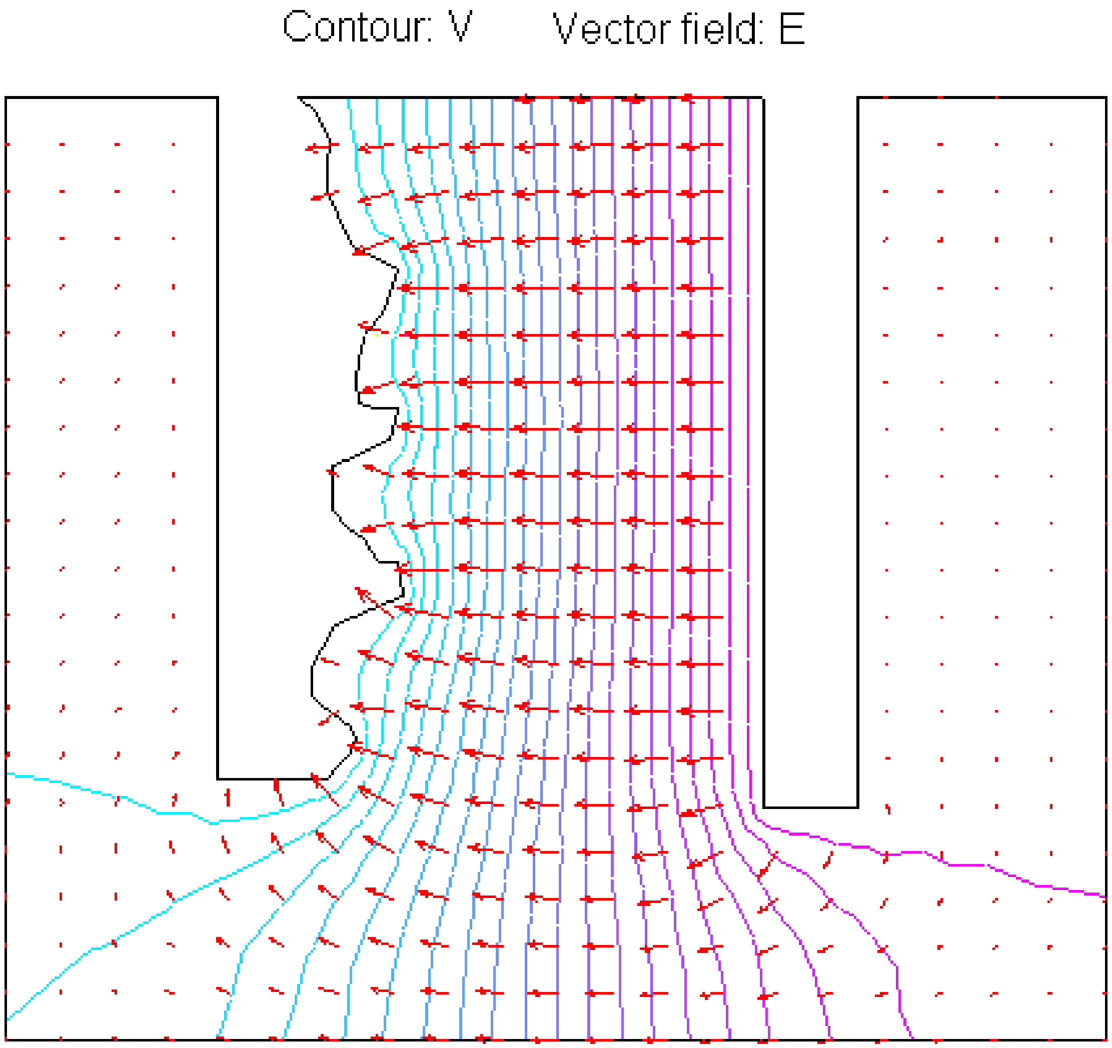

Figure 5.3.3: Matlab™ simulation of the electric field in a weak ionic solution between a smooth cathode, representing the gold wire, on the right and a rough anode, representing the GaN surface, on the left. The field is strongest at the peaks on the GaN anode, increasing the etch rate at the peaks and smoothing the surface.

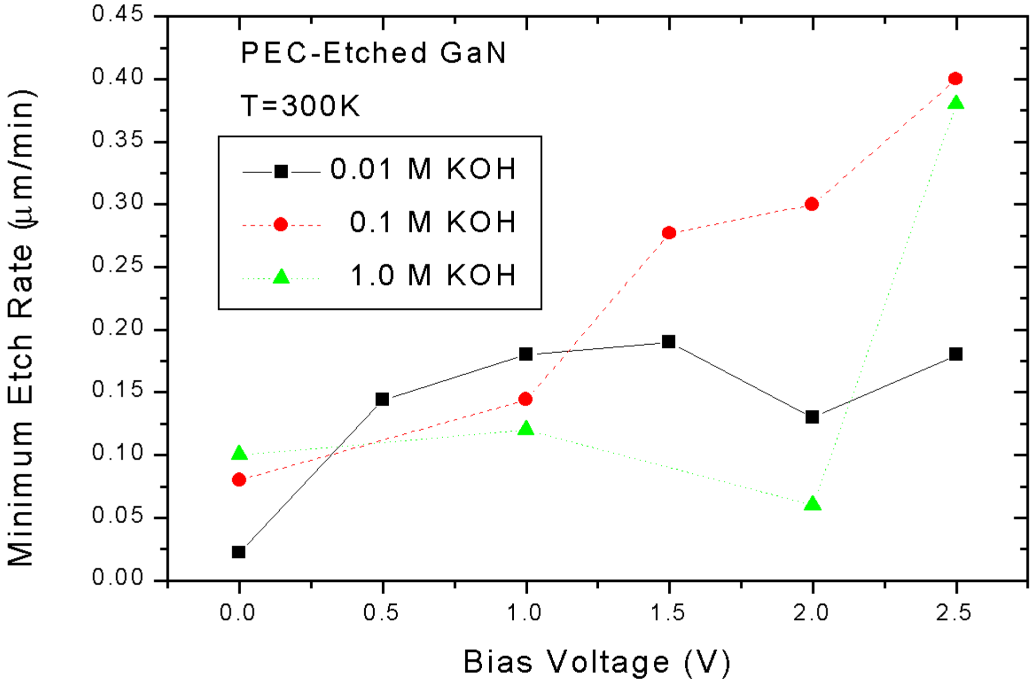

Figure 5.3.4: The minimum PEC etch rate, *i.e.* the etch rate of the GaN peaks, as a function of voltage for various KOH concentrations at room temperature.

5.4. Discussion of advantages and disadvantages of PEC etching

There are several advantages to using PEC etching, including high etch rates and low surface damage. This method will likely be very useful for making rectifying contacts to etched n-type GaN. As discussed in Section 3.3, dry etching causes ion-induced damage which creates an n^+-type surface layer which causes difficulty in making rectifying contacts.

The ability of the PEC technique to selectively etch material based upon doping concentration or band gap energy can also be useful for device fabrication. This selectivity, however, causes problems when fabricating some devices, including diode lasers. The upper layers of a diode laser structure are typically p-type, and to date nobody has reported on successful PEC etching of p-type GaN. Thus, while PEC etching may be useful for optically pumped lasers, until an ability to etch p-type GaN is developed it will not be useful for etching diode lasers.

A second difficulty when producing etched lasers is the sidewall roughness. While two groups have reported an ability to produce smooth etched bottom surfaces, no-one has developed a method for etching smooth, vertical sidewalls. However, a method for crystallographic etching of GaN has been developed which can be used to smooth the rough sidewalls produced during PEC etching.

6. Anisotropic Wet Chemical Etching

6.1. Etching mechanisms and theoretical models

A common processing technique in GaAs and Si technology is wet chemical etching.[123-128] Although chemical etching has existed for centuries and etching of silicon has existed for decades, the detailed mechanisms behind silicon etching are only now being uncovered.[129] While atoms may be removed anywhere on the surface, etching of semiconductors often occurs most easily along step edges, where atoms are generally more weakly bonded. A simplistic illustration of this is shown schematically in Figure 6.1.1, which shows a step edge on a Si (100). The surface atom which is most weakly bound is the one at the step edge. It has three dangling bonds which can react with the etchant and only one bond with the crystal structure; this combination causes it to be the most easily removed atom. This simplistic reasoning is not of great use when trying to determine the actual etching mechanisms taking place; the actual chemistry of the removal of atoms is not yet known, and the situation is further complicated by surface reconstructions and the effects of impurities and other defects in the crystal structure.

Surface reconstructions play a large role in etching of silicon, where the (111) surface adopts a 7×7 reconstruction which covers the surface with strong Si-Si bonds, slowing the etching of this plane. During etching, this plane forms large, flat terraces and etching occurs almost exclusively along step edges. The Si (100) surface adopts a 2×1 reconstruction with weak dimer bonds, increasing the etch rate of this plane. This 2×1 reconstruction allows rows of dimers to be removed easily, exposing the next lower atomic layer, which then dimerizes in the direction perpendicular to layer above it. The resulting surface does not have well-defined step edges, but is ragged-looking, with trenches and dimer chains running at right angles to one another. Surface reconstruction of GaN surfaces may also be expected to affect wet chemical etching similarly.

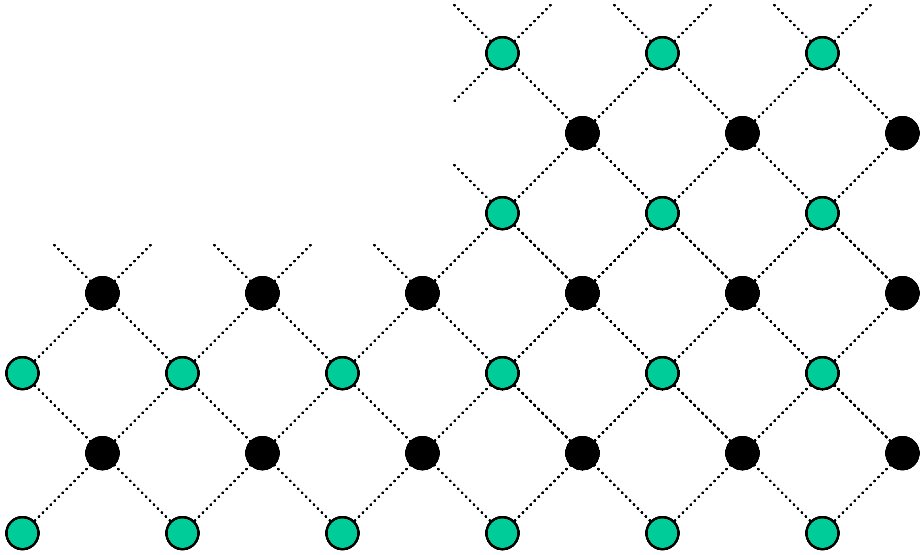

Figure 6.1.1: Schematic showing a step edge and the corresponding dangling bonds on a silicon (100) surface. The dashed lines represent bonds; the darker colored atoms are recessed into the page by ¼ of a lattice vector compared to the lighter colored atoms.

Several surface reconstructions have been studied on the GaN (0001) and $(000\bar{1})$ planes by scanning tunneling microscopy, electron diffraction, reflection high energy electron diffraction, Auger electron spectroscopy, and first-principles theory. These reconstructions include 1×1, 3×3, and 6×6 on the $(000\bar{1})$ surface,[130] and 2×2, 5×5, 6×4, and an as yet undetermined reconstruction labeled “1×1” (with quotation marks indicating that the symmetry is nearly, but not exactly, 1×1) on the (0001) surface.[131] Other reconstructions have also been observed on these surfaces, including 2×1, 2×3, 3×2, and 4×4, but the polarity of the surfaces, *i.e.* (0001) or $(000\bar{1})$, were not reported.[132,133] The $\{10\bar{1}0\}$ and $\{11\bar{2}0\}$ planes have also been studied theoretically using a local-density approximation, and the only reconstruction found on these surfaces is a Ga-N bond contraction and slight buckling rehybridization in the surface layer.[101]

Even without surface reconstructions, the atomic makeup of exposed planes can cause anisotropy in etching. This is true, for example, when using a bromine-methanol etchant on GaAs.[124] The {111} GaAs planes consist either of all gallium atoms or all arsenic atoms, and these two different planes have very different etch rates. This can be understood qualitatively by considering the top surface as being electrically neutral and comparing the bonding configurations of the two surfaces.[d] The gallium atoms have three bonding electrons and the arsenic atoms have five bonding electrons; all of the surface atoms, whether the surface is covered with gallium or arsenide atoms, is connected to the next plane by three bonds. Thus, a surface gallium atom has no free electrons to interact with the etchant, while an arsenide surface atom has two. As a result, a surface completely covered with arsenide etches faster than a surface that is covered partially with arsenide and partially with gallium, which in turn etches faster than a surface covered completely with gallium. While this sort of analysis provides qualitative insight into etching mechanisms, quantitative work has generally been avoided. Instead, phenomenological or heuristic approaches are usually taken to describe etching characteristics.

---

[d] This analysis is taken from R. Williams, *Modern GaAs Processing Methods*, Artech House, Boston, p. 98 (1990).

Much theoretical work has been done on the shapes and surface structures of crystals. In 1901, G. Wulff described a method for determining the equilibrium shape for a crystal by a geometrical construction.[134] This was done by drawing normals to the ends of radius vectors representing surface energies. The equilibrium crystal shape is then described by the envelope defined by the combination of normals. This construction is called a Wulff plot. This work was continued by C. Herring, who developed conditions for the appearance of facets and the thermodynamic stability of crystal faces.[135] Usually, however, the surface shape is determined by kinetic factors such as surface reaction rates and mass transfer of reactants and products.[136] This limits the usefulness of Wulff constructions, which yield equilibrium shapes.

D. W. Shaw has developed a method that uses experimentally determined etching rates, rather than equilibrium surface energies, in modified Wulff-type constructions to determine the morphology of etched surfaces.[136] When applied to GaAs, this phenomenological method has been shown to work exceptionally well, predicting even very complicated surface shapes, as shown in Figure 6.1.2. While it does not elucidate the etching mechanisms, it can be a practical method for determining the shape of an etched surface based upon past experience with etching under the same conditions. This method can be applied to GaN after sufficient information has been gathered about etch rate as a function of crystallographic orientation.

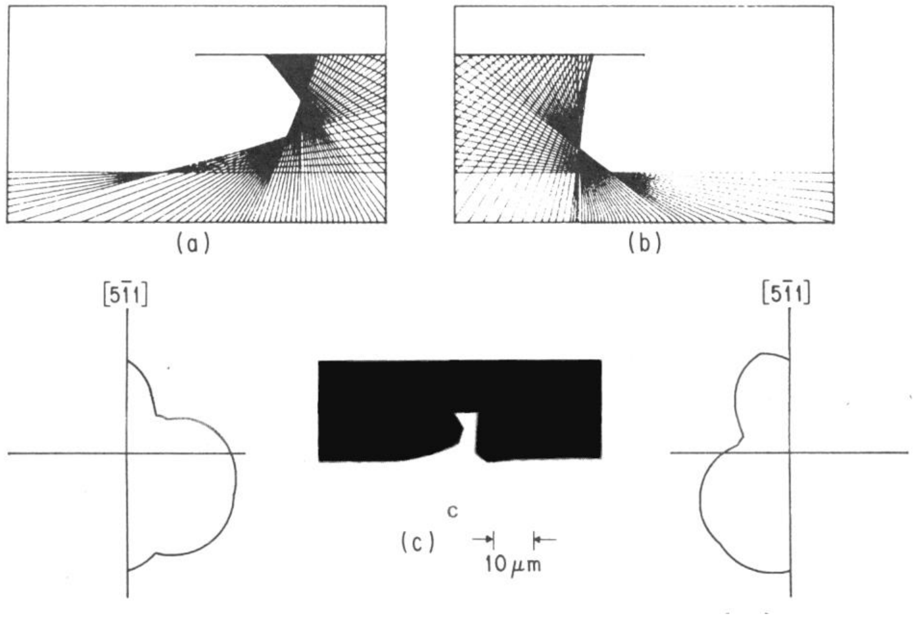

Figure 6.1.2: (a,b) Predicted cross-sectional profiles for opposing sides of a mesa etched in a {511} oriented GaAs slice using 1 H_2SO_4 : 8 H_2O_2 : 40 H_2O etchant. The diagrams upon which they are based are below each profile. (c) Micrograph of an actual cross section after etching. (D. W. Shaw, 1979)

6.2. Experimental results

GaN is so chemically stable that no chemical had been found that is able to etch it at room temperature until very recently.[137,138] J. L. Weyher *et al.*[138] have found that while the (0001) GaN surface does not etch at all in concentrated KOH and NaOH solutions at room temperature, the $(000\bar{1})$ surface is attacked and forms pyramidal structures with side walls that are most likely $\{10\bar{1}2\}$ planes. Once the surface is covered with these pyramidal structures, the etching stops. The reason for the difference in etching characteristics between (0001) GaN and $(000\bar{1})$ GaN is probably due to the difference in the surface atoms, with the gallium-covered (0001) surface etching much more slowly than the nitrogen-covered $(000\bar{1})$ surface, as described in the previous section. This etching is useful for determining the polarity of the crystal, and can be combined with mechanical polishing to provide smooth surfaces, but is not useful for etching for device fabrication. Stocker *et al.*[139] have recently developed wet etching techniques in GaN with a two-step process that allows crystallographic etching to be used for device processing.

The first of the two etching steps in the crystallographic etching process is used to establish the *etching depth*, and it can be performed by any of several common processing methods. As a first step several different processing methods have been used, including reactive ion etching, PEC etching, and cleaving. The second step is done by immersion in a chemical that is able to crystallographically etch GaN. This step can produce smooth crystallographic surfaces, and the specific etching planes can be chosen by varying the orientation of the first step, the chemical agents, and the temperature.

Because the *c*-plane is impervious to all of the chemicals investigated thus far, no etch mask is required for the crystallographic etching step—the *c*-plane itself acts as a mask. An etch mask may be necessary, however, if long etching times are used, to prevent the development of etch pits at defect sites. Very few common masking materials can withstand the hot, caustic etchants required for GaN. Materials such as Si_3N_4, SiO_2, photoresist, and TiO_2, to name a few, can not be used to mask GaN for wet etching. However, I have found two materials that do hold up to the etchants used for GaN: titanium masks after annealing at 900 °C for 30 seconds in a N_2 ambient, and nickel masks after annealing at 650 °C for 2 min in a N_2 ambient.

While they do not etch the *c*-plane of GaN in defect-free regions, molten KOH and hot phosphoric acid (H_3PO_4) have been shown to etch pits at defect sites in the *c*-plane of GaN.[140,141] S. K. Hong *et al.* have recently shown that etch pits form at nanopipe defects, but not at screw or threading dislocations.[142] Kozawa *et al.* reported that the facets of these pits correspond to the $\{30\bar{3}2\}$ face of GaN.[141] In this work, etch pits with facets that correspond to various GaN crystal faces have been observed after etching in H_3PO_4 above 160°C, in molten KOH above 180°C, in KOH dissolved in ethylene glycol above 135°C, and in NaOH dissolved in ethylene glycol at 180°C. An SEM image of these etch pits is shown in Figure 6.2.1. All of the hexagonal etch pits share a common base, the $\langle 11\bar{2}0 \rangle$ direction, but intersect the *c*-plane at a wide variety of angles. This is because the faces are actually produced by two or more competing etch planes, as can be seen in the high-resolution field-effect SEM image in Figure 6.2.2. The etchant temperatures are monitored using a thermocouple, and are accurate to within 5 °C. The etch pit density for the GaN samples is on the order of 10^6 cm^{-2} after etching in H_3PO_4 and 10^7 – 10^8 cm^{-2} in hydroxide-containing etchants.

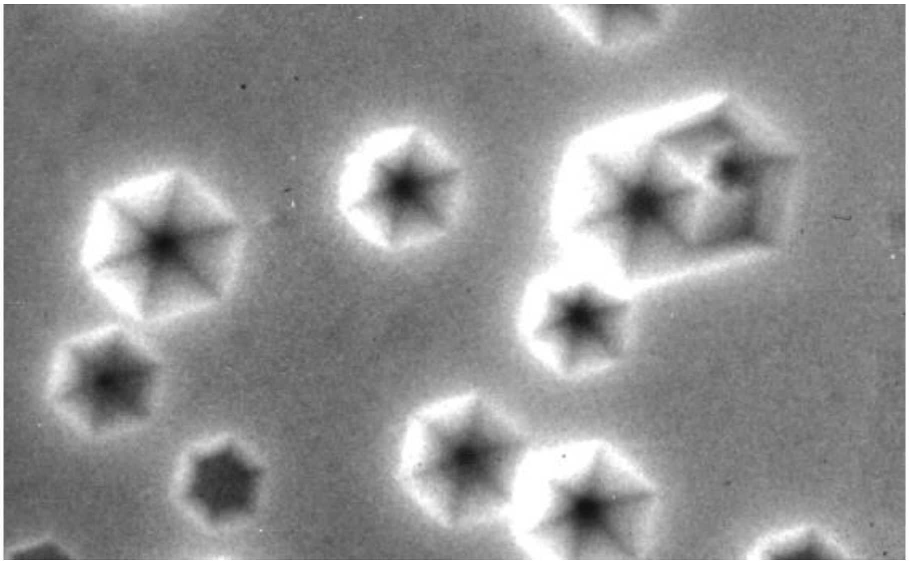

Figure 6.2.1: Top view of hexagonal etch pits formed in the *c*-plane of GaN by etching in molten KOH.

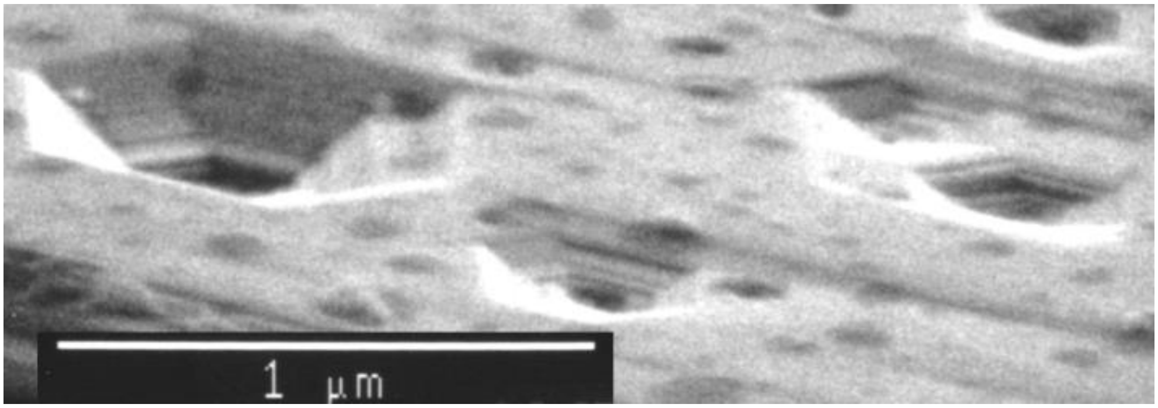

Figure 6.2.2: High-resolution field-effect SEM image of dislocation etch pits in the *c*-plane of GaN, produced by etching in 10% KOH by weight dissolved in ethylene glycol at 165°C.

By using another etching step before wet etching, it is possible to expose planes other than the *c*-plane, which can subsequently be wet etched. This is the basic concept behind the two-step etching process. The etch rates and crystal planes observed for all chemicals used in this work are summarized at the end of this chapter in Table 6.1. The etching planes listed in the table are those that appear during the etch. Because the *c*-plane {0001} is impervious to all of these chemicals except at the defect sites where etch pits occur, it is also an etch plane, with a negligibly small etch rate.

Figure 6.2.3 displays several illustrative examples of GaN epilayers that have been crystallographically etched after cleaving. Figure 6.2.3(a) and Figure 6.2.3(b) show a sample etched in H_3PO_4 at 132°C. The $\{10\bar{1}3\}$ plane shown in Figure 6.2.3(a) appears along the side of the sample cleaved along the GaN *a*-plane. The $\{10\bar{1}\bar{2}\}$ plane shown in Figure 6.2.3(b) appears along the side of the sample cleaved along the GaN *m*-plane. The $\{10\bar{1}0\}$ plane shown in Figure 6.2.3(c) was produced by etching in 10% KOH by weight dissolved in ethylene glycol at 165°C. This plane has been examined using a field-effect SEM with a resolution of 5 nm at 2.5 kV, and the surface appears perfectly smooth. The $\{10\bar{1}\bar{1}\}$ plane shown in Figure 6.2.3(d) was produced by etching in molten KOH at 184°C.

The activation energies for etching in these various solutions is 0.9 eV, or 21 kcal/mol, as inferred from the Arrhenius plots in Figure 6.2.4 and Figure 6.2.5. It should be noted that this is equal to the calculated heat of formation of GaN, 0.90 eV.[101] The heat of formation is the energy required to add a gallium atom and a nitrogen atom to a crystal of gallium nitride. The heat of formation of GaN is much lower than that of GaAs (5.56 eV)[143], although GaN has stronger chemical bonds. This is because the heat of formation is calculated beginning with the most stable form of each element. For GaAs, the most stable forms of the constituent atoms are Ga and As. For GaN, the most stable forms are Ga and N_2. Before nitrogen can be incorporated into the GaN crystal, the N_2 molecules must be split into atomic N. This requires a great deal of energy, 4.88 eV per nitrogen atom.[144] If this energy is added to the heat of formation of GaN, then it can be seen that the amount of energy required to break the crystal bonds is higher for GaN than for GaAs.

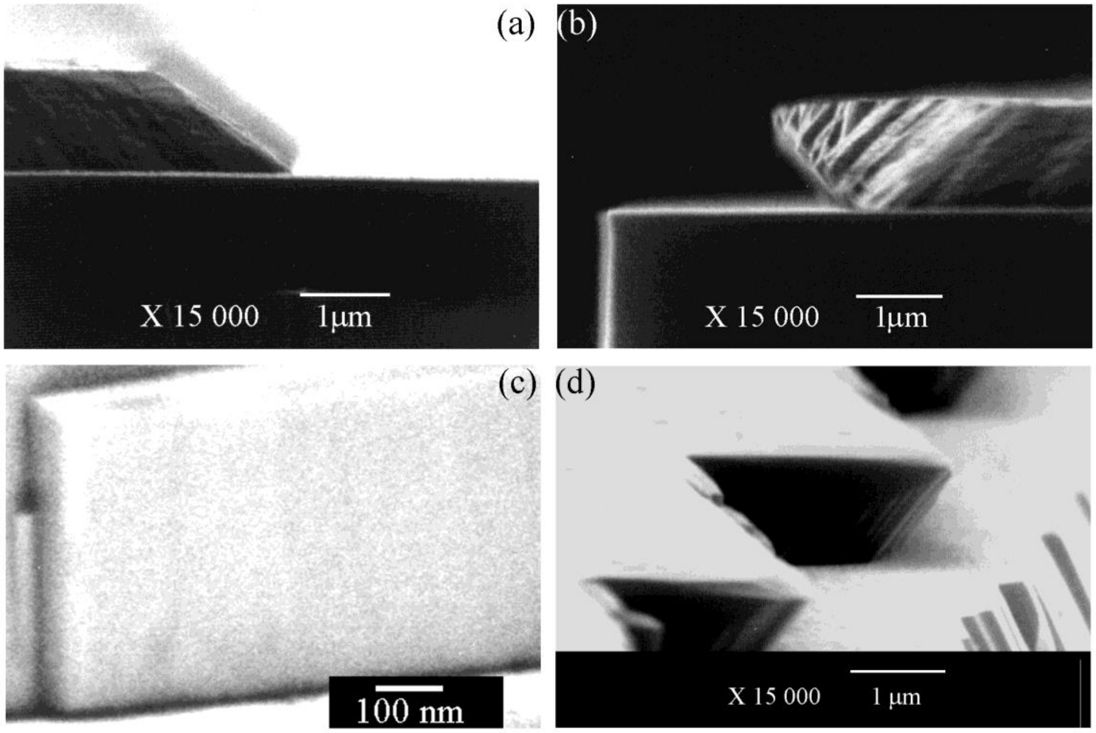

Figure 6.2.3: SEM images of crystallographic surfaces of GaN made by wet etching. (a) Overcut $\{10\bar{1}3\}$ plane etched by H_3PO_4. (b) Undercut $\{10\bar{1}\bar{2}\}$ plane etched by H_3PO_4. (c) Vertical $\{10\bar{1}0\}$ plane etched by KOH in ethylene glycol. (d) Undercut $\{10\bar{1}\bar{1}\}$ plane etched by molten KOH.

The activation energy indicates that the etch is not diffusion-rate limited, but reaction-rate limited, since typical activation energies for diffusion-limited etching are in the 1 – 6 kcal/mol range.[145] The activation energies observed here are much larger than this, which implies reaction-rate limited etching. The anisotropic nature of the etch supports the identification of reaction-rate limited etching, because diffusion-limited etching tends to be isotropic and polish the exposed surfaces.[146] Linear Arrhenius plots are unusual for compound semiconductors,[147] because they indicate that the etch rate is controlled by only one reaction, which would imply that either Ga-N dimers are removed during etching or else one atomic species is much more easily removed from the surface than the other.

The etch rates shown in Figure 6.2.4 – Figure 6.2.6 are measured perpendicular to the growth direction, i.e. in the "horizontal" *c*-plane. For "vertical" planes, such as the $\{10\bar{1}0\}$ plane, the actual etch rate of the plane is equal to the etch rate measured. For non-vertical planes, however, the etch rate of the plane is actually less than the measured etch rate. The etch rate perpendicular to the $\{10\bar{1}\bar{2}\}$ plane, for instance, is the etch rate shown in Figure 6.2.4 multiplied by cos(46°), because the $\{10\bar{1}\bar{2}\}$ plane intersects the vertical $\{10\bar{1}0\}$ plane at an angle of 46°.

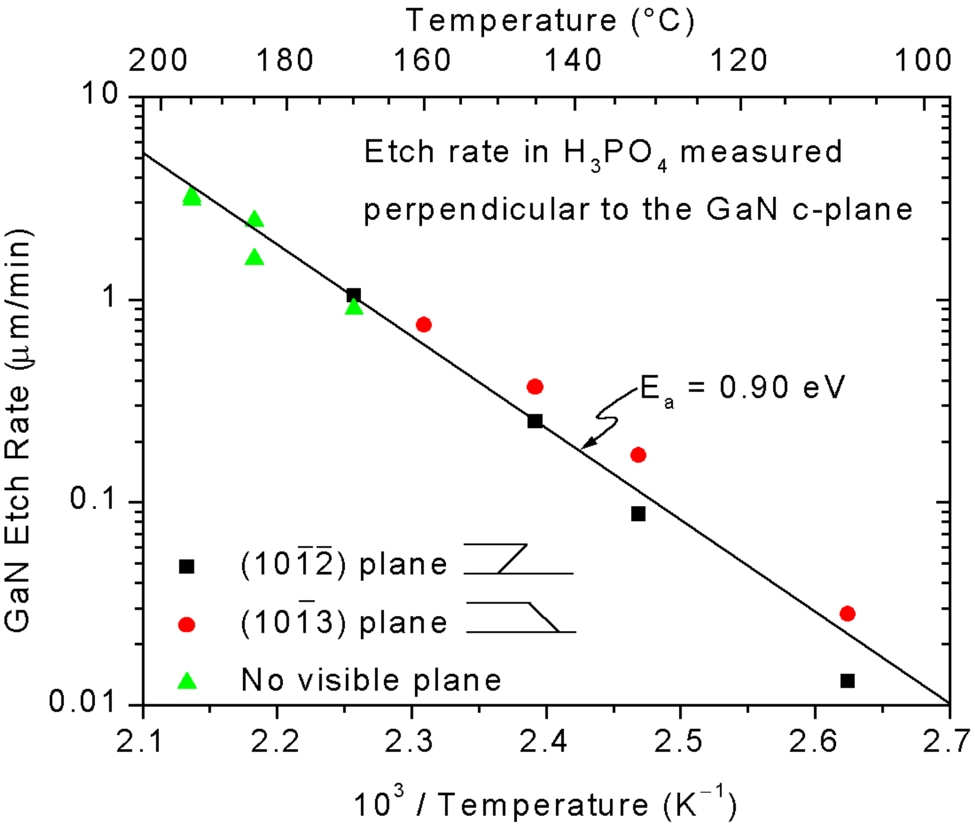

Figure 6.2.4: Arrhenius plot of etch rates for GaN in H_3PO_4.

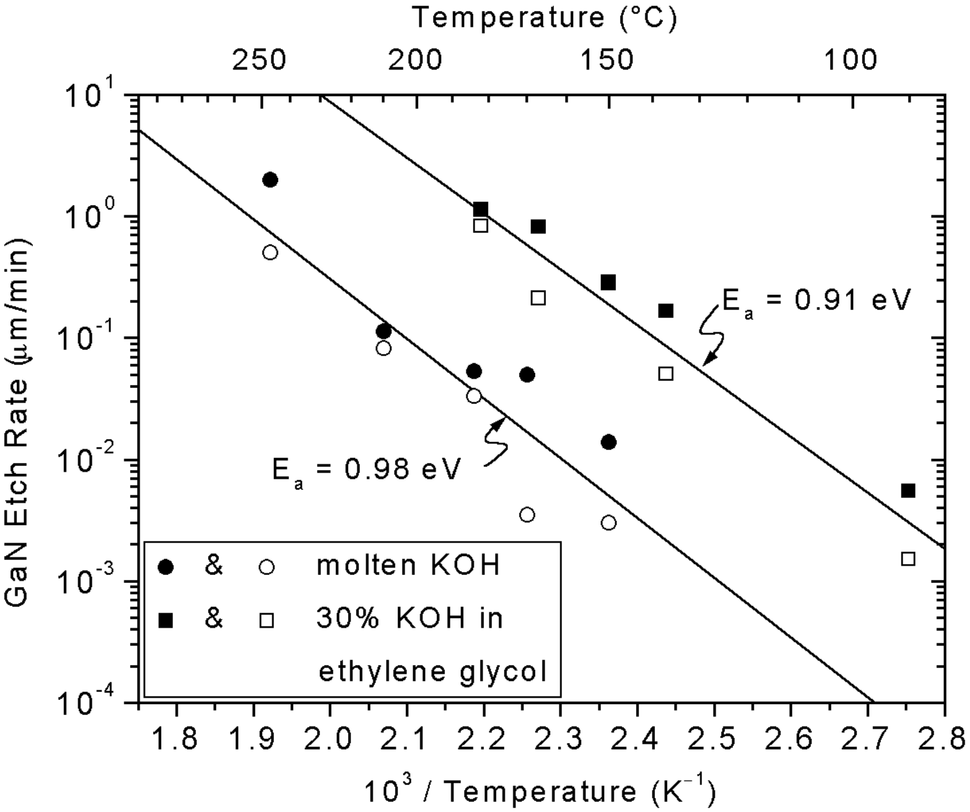

Figure 6.2.5: Arrhenius plot of GaN etch rates in KOH and 30% KOH dissolved in ethylene glycol. Solid and hollow symbols represent etch rates measured along cleaved edges parallel to the $\{11\bar{2}0\}$ *a*-plane and the $\{10\bar{1}0\}$ *m*-plane, respectively.

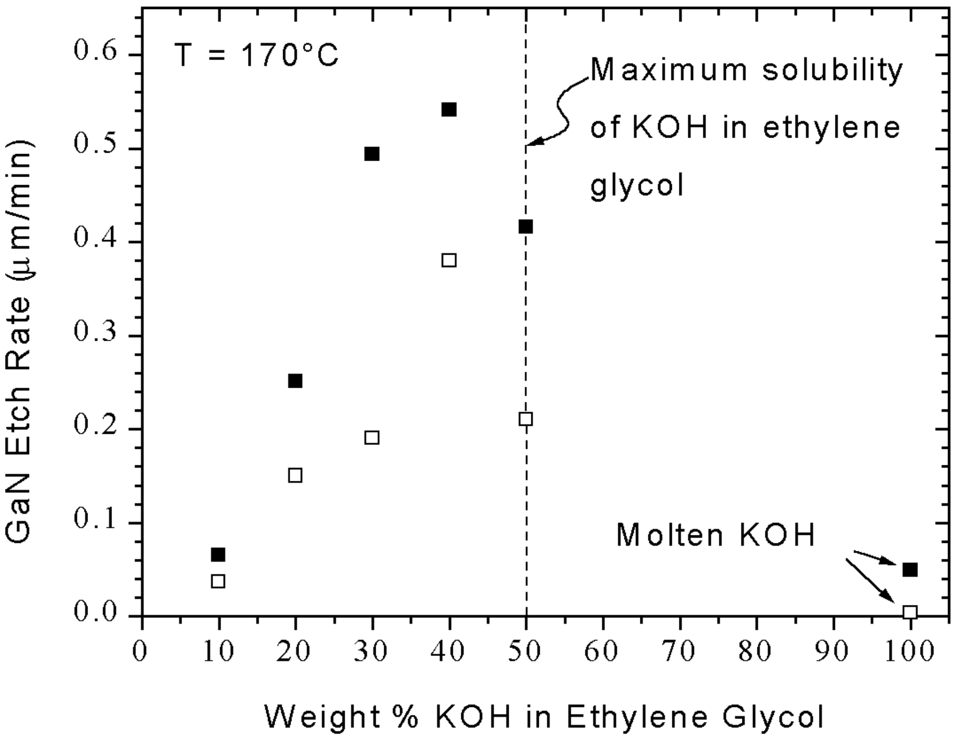

Figure 6.2.6: GaN etch rate as a function of KOH concentration in ethylene glycol at 170 °C. Solid and hollow symbols represent etch rates measured along cleaved edges parallel to the sapphire $\{10\bar{1}0\}$ *m*-plane and $\{11\bar{2}0\}$ *a*-plane, respectively.

It is interesting to note that the etch rate of 30% KOH dissolved in ethylene glycol is higher than the etch rate of molten KOH at the same temperature. In fact, the etch rate as a function of concentration peaks at a value of 40% KOH by weight in ethylene glycol, as can be seen in Figure 6.2.6. Initially it was believed that this could be due to high solubility of the etch products in ethylene glycol, but this can not be the case, since the etching rate is not limited by diffusion. The ethylene glycol must therefore play an active role in the chemical reactions taking place at the surface of the GaN. More work is needed in order to gain an understanding of the chemical reactions that are involved in this etching process.

If crystallographic wet etching is to be useful for fabricating GaN-based laser diodes, the doping dependence of etch rates and crystallographic orientation of the resulting planes must be established. To establish this relationship, crystallographic wet etching has been done on p-type GaN/non-intentionally doped GaN structures. SEM images of the two etch planes observed after these etches are shown in Figure 6.2.7 and Figure 6.2.8. Only the top portion of the epilayers is doped p-type with magnesium; the lower 1 μm is undoped. The seamless morphology of the surfaces displayed in Figure 6.2.8 indicates that the change in doping does not affect the etch plane or the etch rate. If the etching was affected by doping, a horizontal seam would appear between the doped and undoped regions.

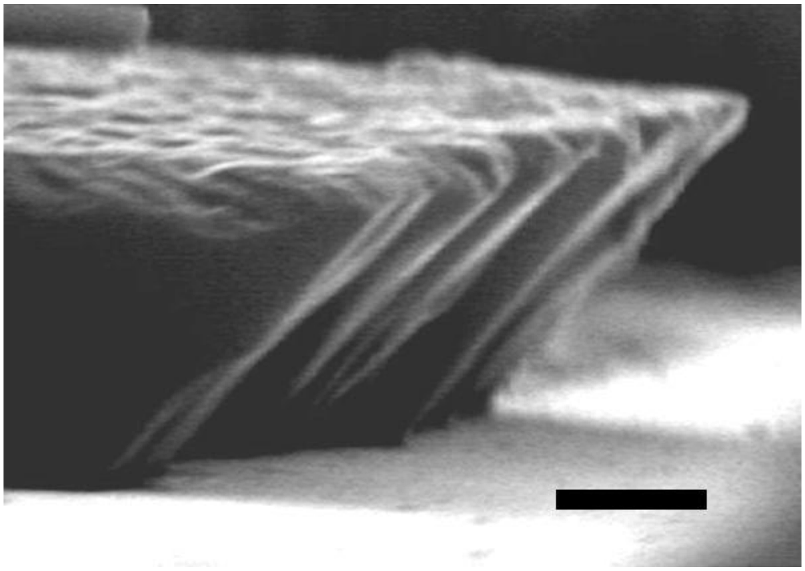

Figure 6.2.7: SEM image of a $\{10\bar{1}\bar{2}\}$ crystallographic p-type GaN surface made by wet etching in molten KOH at 243°C. The black bar in the lower right corner is 1 μm long.

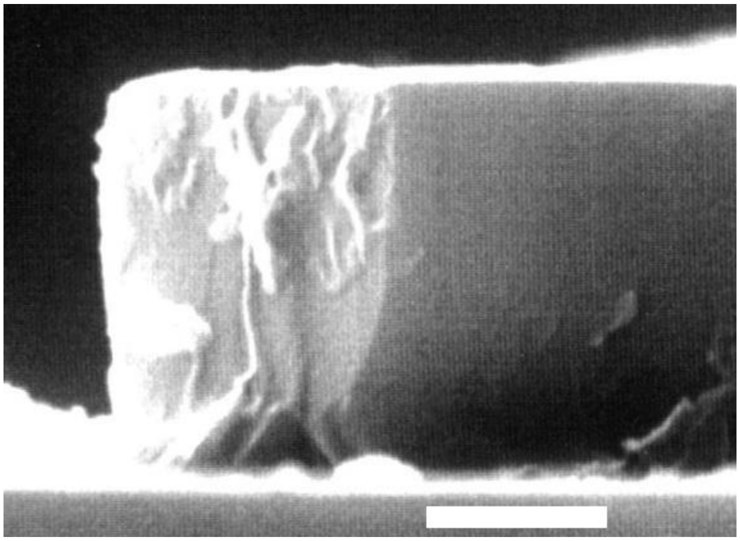

Figure 6.2.8: SEM image of a $\{10\bar{1}0\}$ crystallographic p-type GaN surface made by wet etching in molten KOH at 197°C. The white bar on the lower right side is 1 μm long.

The most commonly observed etching planes formed by H_3PO_4, tetraethylammonium hydroxide (TEAH), and KOH dissolved in ethylene glycol, and in molten KOH under some conditions, are $\{10\bar{1}\bar{2}\}$, as shown in Figure 6.2.7. The $\{10\bar{1}0\}$ planes shown in Figure 6.2.8 are also observed after etching in molten KOH. The quality of the crystallographically etched surfaces is generally lower in the p-type material than in the n-type material; in many cases, the only distinct crystal plane left after etching is the *c*-plane. The reason for this difference is unclear at the present time. It seems to be unrelated to crystal quality; the crystals are of similar quality, as indicated by x-ray rocking curve full-width-at-half-maxima of 800 – 900 arcsec and by etch pit densities on the order of 5×10^7 cm^{-2} after etching in molten KOH. The difference is also not related to the doping, since the p-type material etches seamlessly with the undoped material on which it is grown.

Etch rates and activation energies in molten KOH for p-type GaN and for n-type GaN are nearly the same, as can be seen from the Arrhenius plots shown in Figure 6.2.9. The activation energy observed in both samples is 21 kcal/mol, or 0.9 eV. As in Figure 6.2.6, two different etch rates are recorded for each sample at any given temperature in Figure 6.2.9 and Figure 6.2.10. The *faster* etch rate is measured at the side of the wafer cleaved along the sapphire *m*-plane, and the *slower* rate is measured at the side of the wafer cleaved along the sapphire *a*-plane. As inferred from the Arrhenius plots in Figure 6.2.10, the activation energy for the p-type GaN in 30% KOH in ethylene glycol is 21 kcal/mol, or 0.9 eV, and the activation energy in H_3PO_4 is 33 kcal/mol, or 1.3 eV. For

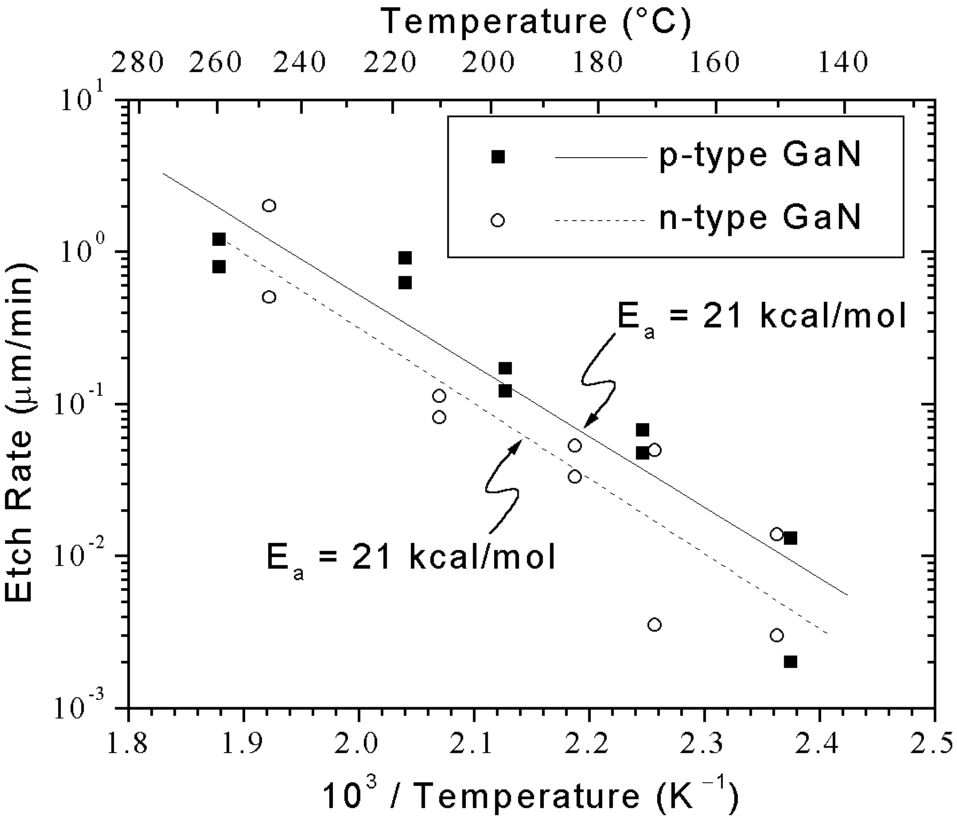

Figure 6.2.9: Arrhenius plots of n- and p-type GaN etch rates in molten KOH.

all of the etchants used, the activation energy is equal to or slightly higher than the calculated heat of formation of GaN, 0.90 eV.[101]

It is possible to begin to assemble modified Wulff-type etching diagrams by compiling all of this etch rate data. Points can be placed on the graph corresponding to the $[0001]$, $\{10\bar{1}0\}$, and $\{10\bar{1}\bar{1}\}$ directions for etching in KOH and KOH dissolved in ethylene glycol; $[0001]$, $\{10\bar{1}\bar{2}\}$, and $\{10\bar{1}3\}$ for etching in H_3PO_4; and $[0001]$ and $\{10\bar{1}\bar{1}\}$ for etching in TEAH and TMAH. This is enough information to begin to

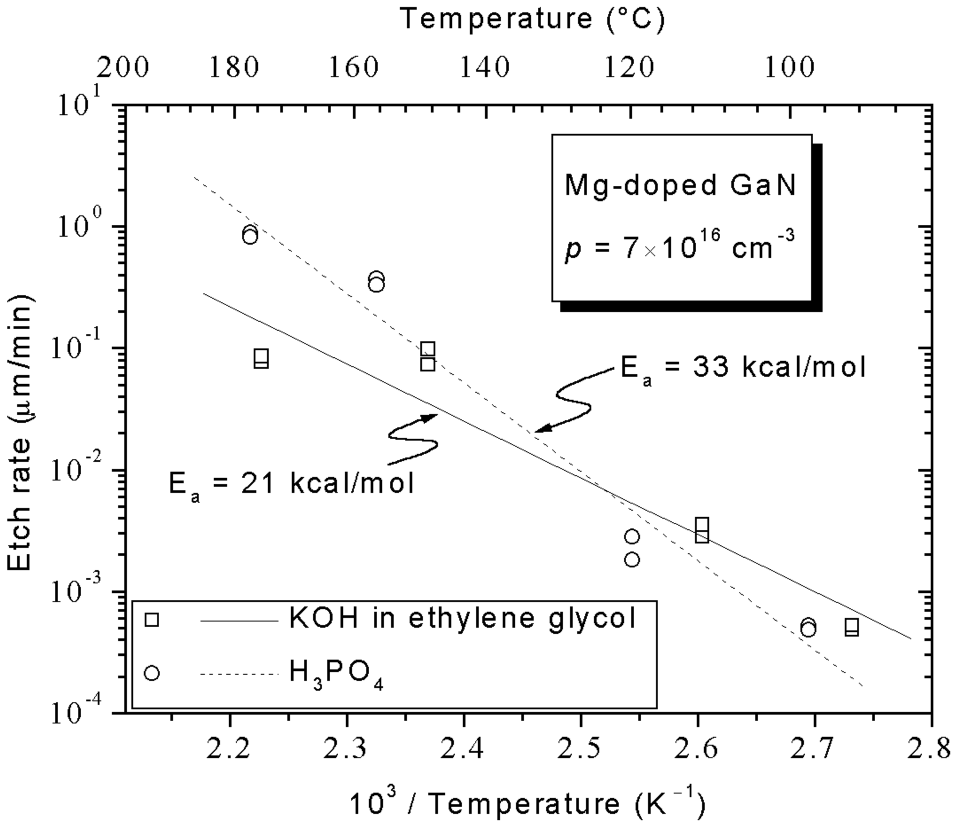

Figure 6.2.10: Arrhenius plot of p-type GaN etch rates in H_3PO_4 and in 30% KOH by weight dissolved in ethylene glycol.

get an idea about what a modified Wulff diagram would look like in the $[11\bar{2}0]$direction, which is orthogonal to all of the above directions. The etch rates in all of these directions will appear as cusps in the diagram, since curved surfaces have never been observed in this orientation after crystallographic etching. The curved lines that are included in Figure 6.2.11 show the general shape of the diagram but should not be taken as quantitatively accurate. In order to build up an accurate diagram it would be necessary to perform many more measurements of etch rates, each beginning on a sidewall with a slightly different angle.

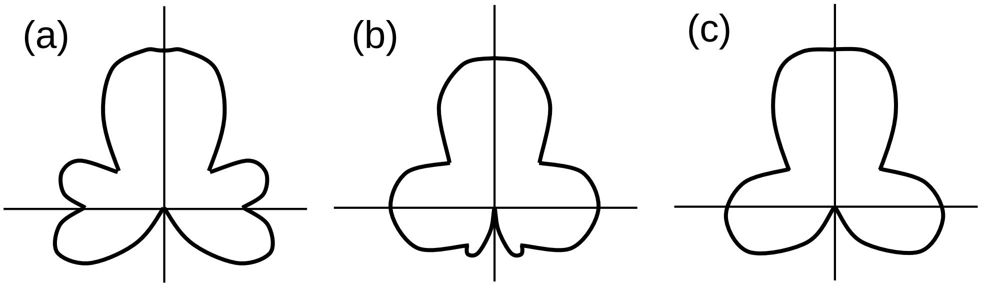

Figure 6.2.11: Modified Wulff diagrams of etch rates normal to the GaN $[11\bar{2}0]$ direction for etching in (a) molten KOH or KOH dissolved in ethylene glycol, (b) H_3PO_4, and (c) TEAH or TMAH.

The diagrams above show etch rates that are very low in the $[000\bar{1}]$ "downward" direction, higher in horizontal or off-angle directions, and very high in the $[0001]$ "upward" direction. The likely cause of this anisotropy is the same mechanism which causes anisotropic etching of GaAs in bromine-methanol, the atomic species in the first atomic layer. The GaN (0001) surface is composed entirely of gallium atoms, which have no electrons available for reaction with the etchants if the surface is assumed to be electrically neutral. For this reason, the etch rate of this surface, in the $[000\bar{1}]$ direction, is very low. The fastest etching surface is the nitrogen-covered [0001] surface, which is not accessible on our MOCVD-grown materials, but which Seelmann-Eggebert *et al.*[138,148] observed as the only etching plane of bulk GaN in hydroxide solutions at low temperatures. The other observed crystallographic etching planes correspond to planes that are covered partially with nitrogen and partially with gallium, and these planes have etch rates which fall between those of gallium-covered and nitrogen-covered surfaces. This analysis illuminates the linear Arrhenius plots observed for wet chemical etching of GaN: the reaction which limits the etch rate is the removal of gallium atoms from the surface.

Table 6.1: Wet chemical etch rates and observed etching planes for various chemicals.

Chemical	**Temperature (°C)**	**Etch Rate (µm/min)**	**Etching Planes Observed**
Acetic Acid (CH_3COOH)	30	< 0.001	None
Hydrochloric Acid (HCl)	50	< 0.001	None
Nitric Acid (HNO_3)	81	< 0.001	None
Phosphoric Acid (H_3PO_4)	108 – 195	0.013 – 3.2	$\{10\overline{12}\},\{10\overline{1}3\}$
Sulfuric Acid (H_2SO_4)	93	< 0.001	None
Potassium Hydroxide (KOH), molten	150 – 247	0.003 – 2.3	$\{10\overline{1}0\},\{10\overline{11}\}$
50% KOH in H_2O	83	< 0.001	None
10 – 50% KOH in Ethylene Glycol (CH_2OHCH_2OH)	90-182	0.0015 – 1.3	$\{10\overline{1}0\}$
50% NaOH in H_2O	100	< 0.001	None
20% NaOH in Ethylene Glycol	178	0.67 – 1.0	None
50% Aqueous Ammonium Hydroxide	75	< 0.001	None
40% Aqueous Tetraethylammonium Hydroxide (TEAH)	91	0.007	$\{10\overline{11}\}$
40% Aqueous Tetramethylammonium hydroxide (TMAH)	76	0.013	$\{10\overline{11}\}$

6.3. Discussion of advantages and disadvantages of wet etching

Crystallographic wet etching has several advantages over dry etching and photo-enhanced wet etching. Because wet etching processes are gentler than dry etching, the surface damage should be much lower or even nonexistent for wet etching. For fabricating laser cavities, the crystallographic nature of the etch also guarantees the parallelism of the mirrors. The smoothness of the surfaces is another great advantage of crystallographic etching for GaN; this is the only etching technique to date that has produced vertical walls in GaN with a roughness less than 5 nm.

The cost of fabricating semiconductor devices is dependent upon the number of processing steps. At first glance, a two-step etching process seems to be a disadvantage, because it adds one processing step. On the contrary, in many cases one of the most difficult and costly steps can be eliminated by using crystallographic etching. Once etching is complete, often the next step is to deposit metal contacts. This involves a careful alignment procedure in order to ensure that the metal contacts are aligned properly with the etched features. For crystallographic etching, the annealed Ni and Ti masks can also serve as electrical contacts. The electrical contacts are therefore automatically self-aligned, guaranteeing proper positioning.

The only major obstacle to be overcome for fabrication of laser cavities by crystallographic etching is difficulty in making smooth sidewalls with lateral dimensions larger than approximately 10 μm. As etching proceeds, steps form in the exposed surface as some areas apparently etch at slightly different rates than adjacent areas. It is possible that this effect is defect-related, so that the problem will not occur in crystals with very low defect densities. More experimentation could also result in the discovery of conditions which prevent these steps from occurring, possibly through the use of different chemicals or better control of the etching temperature. Despite the difficulties which have been encountered in this area to date, this method has been used for fabricating optically pumped lasers which will be described in the next chapter.

7. Lasers

7.1. Heterostructure design

In Chapter 2, a laser was described as an optical gain region inside an optical resonator. The structure presented here for fabricating optically pumped lasers is the InGaN/GaN double heterostructure (DH) shown schematically in Figure 7.1.1. The optical gain region is the $In_{0.09}Ga_{0.91}N$ layer. The band gap of InGaN is less than that of GaN, so electrons and holes generated near the InGaN layer fall into it. This creates a high density of electrons and holes in the InGaN layer for efficient recombination.

In addition to having a lower band gap than GaN, InGaN also has a higher index of refraction. This has the advantage of allowing optical waveguiding in the active region. Optical waveguiding in double heterostructures is dealt with in detail in many textbooks, and so will not be discussed here in detail. For a derivation of the waveguiding properties of these structures see, for example, Appendix 5 of Coldren & Corzine's *Diode Lasers and Photonic Integrated Circuits*, John Wiley & Sons, Inc., 1995.[149] Calculations for this InGaN/GaN DH were done using a computer simulation, and a single guided mode was found. The electric field amplitude distribution of this mode is shown in Figure 7.1.1, superimposed on the schematic of the structure. It can be seen that this mode has its maximum in the InGaN region, which is to be expected because the InGaN region has the highest index of refraction.

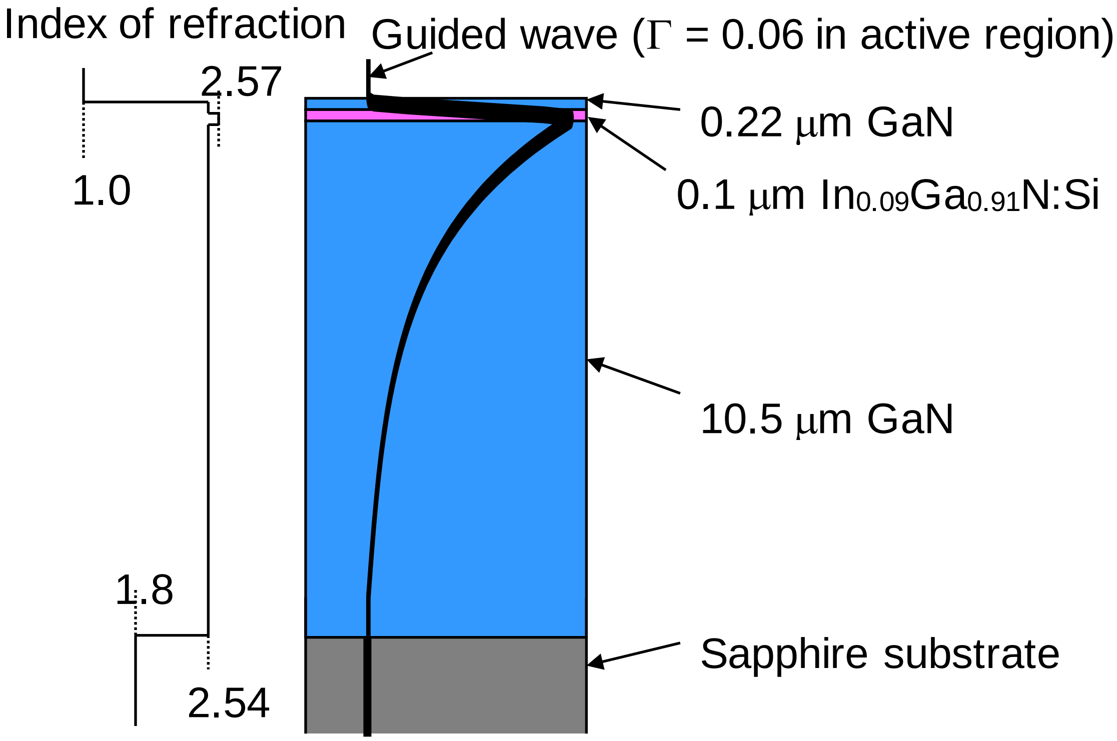

Figure 7.1.1: Schematic of the InGaN/GaN double heterostructure laser structure. The active region consists of Si-doped $In_{0.09}Ga_{0.91}N$, which has a refractive index $\bar{n} = 2.57$. The cladding layer is undoped GaN, $\bar{n} = 2.54$. This structure is grown on *c*-plane sapphire, $\bar{n} = 1.8$.

The waveguiding properties of a slab waveguide allow propagation of light with any polarization, but introduction of a laser cavity causes waves with a transverse electric (TE: electric field in the plane of the waveguiding layer) polarization to be favored over those with a transverse magnetic (TM: magnetic field in the plane of the waveguiding layer) polarization. This is because of the dependence of reflectivity on angle of incidence for TE and TM polarizations. A simple ray tracing model of waveguiding in a dielectric slab shows that the light is incident on the end facets at a slight angle. This is shown schematically in Figure 7.1.2.

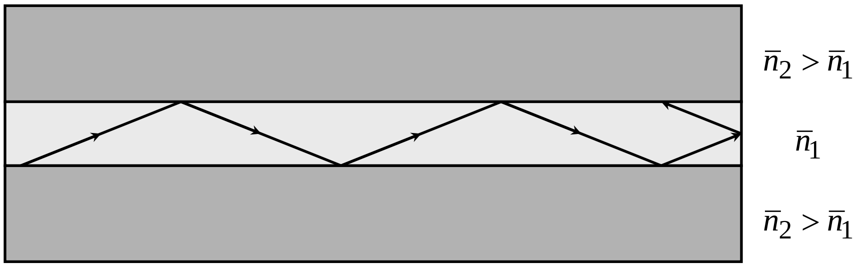

Figure 7.1.2: Trajectory of a light ray guided in a laser cavity with a dielectric slab waveguide.

The small incident angle at the facets has a large effect on the optical output of the laser cavity. According to the Fresnel equations, the reflectivity of a surface is dependent upon the polarization of the light for off-normal incidence. The electric field vector **E** is normal to the *plane of incidence*[e] for TE modes in a slab waveguide laser. The amplitude reflection coefficient for the TE modes is given by

$$r_\perp \quad = \quad -\frac{\sin(\theta_i - \theta_t)}{\sin(\theta_i + \theta_t)}, \qquad \textbf{Equation 7.1.1}$$

where θ_i is the incident angle on the facet inside the cavity and θ_t is the transmission angle.[f] The amplitude reflection coefficient when **E** lies in the plane of incidence (TM modes) is

$$r_\parallel \quad = \quad \frac{\tan(\theta_i - \theta_t)}{\tan(\theta_i + \theta_t)}. \qquad \textbf{Equation 7.1.2}$$

The reflectivity as a function of angle for TE and TM modes are plotted in Figure 7.1.3 for all angles up to θ_{crit}, the critical angle for total internal reflection. For all angles, the reflectivity of the TM mode is lower than that for the TE mode. As a result, the round trip net gain is always higher for TE modes than for TM modes, so lasers which use slab waveguiding are strongly TE polarized above the laser threshold.

---

[e] The plane of incidence is the plane containing the incident, reflected, and transmitted beams in a ray diagram; in Figure 7.1.2, the plane of the page is the plane of incidence.

[f] The derivation of Equation 7.1.1 and Equation 7.1.2 can be found in E. Hecht's *Optics, 2nd Edition*, pp. 94-96, Addison-Wesley Publishing Company, 1987.

The overlap of the guided mode with the active region is called the confinement factor Γ. It is defined as the fraction of optical energy contained in the active region

$$\Gamma = \frac{\int\limits_{\substack{\textit{active}\\\textit{region}}} \left|U(x,y)\right|^2 \mathrm{d}x}{\int_{-\infty}^{\infty} \left|U(x,y)\right|^2 \mathrm{d}x}, \qquad \textbf{Equation 7.1.3}$$

where $U(x,y)$ is the amplitude of the electric field as a function of x and y coordinates, and the amplitude is assumed to be independent of position in the propagation direction z. Γ in the double heterostructure is 6%, which is typical for a semiconductor laser.

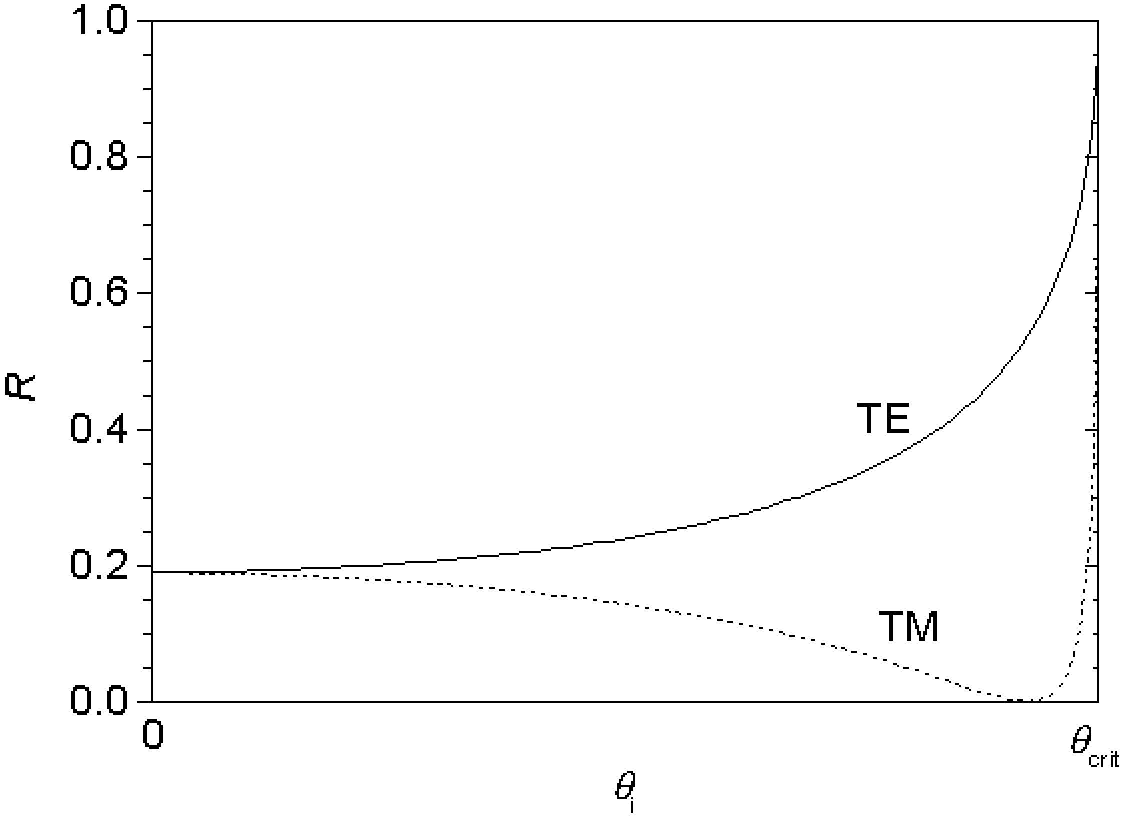

Figure 7.1.3: Power reflectivity *R* for TE and TM modes in a laser with a slab waveguide, as a function of incident angle.

The silicon doping of the active region in this structure is significant. In stimulated emission measurements without a cavity, the high Si doping concentration (carrier concentration $n = 2 \times 10^{18}$ cm^{-3}) in the InGaN active region was found to lower the threshold for stimulated emission. An identical but undoped InGaN double heterostructure displayed no stimulated emission for pumping intensities even up to the damage threshold. Several studies on the effects of Si doping of GaN epilayers,[150,151] InGaN/GaN QW's,[152,153,154] and GaN/AlGaN QW's[155,156] have found that Si doping increases the luminescence of the material. Nakamura *et al.* suggested that the silicon doping enhances stimulated emission by the formation of localized quantum-dot-like states in the InGaN layer.[157] In addition to this effect, the carrier lifetime decreases with increasing doping, since the probability of radiative recombination is proportional to the number of carriers present. This increases the ratio of radiative recombination to nonradiative recombination. Cho *et al.* measured a considerable decrease in lifetime from ~30 ns for $n < 1 \times 10^{17}$ cm^{-3} to ~4 ns for $n = 3 \times 10^{19}$ cm^{-3}.[154] A third advantage caused by the doping is that increased Si doping appears to improve the interface properties between the InGaN and GaN epilayers.[154]

7.2. Cleaved-facet lasers

Optically pumped lasing has previously been demonstrated in InGaN/GaN multiple quantum wells[111,158] and InGaN/GaN single heterostructures.[159] Optically pumped InGaN/GaN double heterostructure lasers have now been added to this list. Demonstration of lasing from a thick InGaN active region reflects the high quality of the material and the interfaces between the active region and the cladding regions. This is unusual, due to difficulties normally encountered when growing thick InGaN layers; at the InGaN growth temperature (800°C), the material quality tends to degrade and the surface roughness tends to increase.[160]

Cleaving has been used to fabricate laser cavities made with the double heterostructure described in Section 7.1. After thinning the sapphire substrate to 200 μm, the laser facets are formed by scribing and cleaving along the *m*-plane of the substrate, as described in Section 4.2. The samples are then mounted in an edge-emitting configuration. This configuration is similar to that used for net optical gain measurements, and is illustrated in Figure 7.2.1. A 200-μm-wide region of the cavity is pumped using a nitrogen laser emitting at 337.1 nm. This laser provides a pulse width of 800 ps and a maximum power density of 98 MW/cm^2. Neutral density filters are used to attenuate the pumping power.

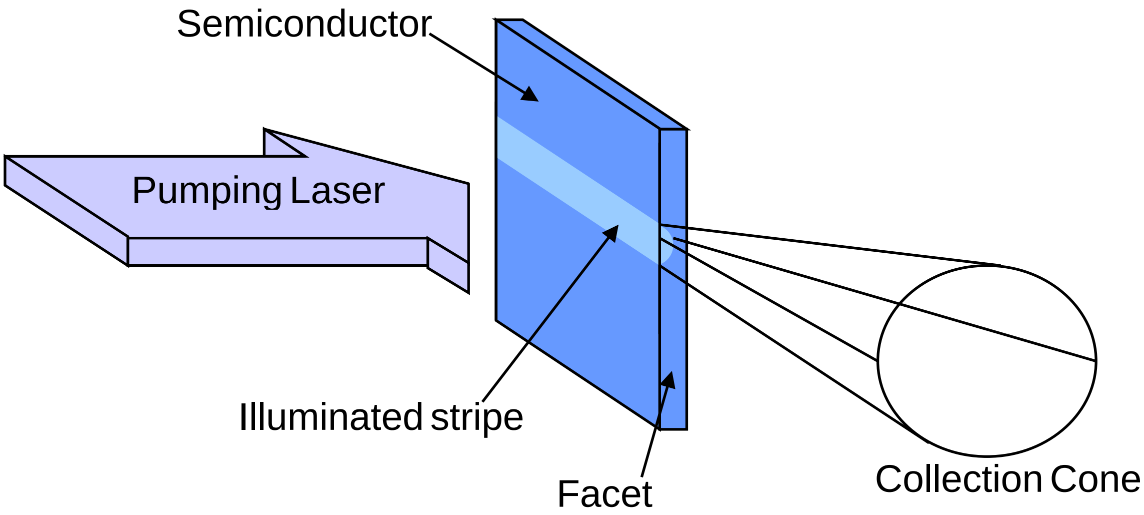

Figure 7.2.1: Schematic of optical pumping and collection optics for a laser cavity in edge-emitting configuration.

Each sample has an optical damage threshold. If pumping powers above the threshold are used, the optical emission from the sample decreases sharply, and burn marks appear on the sample. The damage seems to be induced not by the pumping source but rather by the stimulated emission in the semiconductor. This was proposed recently by D. A. Cohen *et al.* when they observed that the damage occurs at the ends of optically pumped stripes, where the intensity of the stimulated emission is the highest.[161] This hypothesis is further supported by this work, because the damage threshold is found to be much higher for short cavities (greater than 98 MW/cm^2 for 50 μm cavities) than it is for longer cavities (~20 MW/cm^2 for 1 mm cavities).

The light emitted from one of the laser facets is collected and focused into the entrance slit of a 0.75 m spectrometer. A schematic of the pumping and collection optics is shown in Figure 7.2.2. The N_2 laser emission is focused between a pair of slits made with razor blades. The slits are positioned so that the light passing through is as uniform as possible. The light is then focused on the sample. The emission from the sample is collimated and focused into the monochromator. The light is detected using a GaAs photomultiplier, and the signal is processed using a current amplifier and a boxcar amplifier.

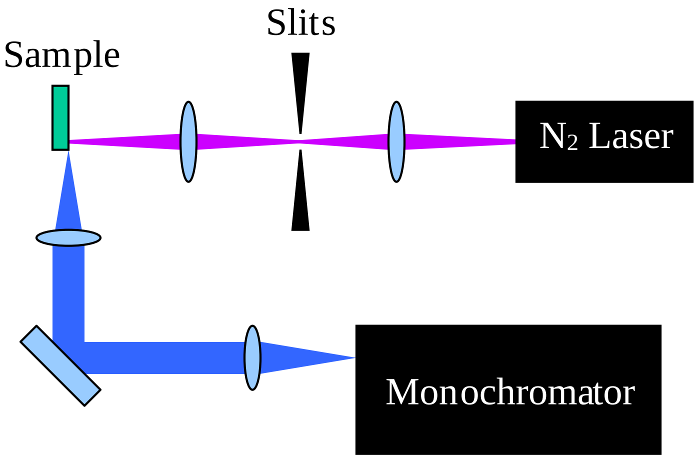

Figure 7.2.2: Pumping and collection optics for stimulated emission measurements.

Figure 7.2.3 shows both the integrated intensity and the peak intensity of an InGaN/GaN laser as a function of excitation power density. The inset depicts an expanded view of the low power section of the graph. Inspection of the inset reveals that both the integrated intensity and the peak intensity of the emission increase linearly with incident excitation power density up to 1.0 MW/cm^2. A marked change in the light-versus-excitation characteristic occurs at the incident threshold density of 1.3 MW/cm^2. Above threshold, the slope increases by a factor of 34 for the integrated intensity, and by a factor of 210 for the peak intensity. This drastic change in differential quantum efficiency is due to the onset of laser oscillation.

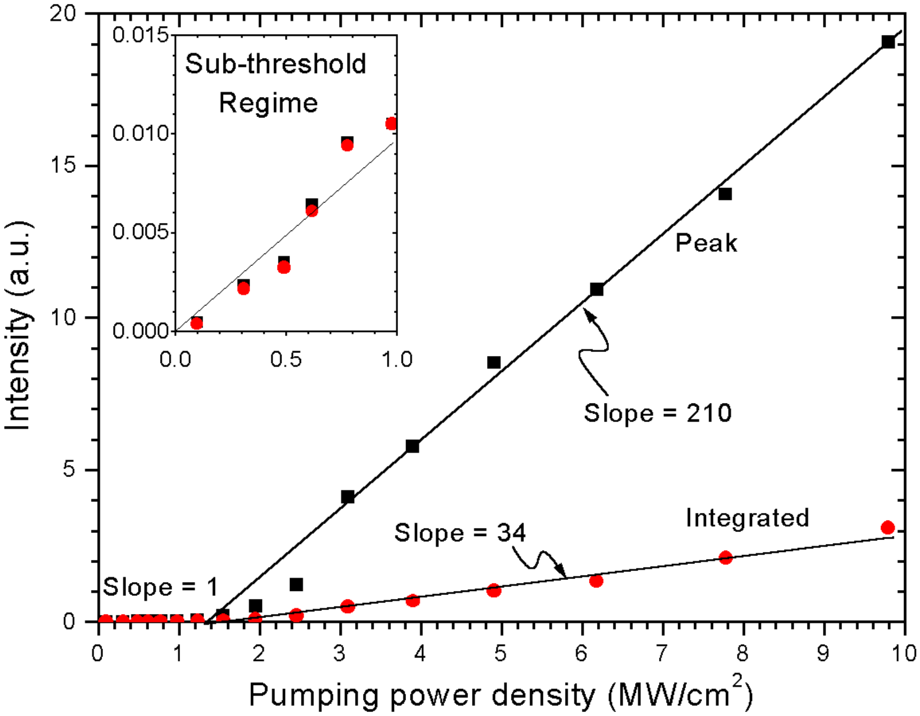

Figure 7.2.3: Peak and integrated emission intensities as a function of incident excitation power density. The inset shows an expanded view of the low-power regime. Above threshold, the slope increases by a factor of 34 and 210 for the integrated and peak intensities, respectively.

Figure 7.2.4 shows emission spectra of the InGaN/GaN laser below and above the threshold pumping power density $P_{threshold}$ = 1.3 MW/cm^2. Below 1.2 MW/cm^2 a broad spontaneous emission band is observed, centered at 3.18 eV (390 nm). A shoulder appears at 1.2 MW/cm^2, which rapidly grows into a sharp peak centered at 3.15 eV, red-shifted as compared to the spontaneous emission peak. The optical gain is highest where the spontaneous emission is strongest, but absorption near the band gap decreases as the wavelength increases, red-shifting the net gain spectrum. The full width at half-maximum (FWHM) decreases from

115 meV at 1.0 MW/cm^2 to 23 meV at 1.6 MW/cm^2, and eventually reaches a minimum of 13.5 meV at 3.1 MW/cm^2. In the spontaneous regime, the FWHM increases with pumping power from 94 meV at 0.1 MW/cm^2 up to 115 meV at 1.0 MW/cm^2, due to band filling in the InGaN. In the lasing regime, the FWHM increases from 13.5 meV at 3.1 MW/cm^2 to 18.5 meV at 10 MW/cm^2, due most likely to an increase in the number of lasing modes. This effect has also been observed in laser diodes reported by Nakamura et al.[105]

The pronounced decrease in FWHM and strong increase in slope efficiency are indicators of either stimulated emission or lasing. Above threshold, however, the light output becomes highly TE polarized because of optical feedback from the facets, clearly indicating lasing. The TE/TM intensity ratio above threshold is approximately 100, as shown in Figure 7.2.5. The laser emission dominates the TE mode, while the TM mode displays only the broad, low intensity spontaneous emission.

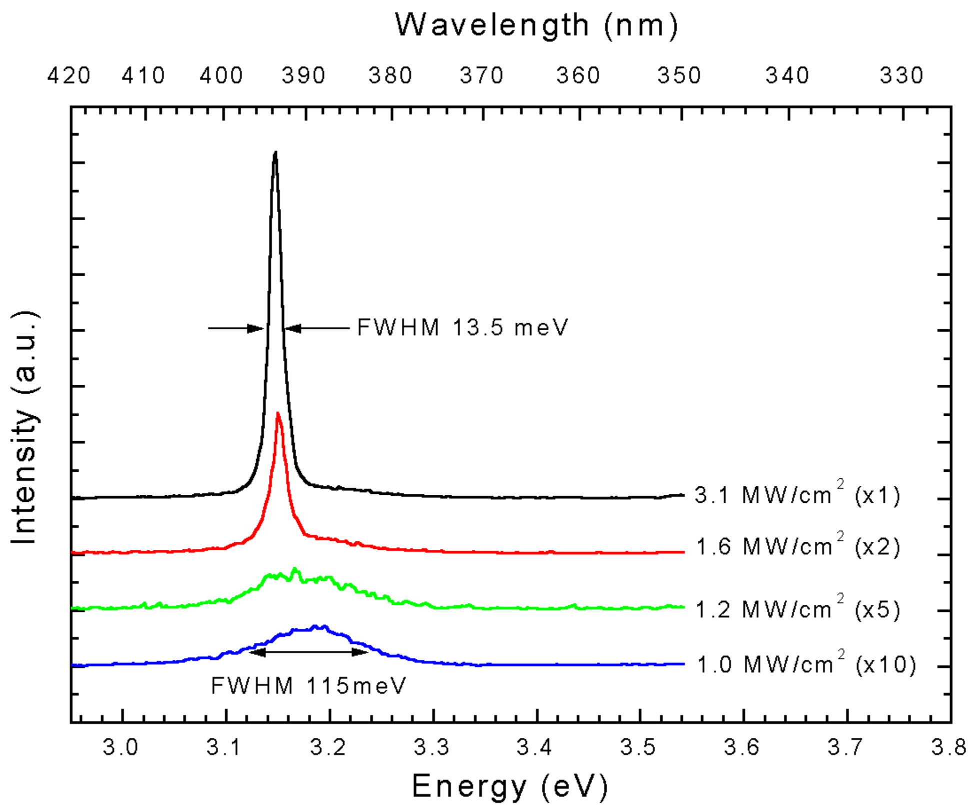

Figure 7.2.4: Emission spectra for different excitation levels. At sub-threshold excitation intensities, a broad band centered at 3.18 eV (390 nm) is visible. Above threshold, a narrow peak emerges, centered at 3.15 eV (394 nm).

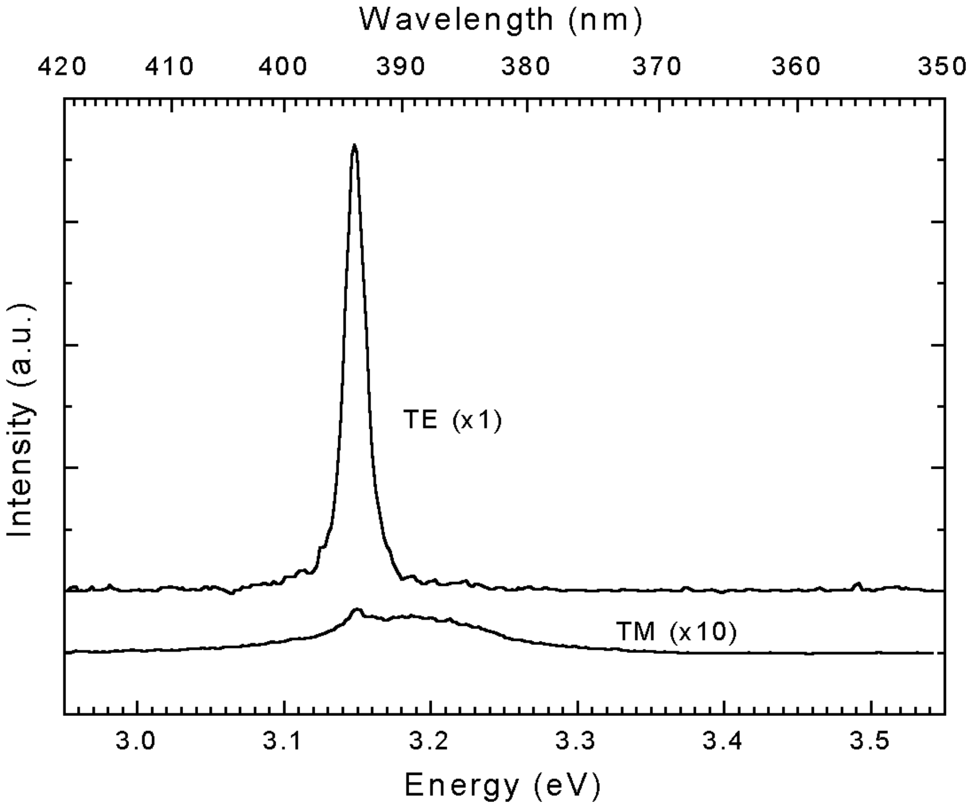

Figure 7.2.5: Polarized emission spectra taken at $2.4\times P_{\text{threshold}}$. The TM mode shows the broad spontaneous emission spectrum, while the TE mode shows the laser peak. The TE/TM intensity ratio is 100 at this excitation level.

With a cavity length of 1 mm, the longitudinal cavity mode spacing is 0.024 nm. The optical modes can not be resolved due to pulse-to-pulse amplitude noise of the excitation source. Variation in intensity between successive pulses from our nitrogen laser are approximately 20%. This variation gives rise to chirping, whereby the modes of the cavity shift, washing out the mode structure.

These are the first lasers fabricated from an InGaN/GaN double heterostructure. Laser action is shown by a dramatic reduction in linewidth along with a strong increase in differential quantum efficiency and high TE polarization, all occurring simultaneously at a threshold pumping power density of 1.3 MW/cm^2. While the striations in the cleaved facets limit the reflectivity, cleaved-facet lasers on sapphire substrates are a relatively simple and straightforward way to fabricate viable GaN-based lasers.

7.3. Wet-etched-facet lasers

Recently the same InGaN-GaN double heterostructure has been used to demonstrate optically pumped wet-etched laser action, using the methods developed in Chapter 6. This is the first reported demonstration of wet-etched GaN-based laser facets.

180-nm-thick annealed Ni masks are used to define cavities with lengths varying from 50 μm to 500 μm. The unusually thick Ni layer is used to minimize the light penetrating into the masked area during PEC etching. The edges of the masks are aligned with the $\langle 11\bar{2}0 \rangle$ direction of the GaN, so that the resulting PEC-etched sidewalls correspond with the $\{10\bar{1}0\}$ plane for subsequent crystallographic etching.

The PEC etching is done under voltage-biased conditions in a 0.03 M KOH solution at room temperature. During etching, the samples are clamped against a nickel bar and immersed along with a gold wire cathode in the aqueous KOH solution. Voltage and current are both monitored and a DC power supply is used to apply a bias voltage of 2 V between the anode and the cathode. Ultraviolet illumination is provided by a 200W Hg lamp, and a silicon wafer is used as a cold mirror to reduce heating by increasing the ratio of UV to IR illumination. This is illustrated in Figure 7.3.1. The index of refraction of Si varies between 5 and 7 in the spectral range from 300 – 400 nm and drops to less than 3.5 above 1000 nm. This causes the power reflectivity at a 45° incidence angle to vary from ~50% in the near UV to ~30% in the near IR. Thus, using the light reflected from the silicon wafer increases the ratio of UV to IR light, allowing a relatively high etch rate while minimizing any heating effects which may occur.

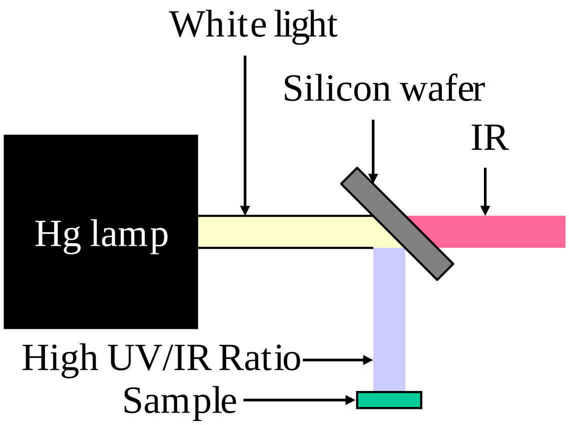

Figure 7.3.1: Schematic showing the positioning of the silicon wafer and sample during PEC etching.

The time required to produce vertical sidewalls extending down to the sapphire substrate under these conditions is 4 hours. A typical PEC-etched sidewall in this material is shown in Figure 7.3.2(a). The nickel mask is visible at the top of the image, and is allowed to remain in place throughout the subsequent crystallographic etching. As the image shows, the PEC-etched sidewall is extremely rough and has a fibrous texture, although the lower GaN surface has etched away cleanly from the sapphire substrate. The clean sapphire surface shows the effectiveness of the bias voltage in eliminating the islands often formed on the sapphire substrate by uneven PEC etching of the GaN. Note that there are some deep holes in the top 1 μm of the structure, near the InGaN layer. These holes form during PEC etching, but the etching mechanism is not yet understood.

The sidewall produced by PEC etching is too rough to be used as a laser facet, since the reflectivity is strongly dependent upon surface roughness. Crystallographic etching in molten KOH is used to smooth the PEC-etched surface to improve the

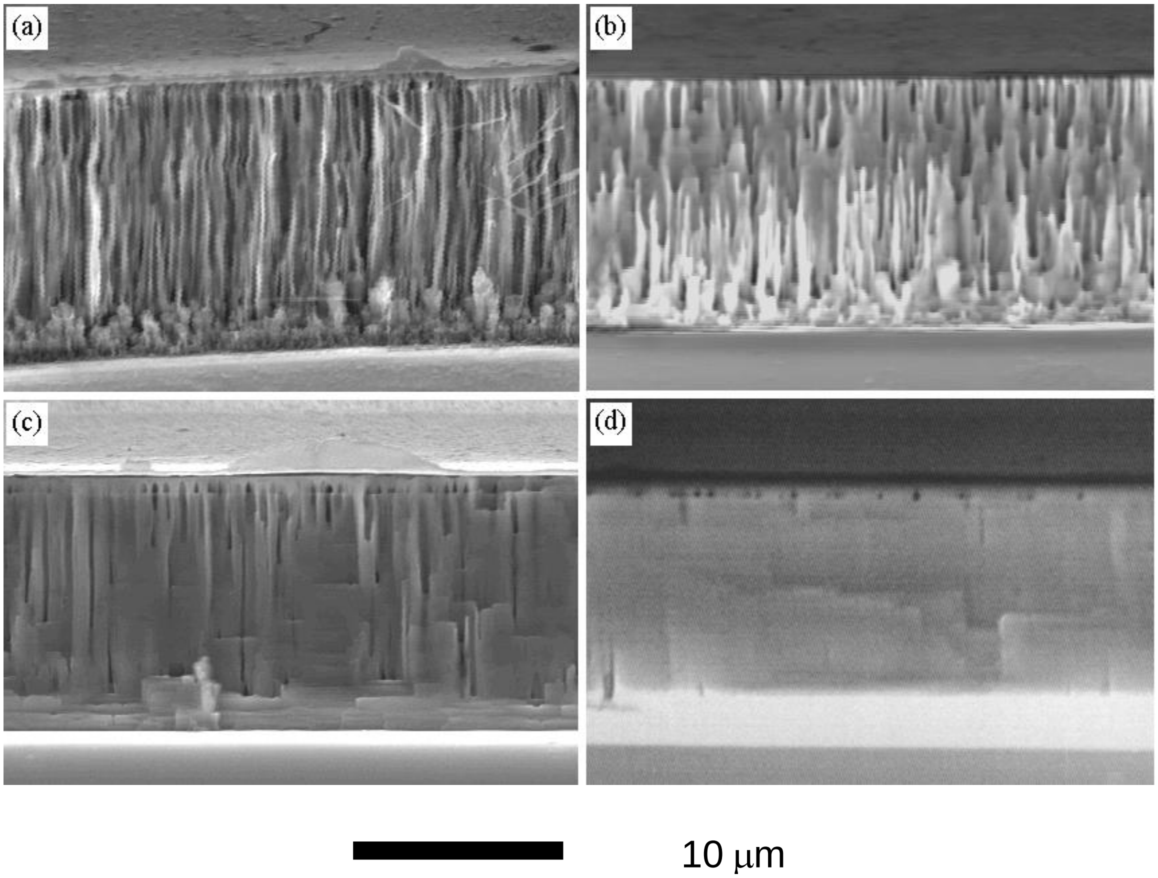

Figure 7.3.2: Smoothing of a surface produced by photo-enhanced electrochemical (PEC) etching of an InGaN/GaN double heterostructure. The 10 μm bar underneath the figure is valid for all of the SEM images. (a) PEC-etched surface before smoothing by crystallographic etching in molten KOH at 175°C. (b) PEC-etched surface after smoothing for 1 min. (c) After smoothing for 3 min. (d) After smoothing for 9 min.

reflectivity. The series of SEM images in Figure 7.3.2(b) – Figure 7.3.2(d) shows the effect that etching in 175°C molten KOH has on the PEC-etched sidewall. The etch rate at this temperature is approximately 0.05 μm/min. The fibrous PEC-etched surface shows considerable smoothing after only 1 minute of crystallographic etching, as can be seen in Figure 7.3.2(b). Further improvement is observed in Figure 7.3.2(c) after three minutes of crystallographic etching. After five minutes of etching, no further smoothing occurs; the image shown in Figure 7.3.2(d) after nine minutes of etching is very similar to images taken anywhere in the range of five to ten minutes. Note that the density of holes in the top 1 μm does not tend to change during crystallographic etching. Horizontal steps like those across the center of Figure 7.3.2(d) are common features produced by crystallographic etching in KOH. These may be due to etch rate anisotropy in the [0001] and $[000\bar{1}]$ directions. The lateral dimension of the smooth areas before a step occurs is generally on the order of 10 μm.

After the crystallographic etching step, the nickel mask is removed by wet etching in a 1 HCl : 1 HNO_3 : 3 H_2O solution. The configuration for optical pumping is identical to that described for the cleaved-facet lasers described in Section 7.2.

Several spectra for a 500 μm wet-etched cavity are shown in Figure 7.3.3. Below the threshold pumping power two broad bands are visible, one at 3.18 eV (390 nm) and another at 3.32 eV (373 nm). The relative intensities of the two peaks below threshold are constant over a change in pumping power of two orders of magnitude. The peak at 390 nm is similar to the peak observed in the sub-threshold regime for the cleaved-facet lasers made from the same material. The higher energy peak is probably emitted from the edges of the sample, where the HVPE-grown material is exposed by the undercutting that occurs during PEC etching. The energy of the peak is well below the bandgap of GaN, indicating not a band-to-band or excitonic transition but rather a transition involving a shallow donor and/or a shallow acceptor. Near the 2.7 MW/cm^2 threshold pumping power density a narrow peak appears at 3.13 eV (396 nm). As the pumping power is increased the peak shifts to slightly lower energy.

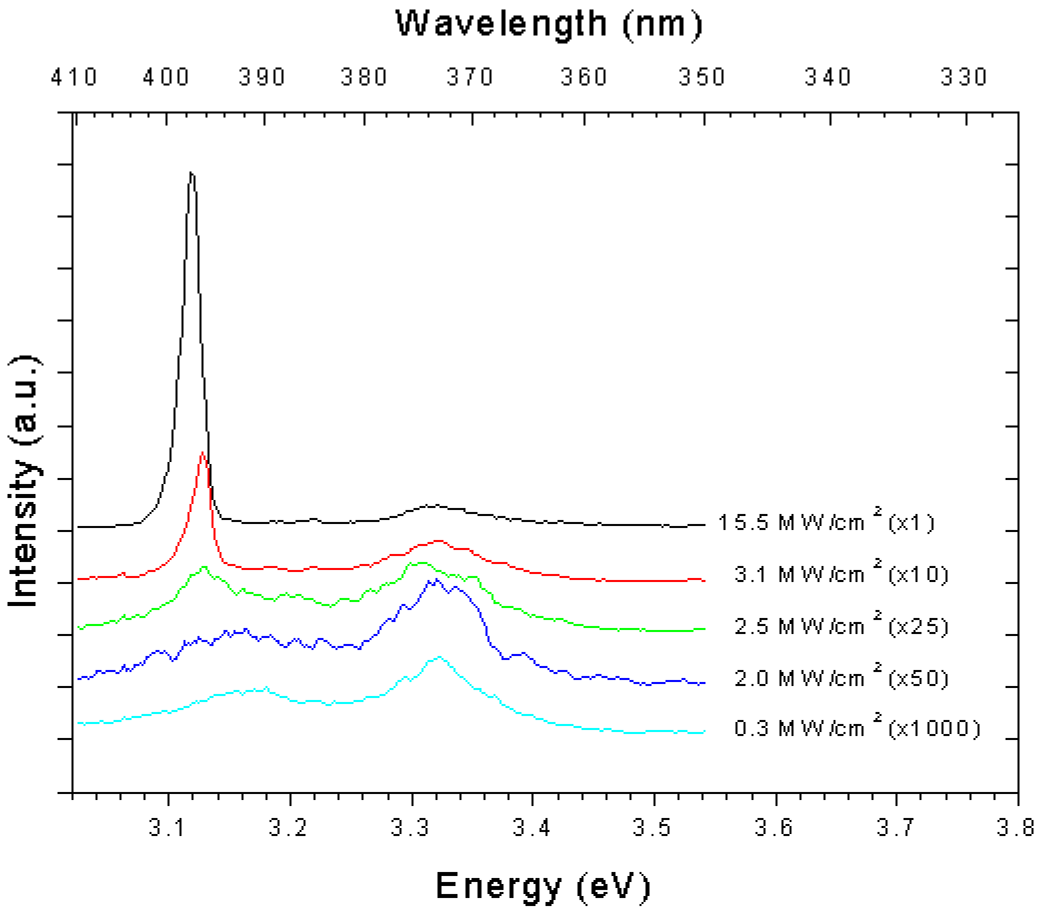

Figure 7.3.3: Emission spectra of a 500 μm wet-etched laser cavity for several different pumping power levels. At sub-threshold excitation powers, two broad bands are visible, one at 3.18 eV (390 nm) and another at 3.32 eV (373 nm). Above threshold, a narrow peak emerges at 3.13 eV (396 nm) and moves to slightly lower energy as pumping power is increased.

A plot of the peak emission intensity, FWHM, and TE/TM ratio for this cavity is shown in Figure 7.3.4. As with the cleaved-facet lasers, the sharp decrease in the FWHM from ~100 meV to less than kT and the concurrent change in slope indicate only the onset of stimulated emission, while the increase of the TE/TM ratio indicates feedback from the laser cavity mirrors. Again, laser modes have not been resolved due to pulse-to-pulse amplitude noise of the excitation source.

When fabricating cleaved-facet lasers, it is difficult to make cavities less than 1 mm in length, but with wet etching lasers have been fabricated with lengths as small as 50 μm. In Section 2.3 the relationship between facet reflectivity, absorption, optical gain, and cavity length was calculated. By rearranging Equation 2.3.2, one can see that a plot of inverse cavity length vs. threshold optical gain should yield a straight line if the absorption and reflectivity is constant:

$$g\big|_{\text{at threshold}} = \alpha - \frac{\ln(R)}{L}. \qquad \textbf{Equation 7.3.1}$$

This straight-line plot is realized in Figure 7.3.5 below, if it is assumed that the optical gain is simply proportional to the incident pumping power. This assumption is commonly called the “linear gain model.” This plot allows a comparison of the reflectivity R with the absorption α. Assuming a reflectivity near the ideal value of 0.2, which is reasonable according to the calculations done in Section 2.3 and the field-effect SEM images in Section 6.2, then the absorption in the material is ~15 cm^{-1}, which is a typical value for this materials system.[162,163]

Two points each for 200 μm and 100 μm cavities that were made by PEC etching without subsequent crystallographic etching are also added to this figure. A linear fit for these points indicates that crystallographic etching increases the facet reflectivity. The linear fit for the PEC-etched cavities is constrained to cross the y axis at the same point as

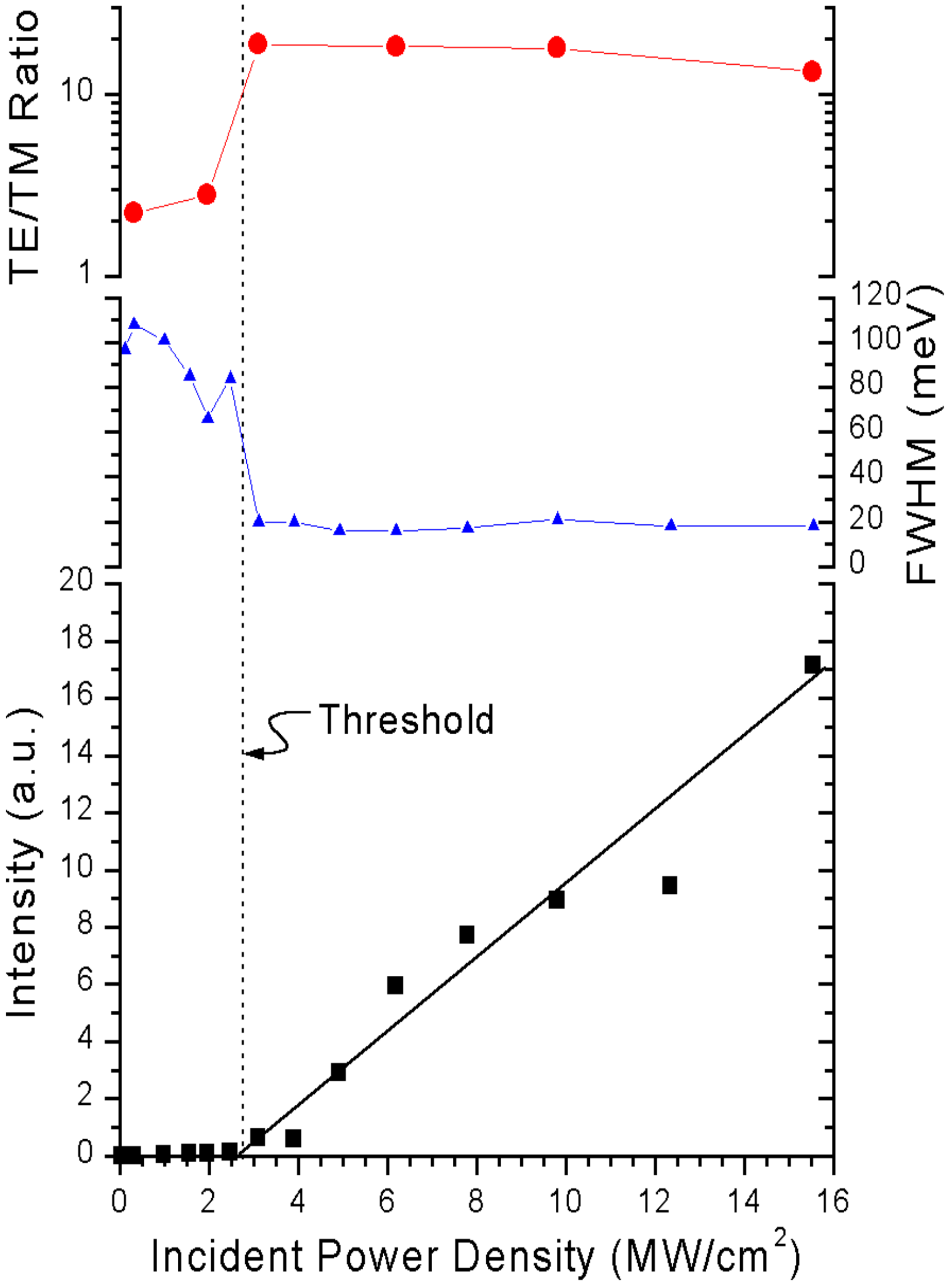

Figure 7.3.4: Peak emission intensity, FWHM, and TE/TM ratio for a 500 μm wet-etched laser cavity over a wide range of pumping power densities. The laser threshold is at 2.7 MW/cm^2.

the line for crystallographically etched cavities. This constraint is equivalent to requiring that the threshold be the same for infinitely long cavities with different, non-zero facet reflectivities. For an infinitely long cavity, the threshold optical gain is equal to the absorption, independent of the reflectivity, as can be seen in Equation 7.3.1.

Comparing the average threshold power for the 200 μm cavities without crystallographic etching to the linear fit for crystallographically etched cavities indicates that the power reflectivity increases by a factor of 2 as a result of smoothing. If the assumption that the reflectivity of the crystallographically etched facets is near the ideal value of 0.2 were not correct, then the increase in reflectivity as a result of smoothing would be even more dramatic.

The first GaN-based lasers fabricated by wet etching have been presented. Laser action is shown by a dramatic reduction in linewidth along with a strong increase in differential quantum efficiency and high TE polarization, all occurring simultaneously at a threshold pumping power density that varies with the inverse cavity length. This work indicates that smoothing the facets of GaN-based lasers with a crystallographic etching step increases the reflectivity considerably.

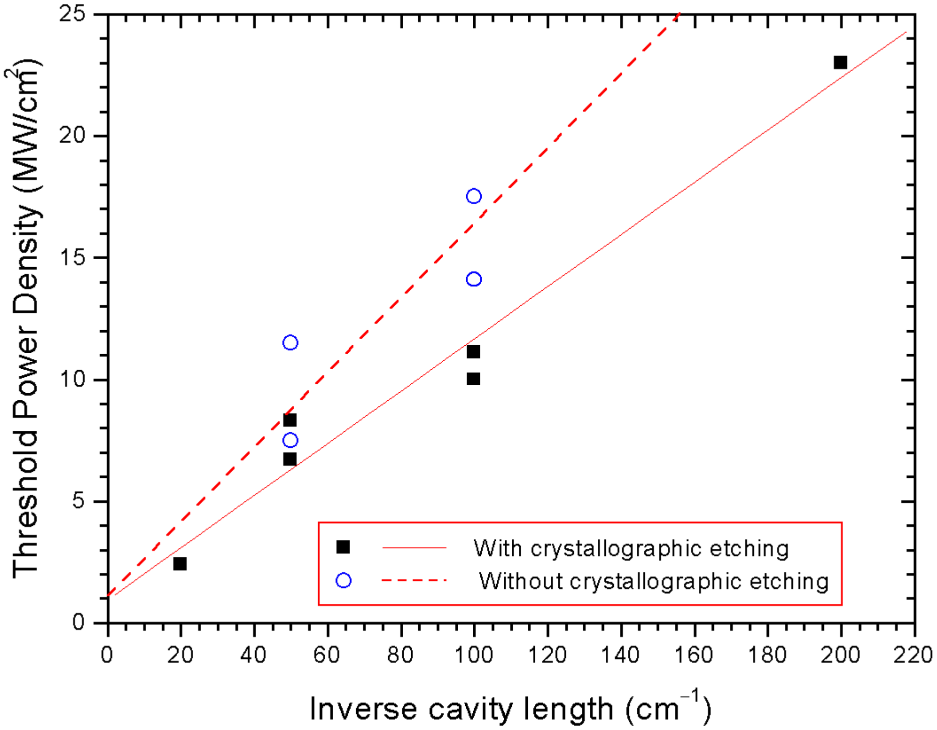

Figure 7.3.5: Measured threshold current density as a function of inverse cavity length. The straight line is a fit to the points for the crystallographically etched cavities.

8. Conclusions

8.1. Techniques for facet fabrication

Many possible techniques for fabricating smooth facets for GaN-based lasers have been demonstrated and compared. On the basis of the theoretical model presented in Chapter 2 which shows a decrease in reflectivity as a function of roughness, a reasonable goal for RMS facet roughness is $\Delta d = 4$ nm.

Dry etching methods, while currently the most common used because of the high etch rates, anisotropy, and reproducibility which they offer, have not been successful at producing smooth facets, with only one group reporting an ability to make vertical sidewalls with a roughness less than 50 nm. Dry etching also has the disadvantage of causing ion-induced damage which affects the stoichiometry and electrical properties of the etched surfaces.

Cleaving offers a low damage method for fabricating laser facets. Cleaved facets on sapphire substrates, however, have rough morphologies caused by a misorientation of the GaN epilayers with respect to the sapphire substrate; cleaved facets on SiC and spinel substrates, and presumably also on pseudo-bulk GaN substrates, generally have atomic-scale roughness, but with the disadvantage of more expensive substrate materials.

Photoenhanced electrochemical (PEC) etching is an area that has received a great deal of attention in the GaN research community in the last two years. It has the potential of offering a low-damage, high-etch-rate method for fabricating devices, and can be used for selective etching based on band gap or doping concentration, but it is very sensitive to crystal defects and no method for PEC etching of p-type material has yet been demonstrated. While smooth etched surfaces have been reported by two different groups, smooth, vertical sidewalls have yet to be demonstrated using this method.

During the course of this thesis, a two-step method for crystallographic etching of GaN has been discovered. This method will not supplant existing technology, but can be used to improve the optical and perhaps also the electrical properties of the surfaces produced by another etching technique. Crystallographic etching can be used to make undercut, overcut, or vertical sidewalls in GaN. The vertical sidewalls fabricated with this method have an RMS roughness less than 5 nm, but the largest facets fabricated to date have a lateral extent only on the order of 20 μm. For high-power laser applications, lateral extents on the order of 100 μm or more will be required.

8.2. Demonstrations of cleaved and wet-etched lasers

In the course of this dissertation, two different types of laser cavities have been demonstrated. Both were made with the same InGaN/GaN double heterostructure material, and are the first examples of lasers made with this structure. The facets of the cleaved lasers have an RMS roughness of 16 nm. Above the threshold optical pumping power density of 1.3 MW/cm^2 the differential quantum efficiency increases by a factor of 34, the full width at half maximum of the peak drops below kT, and the TE/TM ratio increases by nearly two orders of magnitude, indicating the onset of laser oscillation.

The wet-etched-facet lasers presented here are the first ever reported. The PEC-etched facets were initially very rough, but crystallographic wet etching smoothed them, increasing the reflectivity by at least a factor of two. As with the cleaved-facet lasers, the differential quantum efficiencies increased, the full widths at half maxima decreased, and the TE/TM ratio increased as laser oscillations began in the wet-etched structures. The threshold optical pumping power densities for the wet-etched lasers varied with the length of the cavities, from 2.4 MW/cm^2 for 500 μm cavities to 23 MW/cm^2 for 50 μm cavities. An analysis of the threshold pumping power as a function of cavity length allowed an absorption coefficient of 15 cm^{-1} to be deduced for the laser structures.

8.3. Proposed directions for future research

The wet etching techniques which have been developed, both photoenhanced and crystallographic, are in need of further study. The physical processes involved in both techniques are currently understood poorly, and the field would benefit greatly from more experimental and theoretical work aimed at elucidating the etching mechanisms.

In the arena of PEC etching, a study on the surface damage induced by the method needs to be done to assess the utility of this method in industry. In particular, does this method cause changes in the stoichiometry of the top few monolayers of the crystal, as dry etch techniques do, and does hydrogen penetrate into in crystal, possibly passivating acceptors in p-type material?

Crystallographic etching of GaN is such a new phenomenon, reported on for the first time in August of 1998, that almost anything that is done with it will be groundbreaking work. Several research groups have shown interest in this work and are beginning to explore the etching characteristics and the possible uses of these crystallographic etching techniques for device applications.[164] For example, crystallographic etching has been used at CREE Research, Inc. to remove unwanted GaN from SiC substrates so that the expensive substrates can be reused.[165] At Cornell University, crystallographic etching is being used to produce vertical walls and to remove unwanted roughness for improved gate metallization on GaN vertical field-effect transistors.[166]

There are still many questions waiting to be answered about wet chemical etching of GaN. A complete mapping out of the etch rate as a function of crystallographic orientation has not yet been attempted, although some information about what such a diagram would look like can be gleaned from the work presented here. Will wet etching techniques even work on single crystal GaN with very low defect densities? How do the etch rates of the various crystal planes depend on the concentrations of aluminum and indium in their ternary and quaternary alloys with GaN? Does etching passivate acceptors in p-type material? If so, does subsequent annealing reactivate the acceptors? Can crystallographic etching be used to remove the damaged layers produced by dry etching? If so, how do the electrical properties of the surface change after etching? Does crystallographic etching significantly improve the reflectivity of the best dry-etched facets? How can the lateral extents of wet-etched laser facets be increased? There is great potential for the crystallographic etching techniques which have been developed here, but there are still a great many questions to be answered before we will know how and where best to apply them.

9. Appendix A: Miller indices in a hexagonal lattice

Miller indices are used to define planes in a crystal lattice. The conventions used in this work are taken from Sze's *Physics of Semiconductor Devices, 2nd Edition*.[167] For a cubic lattice, three base vectors are required. These three vectors are taken by convention to be along the x, y, and z axes, and the lengths of the vectors are the lattice constants in the respective directions. The Miller indices of a plane are determined by first finding the intercepts of the plane with the three base vectors, then taking the reciprocals of these numbers and reducing them to the smallest three integers having the same ratio. The result is placed in parentheses: (hkl). A set of Miller indices can refer to a single plane, a set of parallel planes, a set of planes with equivalent symmetry, a direction, or a set of equivalent directions. Negative numbers are indicated by placing a bar over the number, as in $(hk\bar{l})$. In a cubic lattice, the symmetries of the crystal are reflected nicely in the Miller indices. For example, the (100) plane is equivalent to (010), (001), $(\bar{1}00)$, $(0\bar{1}0)$, and $(00\bar{1})$.

In a hexagonal lattice, the three base vectors could still be chosen to be orthogonal, but then the symmetries of the crystal are not reflected in the Miller indices. A rotation of 60 degrees around the *c*-axis ($\hat{\mathbf{e}}_4$ in Figure 8.3.1) in a hexagonal crystal results in an equivalent plane. This means that the (100) plane is equivalent (±0.1%) to the (40 23 0), $(\overline{40}\ 23\ 0)$, $(\bar{1}\ 0\ 0)$, $(\overline{40}\ \overline{23}\ 0)$, and $(40\ \overline{23}\ 0)$ planes. As this example illustrates, an orthogonal coordinate system is not well suited to a hexagonal lattice structure. For this reason, four base vectors are used in a hexagonal lattice, as illustrated in Figure 8.3.1. Using this system, the $(10\bar{1}0)$ plane is equivalent to the $(01\bar{1}0)$, $(\bar{1}100)$, $(\bar{1}010)$, $(0\bar{1}10)$, and $(1\bar{1}00)$ planes.

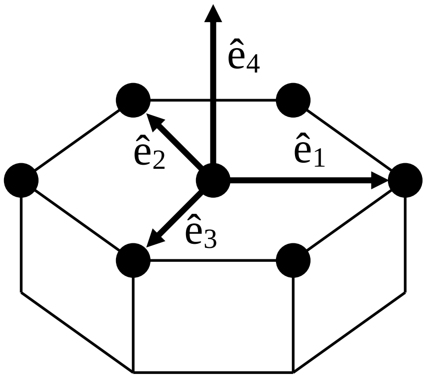

Figure 8.3.1: Base vectors for Miller indices in a hexagonal lattice.

Because four indices are used in a three-dimensional space, not all four are independent. The fourth index, in the direction of the *c*-axis, is independent, but the first three are interrelated. To calculate the relationship between the first three indices, we will consider a plane that intersects the first and second vectors in the positive direction from the origin. The same plane will intersect the third vector at a point in the negative direction from the origin, as shown in Figure 8.3.2. Points **A**, **B**, **C**, and **D** are added for reference. The relationship between the first three Miller indices can be determined by finding the relationship between **AB**, **AC**, and **AD**.

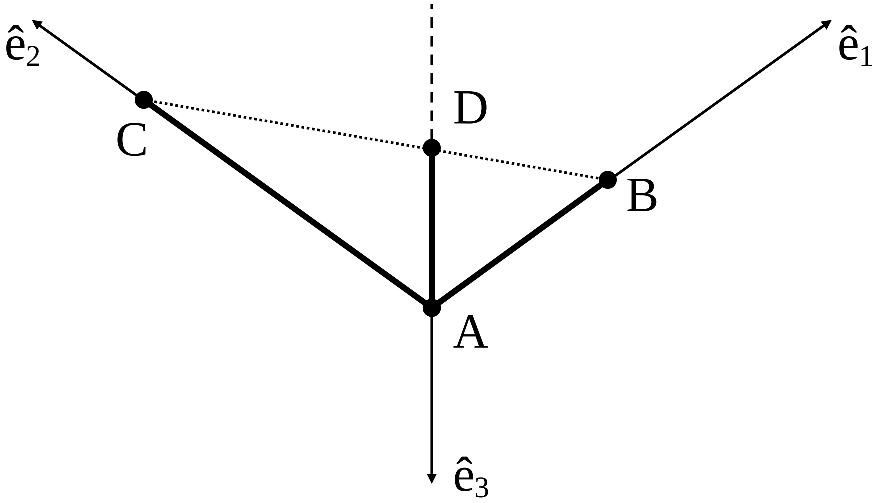

Figure 8.3.2: A plane intersecting the first three directional vectors in a hexagonal lattice at points **B**, **C**, and **D**. The fourth direction is out of the page. Point **A** is at the origin.

To calculate **AD** in terms of **AB** and **AC**, we first construct lines perpendicular to the third vector and intersecting with points **B** and **C**, as shown in Figure 8.3.3. Because they are collinear,

$$\mathbf{AD} = \mathbf{AF} + \mathbf{DF}, \text{ and } \mathbf{HB} = \mathbf{HF} + \mathbf{BF}. \qquad \textbf{Equation 8.3.1}$$

Also,

$$\mathbf{CG} = \mathbf{HF} \quad \text{and} \quad \mathbf{CH} = \mathbf{AG} - \mathbf{AF}. \qquad \textbf{Equation 8.3.2}$$

Next, because $\angle\mathbf{BAD}$ and $\angle\mathbf{CAD}$ are both 60°, it follows that

$$\mathbf{AF} = \frac{1}{2}\mathbf{AB}, \quad \mathbf{AG} = \frac{1}{2}\mathbf{AC}, \quad \mathbf{CG} = \frac{\sqrt{3}}{2}\mathbf{AC} \quad \text{and} \quad \mathbf{EF} = \frac{\sqrt{3}}{2}\mathbf{AB}. \qquad \textbf{Equation } 8.3.3$$

Then, using similar triangles **BDF** and **BCH**,

$$\frac{\mathbf{DF}}{\mathbf{BF}} = \frac{\mathbf{CH}}{\mathbf{HB}}.$$ **Equation 8.3.4**

By combining these four sets of equations and solving for **AD** in terms of **AB** and **AC**, we find the following:

$$\frac{1}{\mathbf{AC}} + \frac{1}{\mathbf{AB}} = \frac{1}{\mathbf{AD}}.$$ **Equation 8.3.5**

The Miller indices are found by taking the reciprocals of the intercepts, and keeping in mind that AD was measured in the negative direction, we find that the third Miller index in hexagonal coordinates is the negative of the sum of the first two.

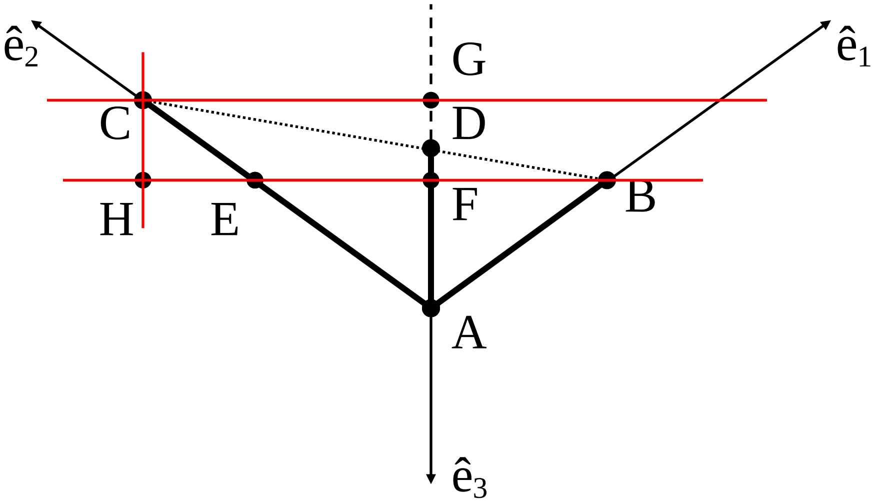

Figure 8.3.3: Geometric constructions for determining the relationship between the first three Miller indices in a hexagonal coordinate system.

Table 9.1 lists the conventions used for planes and directions. All of the planes referred to in this work are listed with their corresponding Miller indices in Table 9.2.

Table 9.1: Conventions for planes and directions using Miller indices in a hexagonal coordinate system

$(hjkl)$	for a plane or set of parallel planes
$\{hjkl\}$	for a full set of planes of equivalent symmetry
$[hjkl]$	for a direction
$\langle hjkl\rangle$	for a full set of equivalent directions

Table 9.2: Labels and Miller indices for common planes in a hexagonal coordinate system.

a-plane	$\{11\bar{2}0\}$
c-plane	(0001)
m-plane	$\{10\bar{1}0\}$
r-plane	$\{1\bar{1}02\}$

REFERENCES

[1] Genesis 1:1-4, *Holy Bible, New International Version*, Zondervan Publishing House, Grand Rapids, MI (1973).

[2] F. A. Ponce and D. P. Bour, *Nature* **386**, 351 (1997).

[3] J. Black, H. Lowckwood, and S. Mayburg, *J. App. Phys.* **34**, 178 (1963).

[4] A. Einstein, *Phys. Z.* **18**, 121 (1917).

[5] R. Ladenburg and H. Kopfermann, *Z. Phys. Chemie Abt. A* **139**, 375 (1928).

[6] R. N. Hall, G. E. Fenner, J. D. Kingsley, T. J. Soltys, and R. O Carlson, *Phys. Rev. Lett.* **9**, 366 (1962).

[7] L. A. Coldren and S. W. Corzine, *Diode Lasers and Photonic Integrated Circuits*, p. 1, John Wiley & Sons, Inc., New York (1995).

[8] N. Tessler, G. J. Denton, and R. H. Friend, *Nature* **382**, 695 (1996).

[9] U. Lemmer, *Polym. Adv. Technol.* **9**, 476 (1998).

[10] G. Landwehr, A. Waag, F. Fischer, H. J. Lugauer, and K. Schull, *Physica E* **3**, 158 (1998).

[11] D. Hommel, T. Behr, E. Kurtz, B. Jobst, K. Schull, A. Jakobs, J. Nurnberger, S. Einfeldt, M. Behringer, G. Landwehr, *J. Cryst. Growth* **159**, 566 (1996).

[12] D. Hofstetter, R. L. Thornton, M. Kneissl, D. P. Bour, and C. Dunnrowicz, *Appl. Phys. Lett.* **73**, 1928 (1998).

[13] S. Nakamura, M. Senoh, S. Nagahama, N. Iwasa, T. Yamada, T. Matsushita, H. Kiyoku, Y. Sugimoto, T. Kozaki, H. Umemoto, M. Sano, and K. Chocho, *Jpn. J. Appl. Phys. 2* **37**, L1020 (1998).

[14] U. Lemmer, C. Kallinger, A. Haugeneder, W. Spirkl, J. Feldmann, U. Scherf, A. Gombert, and V. Wittwer, "An All Plastic Distributed Feedback laser," *Optics & Photonics News* **9 (12)**, 24 (1998).

[15] S. N. Mohammad, A. A. Salvador, and H. Morkoç, *Proceedings of the IEEE* **83**, 1306 (1995).

[16] A. V. Nurmikko and R. L. Gunshor, *IEEE J. Quantum Electron.* **30**, 619 (1994).

[17] U. V. Desnica, *Progress In Crystal Growth And Characterization Of Materials* **36** (4), 291 (1998).

[18] H. P. Maruska and J. J. Tietjen, *Appl. Phys. Lett.* **15**, 327 (1969).

[19] S. Strite and H. Morkoç, *J. Vac. Sci. Technol. B* **10**, 1237 (1992).

[20] R. A. Smith, *Semiconductors, Second Edition*, p. 429, Cambridge University Press, Cambridge (1959).

[21] M. Shimotomai and A. Yoshikawa, *Appl. Phys. Lett.* **73**, 3256 (1998).

[22] R. Singh, D. Doppalapudi, T. D. Moustakas, and L. T. Romano, *Appl. Phys. Lett.* **70**, 1089 (1997).

[23] M. D. McCluskey, L. T. Romano, B. S. Krusor, N. M. Johnson, T. Suski, and J. Jun, *Appl. Phys. Lett.* **73**, 1281 (1998).

[24] R. Dingle, K. L. Shaklee, R. F. Leheny, and R. B. Zetterstrom, *Appl. Phys. Lett*. **19**, 5 (1971).

[25] H. Amano, T. Asahi, and I. Akasaki, *Jpn. J. Appl. Phys.* **29**, L205 (1990).

[26] H. M. Manasevit, F. M. Erdmann, and W. I. Simpson, *J. Electrochem. Soc*. **118**, 1864 (1971).

[27] S. Yoshida, S. Misawa, and S. Gonda, *Appl. Phys. Lett*. **42**, 427 (1983).

[28] H. Amano, N. Sawaki, I Akasaki, and Y. Toyoda, *Appl. Phys. Lett.* **48**, 353 (1986).

[29] H. Amano, M. Kito, K. Hiramatsu, and I. Akasaki, *Jpn. J. Appl. Phys*. **28**, L2112 (1989).

[30] S. Nakamura, T. Mukai, M. Senoh, and N. Iwasa, *Jpn. J. Appl. Phys.* **31**, L139 (1992).

[31] S. Nakamura, M. Senoh, S. Nagahama, N. Iwasa, T. Yamada, T. Matsushita, H. Kiyoku, and Y. Sugimoto, *Jpn. J. Appl. Phys.* **35**, L74 (1996).

[32] S. Nakamura, *Mater. Res. Soc. Proc.* **449**, 1135 (1996).

[33] K. Itaya, *Jpn. J. Appl. Phys.* **35**, L1315 (1996).

[34] Y.-K. Song, M. Kuball, A. V. Nurmikko, G. E. Bulman, K. Doverspike, S. T. Sheppard, T. W. Weeks, M. Leonard, H. S. Kong, H. Dieringer, and J. Edmond, *Appl. Phys. Lett.* **72**, 1418 (1998).

[35] M. Kneissl, D. P. Bour, N. M. Johnson, L. T. Romano, B. S. Krusor, R. Donaldson, J. Walker, and C. Dunnrowicz, *Appl. Phys. Lett.* **72**, 1539 (1998).

[36] S. Nakamura, *MRS Internet J. Nitride Semicond. Res.* **2**, 5 (1997).

[37] Y. Hara, “Nichia pushes blue laser diodes to violet,” *EE Times Online*, 09 Apr. 1998.

[38] N. G. Weimann, L. F. Eastman, D. Doppalapudi, H. M. Ng, and T. D. Moustakas, *J. Appl. Phys*. **83**, 3656 (1998).

[39] T. Lei, K. F. Ludwig, Jr., and T. D. Moustakas, *J. Appl. Phys.* **74**, 4430 (1993).

[40] D. Kapolnek, X. H. Wu, B. Heying, S. Keller, B. P. Keller, U. K. Mishra, S. P. DenBaars, and J. S. Speck, *Appl. Phys. Lett.* **67**, 1541 (1995).

[41] F. A. Ponce, B. S. Krusor, J. S. M. Jr., W. E. Plano, and D. F. Welch, *J. Appl. Phys.* **67**, 410 (1995).

[42] S. D. Lester, F. A. Ponce, M. G. Craford, and D. A. Steigerwald, *Appl. Phys. Lett.* **66**, 1249 (1995).

[43] J. E. Northrup, J. Neugebauer, and L. T. Romano, *Phys. Rev. Lett.* **77**, 103 (1996).

[44] Y. Xin, S. J. Pennycook, N. D. Browning, P. D. Nellist, S. Sivananthan, F. Omnès, B. Beaumont, J. P. Fauri, and P. Gibart, *Appl. Phys. Lett.* **72**, 2680 (1998).

[45] *Physical Constants for Transport Studies of the Group III-Nitrides,* webpage: http://www.iiiv.cornell.edu/www/foutz/nitride.html

[46] C.-K. Sun, S. Keller, G. Wang, M. S. Minsky, J. E. Bowers, and S. P. DenBaars, *Appl. Phys. Lett.* **69**, 1936 (1996).

[47] M. S. Minsky, S. B. Fleischer, A. C. Abare, J. E. Bowers, E. L. Hu, S. Keller, and S. P. Denbaars, *Appl. Phys. Lett.* **72**, 1066 (1998).

[48] M. Pophristic, F. H. Long, C. Tran, R. F. Karlicek, Jr., Z. C. Feng, and I. T. Ferguson, *Appl. Phys. Lett.* **73**, 815 (1998).

[49] F. A. Ponce, D. P. Bour, W. Götz, N. M. Johnson, H. I. Helava, I. Grzegory, J. Jun, and S. Porowski, *Appl. Phys. Lett.* **68**, 917 (1996).

[50] R. P. Vaudo, V. M. Phanse, X. H. Wu, Y. Golan, and J. S. Speck, 2nd International Conference on Nitride Semiconductors, Tokushima, Japan (1997).

[51] J. Park, P. A. Grudowski, C. J. Eiting, and R. D. Dupuis, *Appl. Phys. Lett.* **73**, 333 (1998).

[52] J. A. Freitas, Jr., O.-H. Nam, R. F. Davis, G. V. Saparin, and S. K. Obyden, *Appl. Phys. Lett.* **72**, 2990 (1998).

[53] H. Ishikawa, S. Kobayashi, Y. Koide, S. Yamasaki, S. Nagai, J. Umezaki, M. Koike, and M. Murakami, *J. App. Phys.* **81**, 1315 (1997).

[54] R. F. Davis, *Physica B* **185**, 1 (1993).

[55] E. F. Schubert, W. Grieshaber, and I. D. Goepfert, *Appl. Phys. Lett.* **69**, 3737 (1996).

[56] K. Domen, R. Soejima, A. Kuramata, K. Horino, S. Kubota, and T. Tanahashi, *Appl. Phys. Lett.* **73**, 2775 (1998).

[57] D. Stocker, E. F. Schubert, K. S. Boutros, J. S. Flynn, R. P. Vaudo, V. M. Phanse, and J. M. Redwing, *Elect. Lett.* **34**, 373 (1998).

[58] D. A. Stocker, E. F. Schubert, W. Grieshaber, K. S. Boutros, and J. M. Redwing, *Appl. Phys. Lett.* **73**, 1925 (1998).

[59] F. Binet, J. Y. Duboz, N. Laurent, C. Bonnat, P. Collot, F. Hanauer, O. Briot, and R. L. Aulombard, *Appl. Phys. Lett.* **72**, 960 (1998).

[60] S. Nakamura, M. Senoh, S. Nagahama, N. Iwasa, T. Yamada, T. Matsushita, H. Kiyoku, and Y. Sugimoto, *Appl. Phys. Lett.* **68**, 2106 (1996).

[61] S. M. Sze, *Physics of Semiconductor Devices, 2nd Edition,* John Wiley & Sons, New York, p. 683 (1981).

[62] C. Kittel, *Introduction to Solid State Physics, 6th Edition*, John Wiley & Sons, New York, pp. 300-301 (1986).

[63] M. S. Shur and M. A. Khan, *Mat. Res. Bull.* **22** (2), 44 (1997).

[64] G. D. Chen, M. Smith, J. Y. Lin, H. X. Jiang, A. Salvador, B. N. Sverdlov, A. Botchkarv, and H. Morkoç, *J. Appl. Phys.* **79**, 2675 (1996).

[65] D. M. Hofmann, D. Kovalev, G. Steude, B. K. Meyer, A. Hoffmann, L. Eckey, R. Heintz, T. Detchprom, H. Amano, and I. Akasaki, *Phys. Rev. B* **52**, 16702 (1995).

[66] S. Chichibu, T. Azuhata, T. Sota, and S. Nakamura, *J. Appl. Phys.* **79**, 2784 (1996).

[67] W. Grieshaber, E. F. Schubert, I. D. Goepfert, R. F. Karlicek, Jr., M. J. Schurman, and C. Tran, *J. Appl. Phys.* **80**, 4615 (1996).

[68] F. J. Sánchez, D. Basak, M. A. Sánchez-García, E. Calleja, E. Muñoz, I. Izpura, F. Calle, J. M. G. Tijero, B. Beaumont, P. Lorezini, Pierre Gibart, T. S. Cheng, C. T. Foxon, and J. W. Orton, *MRS Internet J. Nitride Semicond. Res.* **1**, 7 (1996).

[69] A. Cremades, J. Piqueras, C. Xavier, T. Monteiro, E. Pereira, B. K. Meyer, D. M. Hofmann, and S. Fischer, *Mat. Sci. and Eng.* **B42**, 230 (1996).

[70] J. Neugebauer and C. G. Van de Walle, *Appl. Phys. Lett.* **69**, 503 (1996).

[71] K. Saarinen, T. Laine, S. Kuisma, J. Nissila, P. Hautojarvi, L. Dobrzynski, J. M. Baranowski, K. Pakula, R. Stepniewski, M. Wojdak, A. Wysmolek, T. Suski, M. Leszczynski, I. Grzegory I, and S. Porowski, *Phys. Rev. Lett.* **79**, 3030 (1997).

[72] E. F. Schubert, I. D. Goepfert, and J. M. Redwing, *Appl. Phys. Lett.* **71**, 3224 (1997).

[73] A. F. Wright and U. Grossner, *Appl. Phys. Lett.* **73**, 2751 (1998).

[74] S. S. Liu, T. R. Cass, and D. A. Stevenson, *J. Electron. Mater.* **6**, 237 (1977).

[75] M. Ilegems and R. Dingle, *J. Appl. Phys.* **44**, 4234 (1973).

[76] S. Nakamura, M. Senoh, and T. Mukai, *Jpn. J. Appl. Phys.* **30**, L1708 (1991).

[77] I. Akasaki, H. Amano, M. Kito, and K. Hiramatsu, *J. Lumin.* **48/49**, 666 (1991).

[78] K. L. Shaklee, R. E. Nahory, and R. F. Leheny, *J. Lumin.* **7**, 284 (1973).

[79] S. Nakamura, M. Senoh, S. Nagahama, N. Iwasa, T. Yamada, T. Matsushita, Y. Sugimoto, and H. Kiyoku, *Appl. Phys. Lett.* **69**, 1568 (1996).

[80] S. T. Kim, H. Amano, I. Akasaki, and N. Koide, *Appl. Phys. Lett.* **64**, 1535 (1994).

[81] J. Holst, L. Eckey, A. Hoffmann, I. Broser, B. Schöttker, D. J. As, D. Schikora, and K. Lischka, *Appl. Phys. Lett.* **72**, 1439 (1998).

[82] R. Klann, O. Brandt, H. Yang, H. T. Grahn, and K. H. Ploog, *Appl. Phys. Lett.* **70**, 1076 (1997).

[83] A. Billeb, W. Grieshaber, D. Stocker, E. F. Schubert, and R. F. Karlicek, *Appl. Phys. Lett.* **70**, 2790 (1997).

[84] D. A. Francis, C. J. Chang-Hasnain, and K. Eason, *Appl. Phys. Lett.* **68**, 1598 (1996).

[85] R. J. Shul, L. Zhang, C. G. Willison, J. han, J. Hong, S. J. Pearton, and L. F. Lester, "Group -III Nitride Etch Selectivity in Boron Trichloride/Chlorine ICP Plasmas," MRS Fall Meeting (1998).

[86] H. Lee, D. B. Oberman, and J. S. Harris, Jr., *J. Electron. Mater.* **25**, 835 (1996).

[87] A. T. Ping, I. Adesida, M. A. Khan, and J. N. Kuznia, *Electronics Letters* **30**, 1895 (1994).

[88] M. E. Lin, Z. F. Fan, Z. Ma, L. H. Allen, and H. Morkoç, *Appl. Phys. Lett.* **64**, 887 (1994).

[89] J. B. Fedison, T. P. Chow, H. Lu, and I. B. Bhat, *J. Electrochem. Soc.* **144**, L221 (1997).

[90] S. Nakamura and G. Fasol, *The Blue Laser Diode*, Springer-Verlag, New York, NY p. 225 (1997).

[91] G. F. McLane, L. Casas, S. J. Pearton, and C. R. Abernathy, *Appl. Phys. Lett.* **66**, 3328 (1995).

[92] S. A. Smith, C. A. Wolden, M. D. Bremser, A. D. Hanser, R. F. Davis, and W. V. Lampert, *Appl. Phys. Lett.* **71**, 3631 (1997).

[93] J. W. Lee, C. B. Vartuli, C. R. Abernathy, J. D. MacKenzie, J. R. Mileham, S. J. Pearton, R. J. Shul, J. C. Zolper, M. Hagerott-Crawford, J. M. Zavada, R. G. Wilson, and R. N. Schwartz, *J. Vac. Sci. Technol. B* **14**, 3637 (1996).

[94] S. Nakamura, M. Senoh, S. Nagahama, N. Iwasa, T. Yamada, T. Matsushita, H. Kiyoku, Y. Sugimoto, T. Kozaki, H. Umemoto, M. Sano, and K. Chocho, *Appl. Phys. Lett.* **72**, 211 (1998).

[95] A. T. Ping, C. Youtsey, I. Adesida, M. A. Khan, and J. N. Kuznia, *J. of Electron. Mat.* **24**, 229 (1995).

[96] A. T. Ping, I. Adesida, and M. A. Khan, *Appl. Phys. Lett.* **67**, 1250 (1995).

[97] H. P. Gillis, D. A. Choutov, and K. P. Martin, *JOM* August 1996, 50 (1996).

[98] S. J. Pearton, J. W. Lee, J. D. MacKenzie, C. R. Abernathy, and R. J. Shul, *Appl. Phys. Lett.* **67**, 2329 (1995).

[99] B. Molnar, C. R. Eddy, Jr., and K. Doverspike, *J. Appl. Phys.* **78**, 6132 (1995).

[100] F. Ren, J. R. Lothian, S. J. Pearton, C. R. Abernathy, C. B. Vartuli, J. D. MacKenzie, R. G. Wilson, and R. F. Karlicek, *J. of Electron. Mat.* **26**, 1287 (1997).

[101] J. E. Northrup and J. Neugebauer, *Phys. Rev. B* **53**, R10477 (1996).

[102] A. Kuramata, K. Horino, K. Domen, and T. Tanahashi, *Solid-State Electronics* **41**, 251 (1997).

[103] R. K. Sink, S. Keller, B. P. Keller, K. I. Babic, A. L. Holmes, D. Kapolnek, S. P. DenBaars, J. E. Bowers, X. H. Wu, and J. S. Speck, *Appl. Phys. Lett.* **68**, 2147 (1996).

[104] K. Itaya, M. Onomura, J. Nishio, L. Sugiura, S. Saito, M. Suzuki, J. Rennie, S. Nunoue, M. Yamamoto, H. Fujimoto, Y. Kokubun, Y. Ohba, G. Hatakoshi, and M. Ishikawa, *Jpn. J. Appl. Phys.* **35**, L1315 (1996).

[105] S. Nakamura, M. Senoh, S. Nagahama, N. Iwasa, T. Yamada, T. Matsushita, Y. Sugimoto, and H. Kiyoku, *Appl. Phys. Lett.* **69**, 1477 (1996).

[106] S. Keller, U. K. Mishra, and S. P. DenBaars, LEOS Annual meeting (1996).

[107] B. Mason and L. G. Berry, *Elements of Mineralogy*, W. H. Freeman and Company, San Francisco, p. 289 (1968).

[108] I. Kostov, *Mineralogy*, Oliver and Boyd, Ltd., Edinburgh and London, p. 31 (1968).

[109] S. Nakamura, M. Senoh, S. Nagahama, N. Iwasa, T. Yamada, T. Matsushita, H. Kiyoku, and Y. Sugimoto, *Jpn. J. Appl. Phys.* **35**, Pt. 2, L217 (1996).

[110] K. Doverspike, G. E. Bulman, S. T. Sheppard, T. W. Weeks, M. T. Leonard, H. Kong, H. Dieringer, C. H. Carter, Jr., J. A. Edmond, J. D. Brown, J. T. Swindle, J. F. Schetzina, Y. Song, M. Kuball, and A. V. Nurmikko, Photonics West 1998 Conference 3284 (1998).

[111] M. A. Khan, C. J. Sun, J. W. Yang, Q. Chen, B. W. Lim, M. Z. Anwar, A Osinsky, and H. Temkin, *Appl. Phys. Lett.* **69**, 2418 (1996).

[112] S. Nakamura, M. Senoh, S. Nagahama, N. Iwasa, T. Yamada, T. Matsushita, H. Kiyoku, Y. Sugimoto, T. Kozaki, H. Umemoto, M. Sano, and K. Chocho, *Appl. Phys. Lett.* **73**, 832 (1998).

[113] C. Youtsey, I. Adesida, and G. Bulman, *Appl. Phys. Lett.* **71**, 2151 (1997).

[114] D. A. Stocker and E. F. Schubert, “Reduction of surface roughness in photoenhanced electrochemical wet-etched GaN,” *J. Electrochem. Soc.* (1999) (submitted).

[115] M. S. Minsky, M. White, and E. L. Hu, *Appl. Phys. Lett.* **68**, 1531 (1996).

[116] L.-H. Peng, C.-W. Chuang, J.-K. Ho, C.-N. Huang, and C.-Y. Chen, *Appl. Phys. Lett.* **72**, 939 (1998).

[117] H. Lu, Z. Wu, and I. Bhat, *J. Electrochem. Soc.* **144**, L8 (1997).

[118] R. Khare and E. L. Hu, *J. Electrochem. Soc.* **138**, 1516 (1991).

[119] C. Youtsey, G. Bulman, and I. Adesida, *J. Electron. Mat.* **27**, 282 (1997).

[120] C. Youtsey, L. T. Romano, and I. Adesida, *Appl. Phys. Lett.* **73**, 797 (1998).

[121] C. Youtsey, I. Adesida, L. T. Romano, and G. Bulman, *Appl. Phys. Lett.* **72**, 560 (1998).

[122] H. P. Gillis, M. J. Christopher, K. P. Martin, and D. A. Choutov, “Patterning III-N Semiconductors by Low Energy Electron Enhanced Etching (LE4),” Fifth Wide Bandgap Nitride Semiconductor Workshop, St. Louis, MO, 1998.

[123] S. Adachi and K. Oe, *J. Electrochem. Soc.* **130**, 2427 (1983).

[124] Y. Tarui, Y. Komiya, and Y. Harada, *J. Electrochem. Soc.* **118**, 118 (1971).

[125] D. W. Shaw, *J. Electrochem. Soc.* **128**, 874 (1981).

[126] I. Shiota, K. Moloya, T. Ohmi, N. Miyamoto, and J. Nishizawa, *J. Electrochem. Soc.* **124**, 155 (1977).

[127] D. R. Turner, *J. Electrochem. Soc.* **105**, 402 (1958).

[128] K. E. Bean, *IEEE Transactions on Electron Devices* **ED-25**, 1185 (1978).

[129] J. J. Boland and J. H. Weaver, *Physics Today* August 1998, p. 34 (1998).

[130] A. R. Smith, R. M. Feenstra, D. W. Greve, J. Neugebauer, and J. E. Northrup, *Phys. Rev. Lett.* **79**, 3934 (1997).

[131] A. R. Smith, R. M. Feenstra, D. W. Greve, M. S. Shin, M. Skowronski, J. Neugebauer, and J. E. Northrup, *J. Vac. Sci. Technol. B* **16**, 2242 (1998).

[132] W. C. Hughes, W. H. Rowland, Jr., M. A. L. Johnson, S. Fujita, J. W. Cook, Jr., J. F. Schetzina, J. Ren, and J. A. Edmond, *J. Vac. Sci. Technol. B* **13**, 1571 (1995).

[133] K. Iwata, H. Asahi, S. J. Yu, K. Asami, K. Fujita, M. Fushida, and S. Gonda, *Jpn. J. Appl. Phys., Part 2* **35**, L289 (1996).

[134] G. Wulff, *Z. Krist.* **34**, 449 (1901).

[135] C. Herring, *Phys. Rev.* **82**, 87 (1951).

[136] D. W. Shaw, *J. Cryst. Growth* **47**, 509 (1979).

[137] C.B. Vartuli, S.J. Pearton, C.R. Abernathy, J.D. MacKenzie, F. Ren, J.C. Zolper, and R.J. Shul, *Solid-State Electronics* **41**, 1947 (1997).

[138] J. L. Weyher, S. Müller, I. Grzegory, and S. Porowski, *J. Cryst. Growth* **182**, 17 (1997).

[139] D. A. Stocker, E. F. Schubert, and J. M. Redwing, *Appl. Phys. Lett.* **73**, 2654 (1998).

[140] A. Shintani and S. Minagawa, *J. Electrochem. Soc.* **123**, 707 (1976).

[141] T. Kozawa, T. Kachi, T. Ohwaki, Y. Taga, N. Koide, and M. Koike, *J. Electrochem. Soc.* **143**, L17 (1996).

[142] S. K. Hong, B. J. Kim, H. S. Park, Y. Park, S. Y. Yoon, and T. I. Kim, *J. Cryst. Growth* **191**, 275 (1998).

[143] R. C. Weast, M. J. Astle, and W. H. Beyer, ed., *CRC Handbook of Chemistry and Physics, 66th Ed.*, CRC Press, Inc., Boca Raton, FL, p. E-99, (1985).

[144] R. C. Weast, M. J. Astle, and W. H. Beyer, ed., *CRC Handbook of Chemistry and Physics, 66th Ed.*, CRC Press, Inc., Boca Raton, FL, p. D-77, (1985).

[145] J. R. Mileham, S. J. Pearton, C. R. Abernathy, J. D. MacKenzie, R. J. Shul, and S. P. Kilcoyne, *Appl. Phys. Lett.* **67**, 1119 (1995).

[146] R. Williams, *Modern GaAs Processing Methods*, Artech House, Inc., Boston, p. 95 (1990).

[147] H. P. Gillis, M. J. Christopher, K. P. Martin, and D. A. Choutov, "Patterning III-N Semiconductors by Low Energy Electron Enhanced Etching (LE4), *MRS Fall 1998 Meeting*, G8.2 (1998).

[148] M. Seelmann-Eggebert, J. L. Weyher, H. Obloh, H. Zimmermann, A. Rar, and S. Porowski, *Appl. Phys. Lett.* **71**, 2635 (1997).

[149] L. A. Coldren and S. W. Corzine, *Diode Lasers and Photonic Integrated Circuits*, John Wiley & Sons, Inc., New York, p. 446 (1995).

[150] E. F. Schubert, I. D. Goepfert, W. Grieshaber, and J. M. Redwing, *Appl. Phys. Lett.* **71**, 921 (1997).

[151] S. Ruvimov, Z. Liliental-Weber, T. Suski, J. W. Ager III, J. Washburn, J. Krueger, C. Kisilowski, E. R. Weber, H. amano, and I. Akasaki, *Appl. Phys. Lett.* **69**, 990 (1996).

[152] P. A. Grudowski, C. J. Eitling, J. Park, B. S. Shelton, D. J. H. Lambert, and R. D. Dupuis, *Appl. Phys. Lett.* **71**, 1537 (1997).

[153]S. Bidnyk, T. J. Schmidt, Y. H. Cho, G. H. Gainer, J. J. Song, S. Keller, U. K. Mishra, and S. P. DenBaars, *Appl. Phys. Lett.* **72**, 1623 (1998).

[154] Y.-H. Cho, J. J. Song, S. Keller, M. S. Minsky, E. Hu, U. K. Mishra, and S. P. DenBaars, *Appl. Phys. Lett.* **73**, 1128 (1998).

[155] A. Salvador, G. Liu, W. Kim, Ö. Aktas, A. Botchkarev, and H. Morkoç, *Appl. Phys. Lett.* **67**, 3322 (1995).

[156] K. C. Zeng, J. Y. Lin, H. X. Jiang, A. Salvador, G. Popovici, H. Tang, W. Kim, and H. Morkoç, *Appl. Phys. Lett.* **71**, 1368 (1997).

[157] S. Nakamura, M. Senoh, S. Nagahama, N. Iwasa, T. Yamada, T. Matsushita, Y. Sugimoto, and H. Kiyoku, *Appl. Phys. Lett.* **70**, 1417 (1997).

[158] D. Hofstetter, D. P. Bour, R. L. Thornton, and N. M. Johnson, *Appl. Phys. Lett.* **70**, 1650 (1997).

[159] I. K. Shmagin, J. F. Muth, R. M. Kolbas, and S. Krishnankutty, *J. Appl. Phys.* **81**, 2021 (1997)

[160] K. S. Boutros, ATMI/Epitronics, Danbury, CT, private communication (1997).

[161] D. A. Cohen, T. Margalith, A. C. Abare, M. P. Mack, L. A. Coldren, S. P. DenBaars, and D. R. Clarke, *Appl. Phys. Lett.* **72**, 3267 (1998).

[162] D. P. Bour, M. Kneissl, L. T. Romano, M. D. McCluskey, C. G. Van deWalle, B. S. Krusor, R. M. Donaldson, J. Walker, C. J. Dunnrowicz, and N. M. Johnson, *IEEE J. Select. Topics Quantum Electron.* **4**, 498 (1998).

[163] A. C. Abare, M. P. Mack, M. Hansen, J. S. Speck, L. A. Coldren, S. P. DenBaars, G. A Meyer, S. L. Lehew, and G. A. Cooper, *Appl. Phys. Lett.* **73**, 3887 (1998).

[164] I. Adesida (University of Illinois), F. Ren (University of Florida), and B. K. Lee (University of Cincinnati), private communication (1998).

[165] Private communication (1998).

[166] L. F. Eastman (Cornell University), private communication (1999).

[167] S. M. Sze, *Physics of Semiconductor Devices, 2nd Edition*, John Wiley & Sons, New York, p. 11 (1981).